



# Algorithm Theoretical Basis Document (ATBD) for the Conical-Scanning Microwave Imager/Sounder (CMIS) Environmental Data Records (EDRs)

## Volume 2: Core Physical Inversion Module

**Version 1.4 – 15 March 2001**

**Solicitation No. F04701-01-R-0500**

Submitted by:

**Atmospheric and Environmental Research, Inc.  
131 Hartwell Avenue  
Lexington, MA 02421**

With contributions by:

**Jean-Luc Moncet, Sid-Ahmed Boukabara, Alan Lipton, John Galantowicz,  
Hélène Rieu-Isaacs, Jennifer Hegarty, Xu Liu, Richard Lynch, Ned Snell**

Prepared for:

**Boeing Satellite Systems  
919 Imperial Avenue  
El Segundo, CA 90245**

**AER Document P757-TR-I-ATBD-CORE-MODULE-20010315**

This page intentionally left blank.

## REVISION HISTORY

Version	Release Date	POC	Comments
1.0	02/2000	J.-L. Moncet, AER, Inc.	First Draft Version
1.1	10/2000	J.-L. Moncet, AER, Inc.	Second Draft Version
1.2			
1.3	01/2001	J.-L. Moncet, AER, Inc.	General re-write of most sections for clarity; significant additions to Sections 4 and 5.
1.4	02/22/2001; 03/15/2001	J.-L. Moncet, AER, Inc.	Final revisions and addition of new sections before delivery; Reformatting some pages Insertion of performance results Revision of appendicies

## RELATED CMIS DOCUMENTATION

### Government Documents

Title	Version	Authorship	Date
CMIS SRD for NPOESS Spacecraft and Sensors	3.0	Associate Directorate for Acquisition NPOESS IPO	2 March 2001

### Boeing Satellite Systems Documents

Title		Covering
ATBD for the CMIS TDR/SDR Algorithms		
<b>ATBD for the CMIS EDRs</b>	Volume 1: Overview	Part 1: Integration Part 2: Spatial Data Processing Footprint Matching and Interpolation Gridding Imagery EDR
	<b>Volume 2: Core Physical Inversion Module</b>	
	Volume 3: Water Vapor EDRs	Atmospheric Vertical Moisture Profile EDR Precipitable Water EDR
	Volume 4: Atmospheric Vertical Temperature Profile EDR	
	Volume 5: Precipitation Type and Rate EDR	
	Volume 6: Pressure Profile EDR	
	Volume 7: Cloud EDRs	Part 1: Cloud Ice Water Path EDR
		Part 2: Cloud Liquid Water EDR
		Part 3: Cloud Base Height EDR
	Volume 8: Total Water Content EDR	
	Volume 9: Soil Moisture EDR	
	Volume 10: Snow Cover/Depth EDR	
	Volume 11: Vegetation/Surface Type EDR	
	Volume 12: Ice EDRs	Sea Ice Age and Sea Ice Edge Motion EDR Fresh Water Ice EDR
	Volume 13: Surface Temperature EDRs	Land Surface Temperature EDR Ice Surface Temperature EDR
	Volume 14: Ocean EDR Algorithm Suite	Sea Surface Temperature EDR Sea Surface Wind Speed/Direction EDR Surface Wind Stress EDR
	Volume 15: Test and Validation	All EDRs

**Bold** = this document

## TABLE OF CONTENTS FOR VOLUME 2

<b>REVISION HISTORY.....</b>	<b>3</b>
<b>RELATED CMIS DOCUMENTATION .....</b>	<b>4</b>
<b>TABLE OF CONTENTS.....</b>	<b>5</b>
<b>LIST OF TABLES .....</b>	<b>8</b>
<b>LIST OF FIGURES .....</b>	<b>9</b>
<b>1. Introduction.....</b>	<b>15</b>
1.1. Purpose.....	15
1.2. Scope.....	15
<b>2. Overview and Background Information.....</b>	<b>16</b>
2.1. Instrument Characteristics.....	16
2.2. CMIS Channels Used in the Core Physical Inversion Module .....	16
<b>3. Core Physical Inversion Algorithm Processing Outline.....</b>	<b>24</b>
3.1. Overview of Core Physical Inversion Module.....	24
3.2. Core Module Outputs.....	24
3.3. Core Module Inputs.....	25
3.3.1. Required Sensor Inputs .....	25
3.3.2. Ancillary Data Inputs .....	25
<b>4. Theoretical Description of the Core Physical Inversion Algorithm.....</b>	<b>28</b>
4.1. Forward Modeling.....	28
4.1.1. Radiative Transfer Equation.....	28
4.1.2. Overview of the OSS Method .....	28
4.1.3. Transmittance Model.....	31
4.1.4. Radiance Calculation.....	32
4.1.5. Scattering Model .....	38
4.2. Inversion Approach.....	38
4.2.1. General Inversion Methodology.....	39
4.2.2. Pseudo Linearization Noise.....	40
4.2.3. Eigenvector Transformation of Retrieved Parameters .....	41
4.2.4. Retrieved Parameters.....	42
4.3. Physical Constraints on Retrieval Solution and Quality Control of Retrieved Parameters	46
<b>5. Core Physical Inversion Module Performance Analysis.....</b>	<b>48</b>

5.1. Test Data Sets.....	48
5.2. Emissivity Retrieval Results .....	50
5.3. Performance Stratification and Algorithm Robustness.....	53
5.4. Graceful Degradation .....	56
5.5. Sensitivity to Land Surface Emissivity and Prior Knowledge.....	58
5.6. Quality Control.....	61
5.6.1. Impact of Ice Water Path (IWP) on Retrieval Process and Performance.....	65
5.6.2. Impact of Precipitation on Retrieval Process and Performance .....	75
<b>6. APPENDIX 1: THE NOAA-88 GLOBAL ATMOSPHERIC PROFILE DATA SET.</b>	<b>80</b>
6.1. Introduction .....	80
6.2. Statistics of the Data Set.....	80
6.3. Modifications .....	80
6.3.1. Surface Pressure .....	80
6.3.2. Water Vapor Profiles.....	81
<b>7. APPENDIX 2: SURFACE PRESSURE COMPUTATION.....</b>	<b>87</b>
7.1. Basis .....	87
7.2. Inputs to the Hydrostatic Equation.....	87
7.3. Interpolation .....	87
7.4. Data Sources.....	89
7.5. Particular Cases Handling .....	90
7.6. Possible Improvement.....	90
<b>8. APPENDIX 3: SURFACE EMISSIVITY MODELING.....</b>	<b>91</b>
8.1. Emissivity Modeling Approach .....	91
8.2. Initial Emissivity Datasets.....	91
8.3. Extrapolation Method.....	92
8.3.1. Extrapolation Method Approach and Description.....	92
8.3.2. Extrapolation Method Validation.....	94
<b>9. APPENDIX 4: IMPACT OF DYNAMIC EMISSIVITY ON CORE MODULE RETRIEVALS.....</b>	<b>96</b>
9.1. Purpose.....	96
9.2. Simulations and Results .....	96
9.3. Summary .....	102
<b>10. APPENDIX 5: IMPACT OF AN AIR MASS CLASSIFICATION ON CORE MODULE RETRIEVALS.....</b>	<b>107</b>

10.1. Overview .....	107
10.2. Air Mass Classification of the TIGR-2 Dataset using a PNN.....	107
10.2.1. Network Architecture .....	107
10.2.2. Training and Validation.....	108
10.2.3. Results .....	108
10.3. Impact of Air-Mass Pre-Classification on Core Module Retrievals .....	109
<b>11. APPENDIX 6: IMPACT OF SURFACE EMISSIVITY CLASSIFICATION ON CORE MODULE RETRIEVALS .....</b>	<b>113</b>
11.1. Overview .....	113
11.2. Classification algorithm .....	113
11.3. Background statistics generation.....	114
11.4. Impact of pre-classification on retrieval performance .....	116
<b>REFERENCES.....</b>	<b>118</b>
<b>LIST OF ACRONYMS.....</b>	<b>123</b>

## LIST OF TABLES

Table 2-1: CMIS channels used in the Core Physical Inversion Module. ....	17
Table 3-1: Core Module Outputs. ....	24
Table 4-1: Number of Spectral Points Selected for CMIS. ....	30
Table 4-2: $\Delta$ and its Derivatives. ....	38
Table 4-3: List of Retrieved Parameters (EOF Domain). ....	43
Table 5-1: Stratification parameters ....	54
Table 5-2: Typical emissivity values for the three surface spectral emissivity types shown in Figure 5-11 and Figure 5-12. ....	60
Table 5-3: List of flags included in the core module output. ....	63
Table 10-1: Comparison of performance for retrieval variables for global and classified airmass. ....	111



## LIST OF FIGURES

Figure 2-1: Absorption Spectra of Water Vapor and Oxygen in the Microwave. ....	18
Figure 2-2: $\epsilon = 0.5$ . Temperature and Humidity Jacobians. ....	20
Figure 2-3: $\epsilon = 0.9$ - Temperature and Humidity Jacobians. ....	21
Figure 3-1: Core Physical Inversion Module Flow Diagram. ....	27
Figure 4-1: Comparison OSS/Central Frequency (Maximum Differences). ....	31
Figure 4-2: Comparison OSS/Central Frequency ( <i>rms</i> ). ....	31
Figure 4-3: Schematic diagram showing the numbering convention for the atmospheric layers used by OSS, where T refers to transmittances, level 0 represents the top of the atmosphere (TOA) and level N the surface. ....	33
Figure 4-4: Flow Diagram Illustrating the Background Selection for the Surface. ....	46
Figure 5-1: 19 GHz Hpol - Monthly Average - October 1992. ....	51
Figure 5-2: 19 GHz Vpol - Monthly Average - October 1992. ....	51
Figure 5-3: Core module retrieval from SSM/I data and precipitation index from ground-based radar. ....	52
Figure 5-4: Temperature profile (not vertically averaged) rms error for ocean surface, midlatitude summer atmosphere, 50 kg/m <sup>2</sup> precipitable water, 700 mb cloud top, DeltaT <sub>skin</sub> varying from -10 to 10 K (left to right) and cloud liquid water varying from 0 to 0.5 kg/m <sup>2</sup> (top to bottom). The black curves are for the core physical algorithm and the red curves are for regression. ....	54
Figure 5-5: As in Figure 5-4, but for water vapor mixing ratio, and 10 kg/m <sup>2</sup> precipitable water. ....	55
Figure 5-6: As in Figure 5-4, but for precipitable water, plotted versus precipitable water. ....	55
Figure 5-7: As in Figure 5-4, but for cloud liquid water, plotted versus precipitable water. ....	56
Figure 5-8: Impact of loss of the indicated bands on land surface temperature retrieval error. ...	57
Figure 5-9: Impact of loss of the indicated bands on precipitable water retrieval error. ....	57
Figure 5-10: Impact of loss of the indicated bands on cloud liquid water retrieval error. ....	58
Figure 5-11: Impact of <i>a priori</i> land surface emissivity information on clear sky retrievals of (a) land surface temperature, (b) precipitable water, and (c) cloud liquid water. ....	60
Figure 5-12: Impact of <i>a priori</i> land surface emissivity information on cloudy sky retrievals of (a) land surface temperature, (b) precipitable water, and (c) cloud liquid water. ....	61
Figure 5-13: Preliminary Functional Diagram for the Physical Inversion. ....	65

Figure 5-14: Minimum detectable IWP as a function of the mean diameter of the particle size distribution, defined as the minimum amount of ice necessary to induce a brightness temperature change greater than the sensor noise for a given channel. The cirrus cloud top in this case is 250 mb and its thickness is 50 mb. ....	67
Figure 5-15: The solid curve shows the minimum detectable IWP based on the IWP induced depression for the worst of the channels (183 GHz). The dotted curves show the minimum detectable IWP based on the convergence failure criterion. Below the solid curve there is little impact on the retrieval. The curve with “+” symbols represents the chi-square converge criterion while the curve with “*” symbols represents that obtained when using both the chi-square and super-saturation as a quality control metric. In the region between the solid curve and “*” curve the retrieval passes the quality control, but the EDR performance is degraded. ....	68
Figure 5-16: Percentage of points (out of 200 total) that did pass the quality control tests for IWP values of 0, 5, 20, and 40 g/m <sup>2</sup> . ....	69
Figure 5-17: Impact of IWP ( <i>rms</i> and bias) on the temperature and moisture profile retrievals. ....	70
Figure 5-18: Impact on TPW ( <i>rms</i> and bias) of not explicitly accounting for the scattering in the retrieval process while the brightness temperatures are affected by increasing values of the IWP (with a Dme of 700 $\mu$ m and a cloud top at 250 mb). ....	71
Figure 5-19: Impact on CLW ( <i>rms</i> and bias) of not explicitly accounting for the scattering in the retrieval process while the brightness temperatures are affected by increasing values of the IWP (with a Dme of 700 $\mu$ m and a cloud top at 250 mb). ....	71
Figure 5-20: Same as previous figure but for Tskin. In this particular case, an IWP of 20 g/m <sup>2</sup> could come as a bias in the Tskin retrieval of more than 0.4 K with only a moderate impact to the points passing the QC test (see Figure 5-16). ....	72
Figure 5-21: Minimum detectable IWP when the channels above 60 GHz are ignored. The solid curve shows the minimum detectable IWP based on the IWP induced depression for the worst of the channels (60 GHz). The dotted curve shows the minimum detectable IWP based on the chi-squared convergence failure criterion. ....	73
Figure 5-22: Impact of IWP on the temperature and moisture profile retrieval when using only the channels less than or equal to 60 GHz. In this case there is no report for the moisture profile. ....	74
Figure 5-23: Impact on the CLW ( <i>rms</i> and bias) of not explicitly accounting for the scattering in the retrieval process while the brightness temperatures are affected by increasing values of	

the IWP (with a Dme of 700 $\mu\text{m}$ and a cloud top at 250 mb). This retrieval test used only the channels less than or equal to 60 GHz. ....	74
Figure 5-24: Same as previous figure but for Tskin, using only the channels less than or equal to 60 GHz. ....	75
Figure 5-25: Minimum detectable rain-rate (RR) as a function of the cloud top pressure for (a) all channels and (b) ignoring the channels above 60 GHz. ....	76
Figure 5-26: Number of convergent points when (a) using all CMIS channels and (b) neglecting channels above 60 GHz. Note that the small amounts of rain have a much larger impact on the channels above 60 GHz. ....	76
Figure 5-27: Impact of rain-rate on the temperature profile retrieval (a) for all CMIS channels and (b) when neglecting channels above 60 GHz. Note that in this case there is no report for the moisture profile. ....	77
Figure 5-28: Impact of rain-rate on the CLW retrieval (a) for all CMIS channels and (b) when neglecting channels above 60 GHz. ....	78
Figure 5-29: Impact of rain-rate on the retrieval of Tskin (a) for all CMIS channels and (b) when neglecting channels above 60 GHz. ....	79
Figure 6-1: Histogram of the number of observations with latitude for the NOAA-88 data set. .	83
Figure 6-2: Histogram of reported NOAA-88 data set surface pressures. ....	83
Figure 6-3: Histogram of the number of observations in the NOAA-88 data set for each month.	84
Figure 6-4: Histogram of the time of the day the NOAA-88 data set observations were made. ..	84
Figure 6-5: Histogram of the total water vapor column density amounts. ....	84
Figure 6-6: The diamonds in plot (a) are profiles of computed pressure levels mixing ratios put on effective pressure levels. The + in this plots are the computed pressure level mass mixing ratio values interpolated back onto the NOAA-88 pressure grid. Plot (b) shows the comparison between the layer column density amounts provided in the NOAA-88 data set and the layer column density amounts computed from the derived pressure level mixing ratio values shown in plot (a). ....	85
Figure 6-7: Histogram of the difference between the total water vapor column densities provided in the NOAA-88 database and the column densities computed from the derived pressure level mixing ratio values. ....	86
Figure 7-1: NWP Data needed to Compute Surface Pressure. ....	89
Figure 8-1: MeanFigure 8-2 (a) and standard deviation (b) of surface emissivity values at CMIS channel frequencies. ....	95

Figure 8-3: Correlation of each channel emissivity with a reference frequency of (a) 18 GHz and (b) 36 GHz.....	95
Figure 9-1: NWP temperature and mixing ratio profiles and skin and surface air temperature difference for grid point (40.0, -77.5). Eight days at times 0Z and 12Z. ....	97
Figure 9-2: Difference between the cumulative time-averaged and true emissivity and the difference between the retrieved and true emissivity at each time step. Results for the surface channels 10V, 10H, 18V, 18H, 23V, 23H, 36V, 36H, 89V, and 89H for the grid point at (40.0,-77.5).....	98
Figure 9-3: The <i>rms</i> and bias of the difference between the time-averaged and the true and the retrieved and true over 176 grid points. Results for the 10 surface channels. ....	99
Figure 9-4: climatology background case. Retrieved, true and true minus retrieved. Row (1) is the retrieved, row (2) is the true and row (3) is the difference. Column (a) is skin temperature, (b) is TPW and (c) is 23GHz H-pol emissivity.....	100
Figure 9-5: Same as Figure 9-4 but with time-averaged background and covariance.....	101
Figure 9-6: The <i>rms</i> error of temperature and mixing ratio profiles for the 176 NWP grid points. Solid line, climatology background and covariance. Dashed line, time-averaged background and covariance.....	102
Figure 9-7: Same as Figure 9-2 except assumed clear sky conditions.....	104
Figure 9-8: Same as Figure 9-3 except assumed clear sky conditions.....	105
Figure 9-9: Same as Figure 9-4 except assumed clear sky conditions.....	106
Figure 9-10: Same as Figure 9-5 except assumed clear sky conditions.....	106
Figure 10-1: TIGR-2 Classification Results. ....	109
Figure 10-2: Ocean - Comparison of performance for retrieval variables for global and classified air mass.....	111
Figure 10-3: Land - Comparison of performance for retrieval variables for global and classified air mass.....	112
Figure 10-4: Ice - Comparison of performance for retrieval variables for global and classified air mass.....	112
Figure 11-1: Emissivity spectra for the cases classified for developing the high-emissivity background statistics. The spectra cover the CMIS channel set, and were plotted before the baseline sounding channel set was converted from H to V polarization. ....	116
Figure 11-2: Water vapor profile retrieval error for mixed forest surface type with and without surface emissivity pre-classification. The retrievals were performed with noise representative of a composite field of view size of 50 km, and the errors were then inflated	

5% to account for error increase in the cascade from 50 to 15 km. The scenes were cloudy, with liquid water randomly (uniform distribution) ranging from 0 to 0.25 kg/m<sup>2</sup>. ..... 117

## LIST OF FIGURES

## **1. Introduction**

### **1.1. Purpose**

This algorithm theoretical basis document (ATBD) documents the underlying mathematical and theoretical background of the Core Physical Inversion Module (also called the Core Module) developed by Atmospheric and Environmental Research, Inc. (AER) for the Conical Microwave Imaging Sounder (CMIS) in support of the National Polar-orbiting Operational Environmental Satellite System (NPOESS). The Core Module is a physical inversion algorithm designed to simultaneously retrieve temperature and water vapor profiles along the sensor view path, cloud liquid water (CLW), cloud top pressure, skin temperature and surface emissivity. The driving requirement for the core physical inversion algorithm is the extraction of water vapor profiles from the CMIS measurements. The selected approach is best suited for producing water vapor retrievals in clear and cloudy conditions (both liquid water and cirrus ice) and over all surface types, therefore maximizing the range of conditions over which the related Environmental Data Records [EDRs as Atmospheric Vertical Moisture Profile (AVMP), Precipitable Water (PW), Total Water Content (TWC)] will be made available. The objective of this ATBD is to facilitate an understanding of our approach to the CMIS retrieval problem from a phenomenological perspective in the context of the current state-of-the-art. The relationship between the Core Module and the other EDR algorithms is detailed in the ATBD for CMIS EDRs, Volume 1: Overview, Part 1: Integration.

### **1.2. Scope**

Section 2 explains the physics of the problem and describes the relevant CMIS characteristics involved in the process. Section 3 describes the core physical inversion algorithm processing flow with its input and output data. Section 4 presents the theoretical and mathematical description of the algorithm. The algorithm performance is given in Section 5 with a description of the test data followed by sensitivity studies, performance of the algorithm under different conditions, and a description of the constraints and limitations of the algorithm. Appendices follow on the NOAA-88 global atmospheric data set (Appendix 1), the surface pressure computation (Appendix 2), the surface emissivity modeling (Appendix 3), the impact of dynamic emissivities on the Core Physical Inversion module (Appendix 4), the impact of an air-mass pre-classification on the core module retrievals (Appendix 5), and the impact of surface emissivity pre-classification on core module retrievals (Appendix 6). References and a list of acronyms follow.

## **2. Overview and Background Information**

### **2.1. Instrument Characteristics**

The baseline CMIS instrument is a conically scanning microwave radiometer consisting of 40 channels from 6.9 GHz to 183 GHz. There are options to enhance ice cloud detection by extending the spectral coverage to 340 GHz. The CMIS sensor is a dual reflector system. A 2.2 m diameter antenna provides spatial resolution ranging from 64 km to 15 km at 6.9 GHz and 89 GHz, respectively. A second smaller antenna is used for the frequencies above 89 GHz. CMIS has window channels – frequencies chosen to avoid atmospheric absorption lines – around 6, 10, 19, 37, and 89 GHz, and atmospheric sounding channel families around 23, 50-60, 166, and 183 GHz. The instrument rotates continuously at 31.6 rpm on an axis perpendicular to the ground, taking observations along nearly semi-circular arcs centered on the satellite ground track. Successive arcs scanned by a single sensor channel are separated by about 12.5 km along-track (depending on satellite altitude). Calibration data is collected from a source (hot) and deep-space reflector (cold) viewed during the non-earth-viewing portion of the rotation cycle. Each observation (or sample) requires a finite sensor integration time which also transforms the sensor instantaneous field of view (IFOV) – the projection, or footprint, of the antenna gain pattern on the earth – into an observation effective field of view (EFOV). The start of each sample is separated by the sample time which is slightly longer than the integration time. The sample time is  $t_s = 1.2659$  ms for all channels with the exception of 10 GHz (exactly  $2t_s$ ) and 6.8 GHz ( $4t_s$ ). All samples fall on one of three main-reflector scan-arcs or a single secondary-reflector scan arc (166 and 183 GHz channels families only).

### **2.2. CMIS Channels Used in the Core Physical Inversion Module**

The Core Module is designed to simultaneously retrieve temperature and water vapor profiles along the sensor view path, cloud liquid water (CLW), cloud top pressure, skin temperature and surface emissivity.

Table 2-1 lists the CMIS channels used in the Core Physical Inversion Module. (see also [EN #9](#) response.) Figure 2-1 shows the microwave spectra of water vapor and oxygen absorption (spectra calculated for a temperature of 296 K and a pressure of 1013 mb).



## OVERVIEW AND BACKGROUND INFORMATION

Table 2-1: CMIS channels used in the Core Physical Inversion Module.

Channel Name	RF Center Frequency (GHz)	Polarization	RF Passband (3 dB) (MHz)
6V	6.625	V	350
6H	6.625	H	350
10V	10.65	V	100
10H	10.65	H	100
18V	18.7	V	200
18H	18.7	H	200
23V	23.8	V	400
23H	23.8	H	400
36V	36.5	V	1000
36H	36.5	H	1000
60VA	50.300	V	134
60VB	52.240	V	1280
60VC	53.570	V	960
60VD	54.380	V	440
60VE	54.905	V	350
60VF	55.490	V	340
60VG	56.660	V	300
60VJ	59.380	V	280
60VK	59.940	V	440
89V	89.0	V	4000
89H	89.0	H	4000
166V	166.0	V	3000
183VA	$183.31 \pm 0.7125$	V	1275 ea
183VB	$183.31 \pm 3.1$	V	3500 ea
183VC	$183.31 \pm 7.7$	V	4500 ea

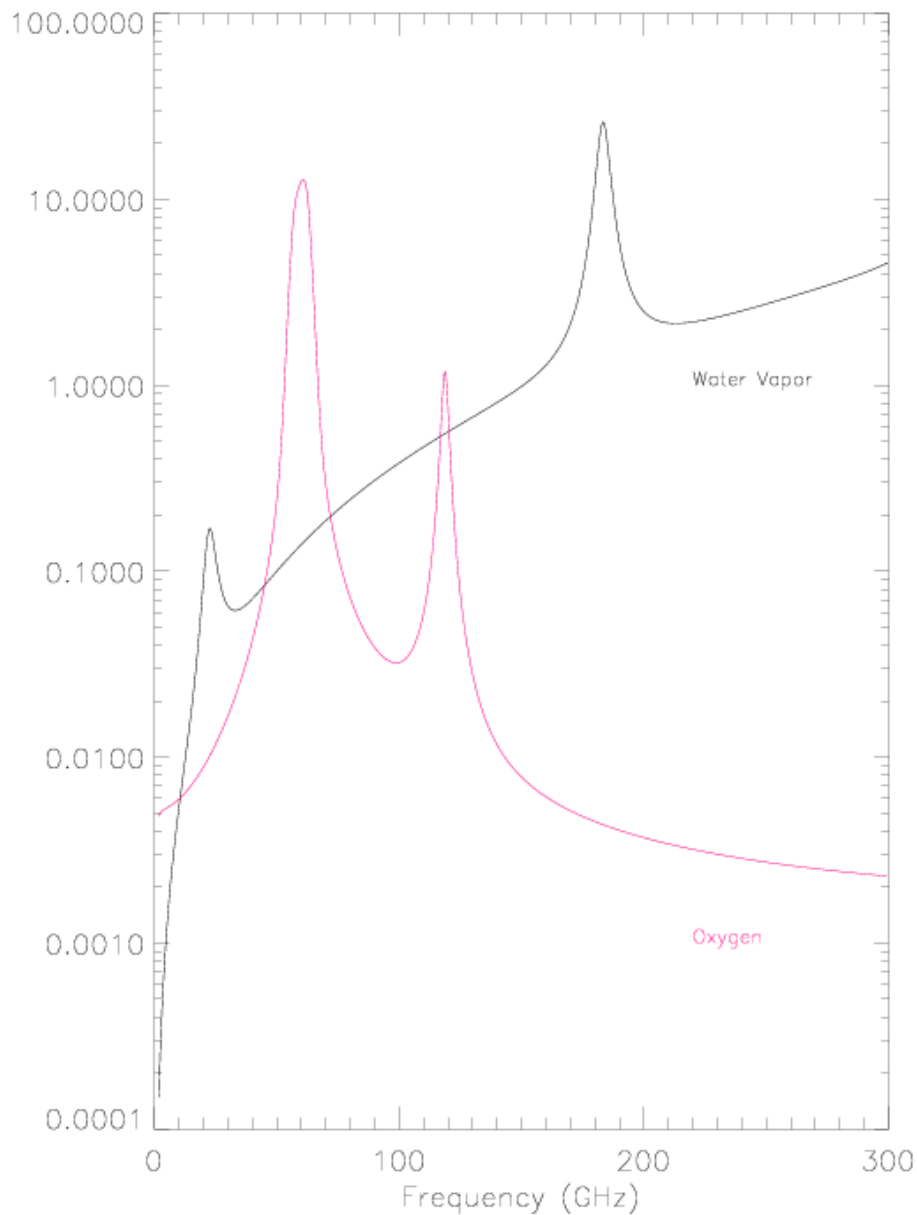


Figure 2-1: Absorption Spectra of Water Vapor and Oxygen in the Microwave.

To visualize the sensitivity of brightness temperature to temperature and water vapor, we computed the temperature and humidity Jacobians for the entire microwave spectrum. The Jacobian is the derivative of the brightness temperature with respect to the atmosphere and surface parameters. Figure 2-2 shows a tropical case where the surface emissivity ( $\epsilon$ ) is 0.5 and presents the Jacobians in temperature (top) and humidity (bottom) in clear (left) and cloudy (right) conditions. A tropical case with  $\epsilon = 0.9$  is shown in Figure 2-3.

Water vapor profiling channels are located on the 183.31 GHz line. The weak 22.235 GHz is used for lower tropospheric and total column water vapor. Away from these lines, water vapor

absorption is dominated by the continuum. The continuum absorption increases as  $\nu^2$  (where  $\nu$  is the frequency) and is therefore much higher at 150 GHz than at 37 GHz. The sensitivity to water vapor at any given level is driven by the column atmospheric absorption above this level. Therefore, the frequencies that contribute the most information will differ depending on the atmospheric conditions.

The primary channels for temperature profiling are located in the 50-60 GHz range. As shown by the sensitivity plots of Figure 2-2 and Figure 2-3, the window channels where absorption is dominated by the water vapor continuum, as well as channels located on the 22.235 and 183 GHz water vapor lines, also have high sensitivity to temperature. Thus these channels contribute significantly to the tropospheric temperature retrievals when included in the inversion. The relative contribution of these channels is higher for a moist atmosphere than it is for a dry atmosphere (see Figure 2-2 and Figure 2-3). Provided that the algorithm correctly takes nonlinearities into account, improved performance can be obtained in the lower troposphere by exploiting the temperature sensitivity of these channels.

Over the spectral range of the CMIS measurements, cloud droplets of the order of 50  $\mu\text{m}$  or less are in the Rayleigh absorption regime. In non-precipitating clouds, absorption is proportional to the cloud liquid water content and scattering can be neglected. The 50 GHz and 183 GHz measurements cannot distinguish between perturbations in temperature or water vapor concentration and the presence of clouds. Therefore, it is necessary to correct the measurements for the presence of clouds in the sounding channels by using the information from the window channels. The combination of 19/22 GHz, 37 and 89 GHz dual polarized channels is very effective for this purpose. These channels are used to derive both cloud liquid water amount and radiating temperature of the cloud (or cloud top height if temperature profile is known). When the cloud top height is specified from external data (e.g. VIIRS) it is possible to derive information about effective thickness of the cloud. It is also noteworthy that the temperature sensitivity of the CMIS measurements increases significantly within the clouds, and decreases below the cloud, due to the increased atmospheric opacity as shown in Figure 2-2 and Figure 2-3.

# OVERVIEW AND BACKGROUND INFORMATION

CLW=0.0

CLW=0.5

Temp.

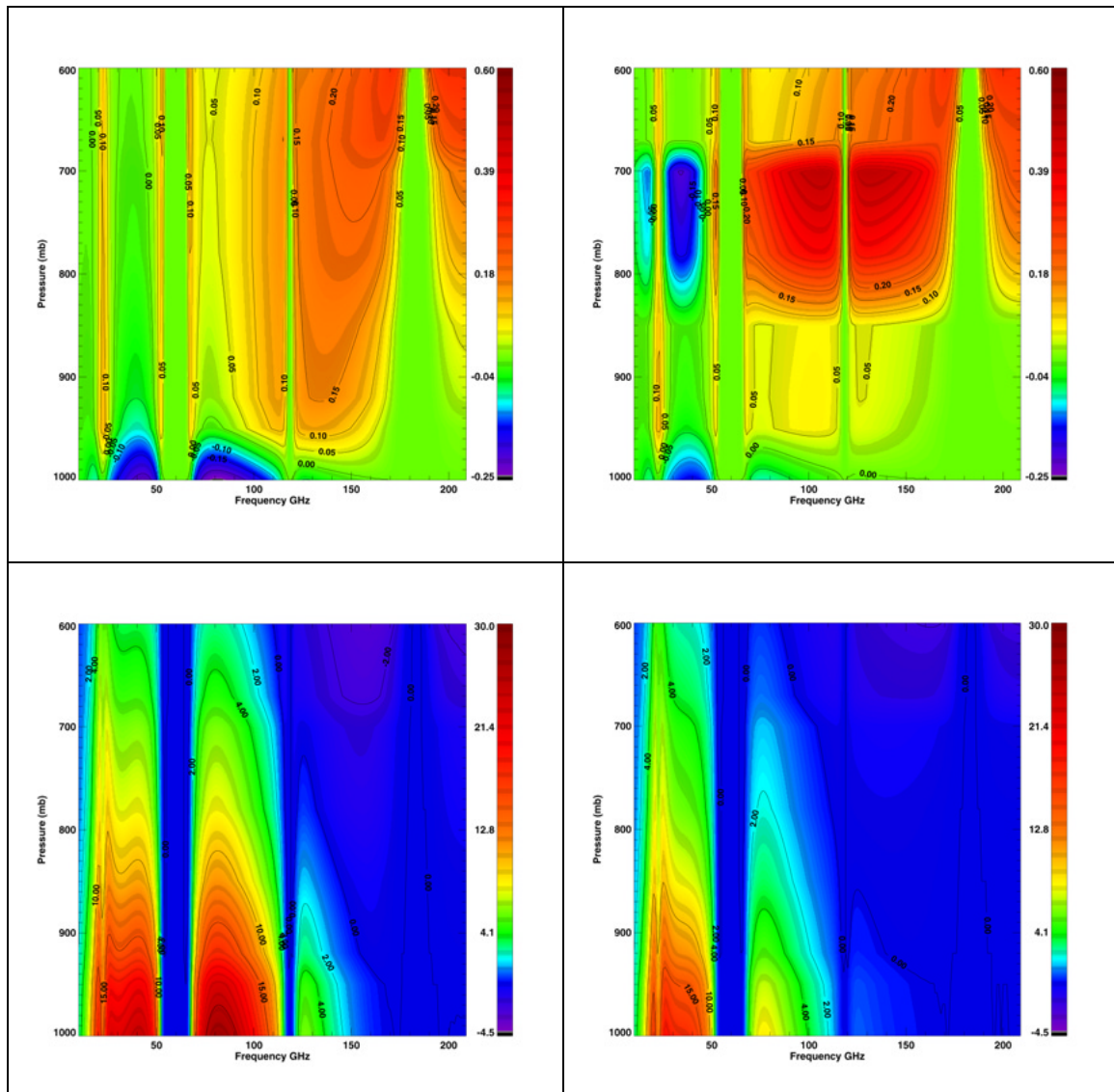
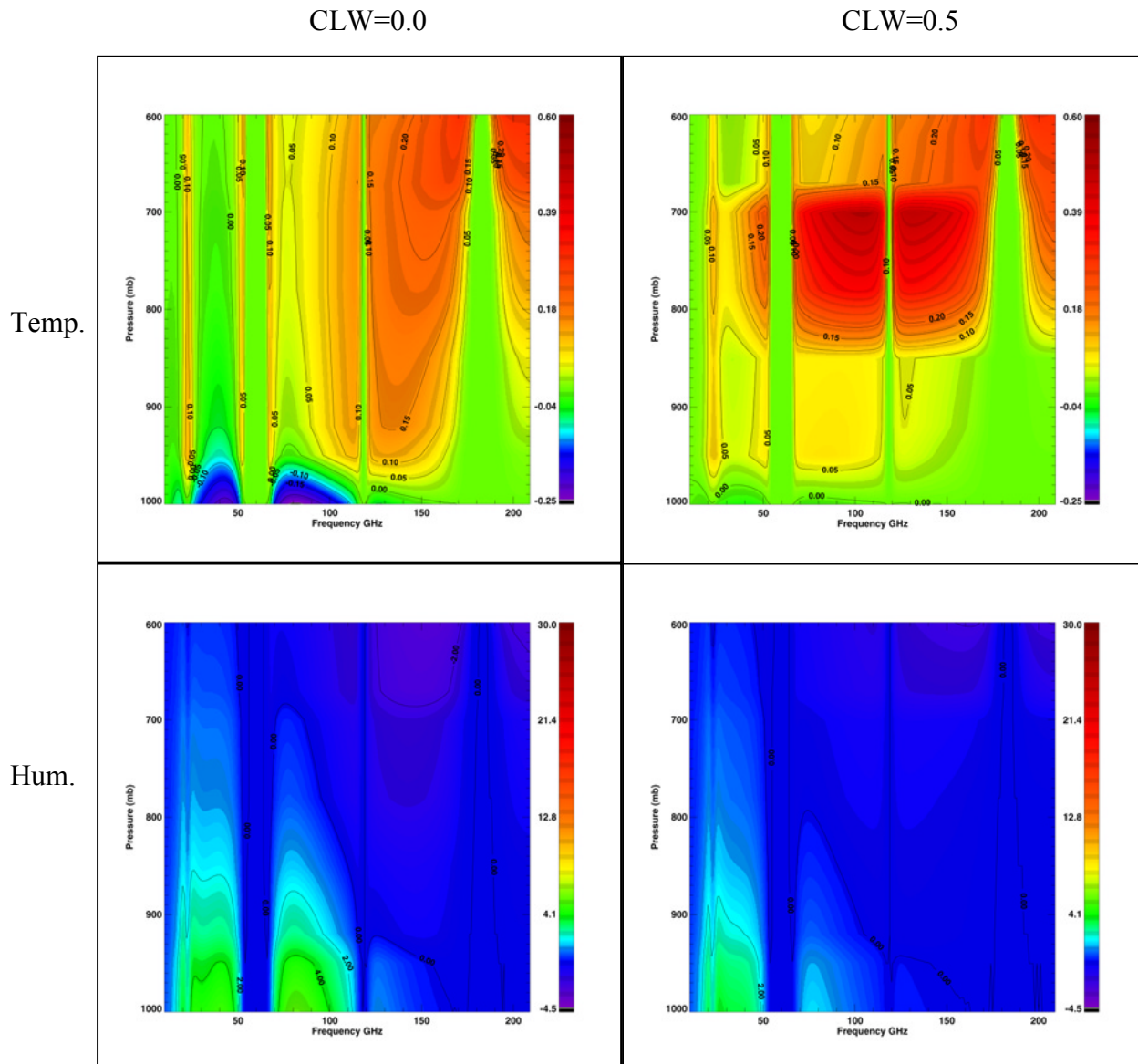


Figure 2-2:  $\varepsilon=0.5$ . Temperature and Humidity Jacobians.

Figure 2-3:  $\varepsilon=0.9$  - Temperature and Humidity Jacobians.

The surface emissivity also affects the retrieval performance. In particular, the sensitivity of measurements to lower tropospheric water vapor and cloud liquid water depends highly on the magnitude of the surface emissivity. Figure 2-2 and Figure 2-3 show examples of Jacobians for temperature and water vapor computed for different values of the surface emissivity. Sensitivity to water vapor is very low over highly emissive surfaces (e.g., vegetated surfaces) due to low surface/atmosphere contrast in the lowest 2 km. By comparison, atmospheric temperature Jacobians are relatively insensitive to the magnitude of surface emissivity. The algorithm must be able to take into account the change in sensitivity of the measurements with respect to a perturbation in the desired parameters.

Over land, the surface emissivity may be highly variable both spatially and temporally. For many areas of the globe this variability makes it difficult to obtain good *a priori* knowledge of the surface emissivity. If the algorithm is to be able to operate optimally under all conditions in the absence of *a priori* knowledge of the surface background, information on surface emissivity must be extracted from the spectral measurements.

This problem can, in principle, be dealt with by training an algorithm for different surface types and use surface pre-classification to select appropriate algorithm or set of coefficients. For example, this type of approach is used for surface temperature retrieval from SSMIS [Aerojet Report, 1994] where a series of radiance tests is performed prior to doing the retrieval in order to determine the surface type. However, the number of surface types that can be unequivocally distinguished is limited by the impact atmospheric variability and such an approach is not immune to misclassification.

In our baseline approach, the surface emissivity is retrieved simultaneously with the other geophysical parameters in an iterative solution process in which the Jacobians are re-evaluated at each iteration. The same algorithm inherently takes into account the change in sensitivity of the measurements to the retrieved parameter (above requirements are automatically satisfied). The proposed use of a single “global” land/snow/ice surface emissivity background as default for the baseline algorithm avoids the difficulties associated with misclassification of surface type and makes the algorithm robust. One unique advantage of this approach is that it provides the potential for atmospheric retrieval capabilities over snow and ice, where all current approaches are deemed to fail.

Note that the approach does not preclude one from using pre-classification. The studies conducted so far show no substantial benefit of such pre-classification when classification is attempted from the radiances themselves. In addition, the algorithm can accommodate *a priori* surface information when available and provides the quality control necessary to detect inadequacies in the supplied information (due e.g. to changes in the surface conditions).

The process for retrieving surface emissivity takes advantage of the fact that unlike the surface temperature signal, the reflective component of the surface contribution contains the spectral characteristics of the downwelling atmospheric emission. This component is used to distinguish surface temperature from emissivity signal. Close examination of the Jacobians shows that as

atmospheric opacity increases, the emissivity Jacobians in the window regions decrease more rapidly than temperature Jacobians.

The difference in opacity at 19 and 23 GHz due to the 22.235 GHz water vapor line is particularly useful. Due to their closeness in frequency, the emissivity is nearly equal for these channels. The dual polarization available on CMIS at 19 and 23 GHz allows one to solve for surface temperature, total precipitable water as well as surface emissivity from those frequencies. The capability to separate surface temperature from emissivity depends on the water vapor load and is expected to decrease in the drier atmospheres. Because the microwave spectrum contains few sharp features in the atmospheric absorption spectrum, the overall retrieval performance depends largely on the spectral correlation of the surface emissivity which drives the number of degrees of freedom in the problem.

### 3. Core Physical Inversion Algorithm Processing Outline

#### 3.1. Overview of Core Physical Inversion Module

The Core Module consists of a forward radiative transfer model and a radiance inversion model. The radiative transfer model is used to compute radiances given various parameters (e.g., temperature and water vapor profiles, surface properties, cloud properties, etc...) and compute the derivatives of radiance with respect to the particular parameters of interest. The inversion model is used to convert the difference between measured radiances and modeled radiances into changes in various atmospheric parameters. The background *a priori* estimate is derived from a number of sources. Radiosonde data are used to construct global ocean and land based backgrounds for the temperature and moisture profiles. A microwave emissivity model based on the work of Wilheit [Wilheit, 1979; Kohn and Wilheit, 1995] is used to provide a background for open ocean surfaces. The land emissivity background is currently derived from SSM/I observations [Prigent *et al.*, 1997], by inter/extrapolation of surface emissivities to standard frequencies and to CMIS channels, as discussed in Appendix 3. (See also [EN #83](#) response.) The maximum likelihood inversion has the capability to incorporate external information. NWP-derived temperature profiles, moisture profiles, and surface parameters can be used to improve the background.

The flow diagram presented in Figure 3-1 shows the entire process of the Core Physical Retrieval Module. It is divided into 3 parts: an initialization process followed by an input and pre-processing module. The retrieval process follows.

#### 3.2. Core Module Outputs

The Core Module Outputs are listed in Table 3-1.

Table 3-1: Core Module Outputs.

Parameters	Representation
Atmospheric Temperature	Temperature profile at 40 pressure levels.
Water vapor	Mixing Ratio at 40 pressure levels.
Tskin	
Surface Emissivity	For each channel.
Water clouds	CLW and cloud top pressure - Sensitivity to thickness when external constraint on cloud top pressure (from e.g. VIIRS) is available
Ice clouds	Requires treatment of scattering IWP, mode radius, cloud top pressure



### 3.3. Core Module Inputs

#### 3.3.1. Required Sensor Inputs

The Core Module uses footprint matched CMIS radiances (see details in ATBD for CMIS EDRs - Volume 1: Overview - Part 2: Footprint Matching and Interpolation) to insure that all the channels sense the same volume of atmosphere.

#### 3.3.2. Ancillary Data Inputs

##### Required Databases

There are 2 forms of ancillary data that are required for the retrievals. The first form is of the “static data base” type, e.g. information that is provided once and for all, and may or may not be updated as better information becomes available. The second form is of the “dynamic data base” type and is updated on a regular basis.

##### *Required “Dynamic Database”*

- External data from NWP model (surface pressure and virtual temperatures) to fix lower boundary of retrieval and define pressure profile.

##### *Required External “Static Database”*

- Digital Elevation Map for lower boundary determination: ~1km resolution map like the GTOPO30 provided by USGS. This DEM has a horizontal grid spacing of 30 arc seconds and was derived from several raster and vector sources of topographic information. The absolute vertical accuracy of GTOPO30 varies by location according to the source data. Generally, the areas derived from the raster source data have higher accuracy than those derived from the vector source data. The full resolution 3-arc second DTED and USGS DEM's have a vertical accuracy of + or - 30 meters linear error at the 90 percent confidence level (Defense Mapping Agency, 1986; U.S. Geological Survey, 1993). More information can be found on <http://edcwww.cr.usgs.gov/landdaac/gtopo30/gtopo30.html>
- A 1 km global Land/Ocean mask (like the Digital Terrain Elevation Data (DTED) from NIMA; more information on <http://www.nima.mil/geospatial/products/DTED/dted.html>) to set up the surface emissivity first guess.

##### *Optional Data for Performance Enhancement*

- Cloud top pressure from VIIRS

## CORE PHYSICAL INVERSION ALGORITHM PROCESSING OUTLINE

### -VIIRS radiances

- to set up clear/cloudy flags in CMIS footprints
- to determine the degree of inhomogeneity in a scene

-NCEP 6 hour forecast for temperature and water vapor can be used as an optional background for retrieval instead of climatology. An error covariance matrix for these profiles is also required (generated from thousands of past profiles and updated every couple of years or so).

# CORE PHYSICAL INVERSION ALGORITHM PROCESSING OUTLINE

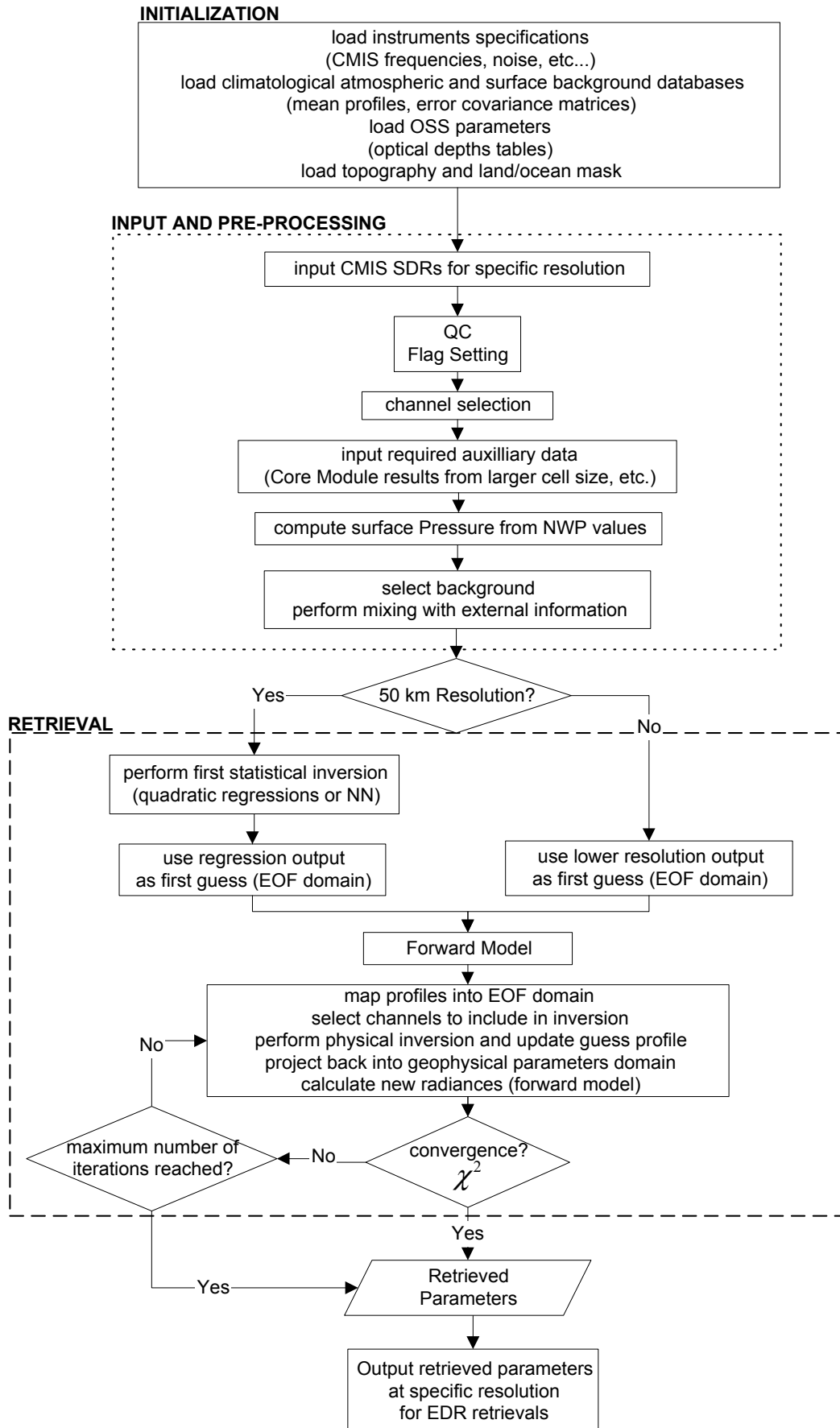


Figure 3-1: Core Physical Inversion Module Flow Diagram.

## 4. Theoretical Description of the Core Physical Inversion Algorithm

### 4.1. Forward Modeling

One of the most critical modules for a physical inversion algorithm is the radiative transfer (RT) model (or forward model). The RT model is used to accurately compute the radiances corresponding to a given atmospheric state and the derivatives (or Jacobian) of the radiances with respect to atmospheric and surface parameters for use by the inversion module. In addition to providing for an accurate treatment of the atmosphere, the forward model must often meet stringent requirements for computation time. In this section we introduce the microwave radiative transfer equations and describe how the newly developed Optimal Spectral Sampling (OSS) technique may be applied in order to construct a highly accurate, computationally efficient, forward model for use in the Core Retrieval algorithm. Because the OSS technique is based on monochromatic computations, it has an advantage over other forms of fast-model parameterizations in that it provides the required derivatives with little extra computation time.

#### 4.1.1. Radiative Transfer Equation

The radiative transfer equation (RTE) used in the microwave region treats the atmosphere as a homogeneous, plane-parallel, non-scattering medium. The brightness temperature,  $R_\nu$ , at a given frequency  $\nu$  is computed using the Rayleigh-Jeans approximation as:

$$R_\nu \cong \varepsilon_\nu \Theta_s T_{s,\nu} + \int_{p_s}^0 \Theta(p) \frac{\partial T_\nu(p, \theta_u)}{\partial p} dp + (1 - \varepsilon_\nu) T_{s,\nu} \left[ \int_0^{p_s} \Theta(p) \frac{\partial T_\nu^*(p, \theta_d)}{\partial p} dp + T_\nu^*(0, \theta_d) \Theta_c \right] \quad (1)$$

where  $\theta(p)$  is the atmospheric temperature at pressure  $p$ ,  $T_\nu(p, \theta_u)$  is the total transmittance due to molecular species and cloud liquid water from pressure  $p$  to space at the satellite viewing angle  $\theta_u$ ,  $T_\nu^*(p, \theta_d)$  is the transmittance from surface to pressure  $p$  at computational angle  $\theta_d$ ,  $\varepsilon_\nu$  is the surface emissivity, and  $\Theta_c$  is the cosmic radiation term ( $\Theta_c = 2.73$  K). In the microwave, over both land and ocean, the surface is treated as specularly reflective, i.e.  $\theta_d = \theta_u$ .

#### 4.1.2. Overview of the OSS Method

The Optimal Spectral Sampling (OSS) method is a generalized formulation for the forward radiative transfer problem that is applicable for any type of instrument configuration from the microwave through the ultraviolet regions of the spectrum. With OSS, the radiative transfer is computed at selected frequency locations within the spectral interval spanned by the instrument

function and the results are combined linearly in such a way as to accurately represent the radiance for each instrument channel. To accomplish this, the convolution of the monochromatic space-to-level transmittance with the spectra gain function (SGF) is approximated as a sum of monochromatic transmittances computed at selected spectral points within the domain spanned by the SGF:

$$T_{\Delta\nu} = \int_{\Delta\nu} \phi_\nu T_\nu d\nu \approx \sum_i w_i T_{\nu_i} \quad (2)$$

where  $\phi_\nu$  represents an instrument function which is assumed effectively zero outside the interval  $\Delta\nu$  and where  $\nu_i \in \Delta\nu$ . The optimal selection of the  $\nu_i$ 's and the computation of the weights,  $w_i$ , is performed off-line while comparing the values of the channel radiances with and without the approximation of Equation (3). The spectral transmittances ( $T_\nu$  and  $T_{\nu_i}$ ) are computed with a reference model [Rosenkranz, 1995]. The optimization procedure minimizes the *rms* difference between the “exact” and approximate radiances calculated for an ensemble of globally representative atmospheric profiles over the full range of surface emissivities. The following constraints are applied in order to ensure a physical solution:

$$w_i > 0 \text{ and } \sum_i w_i = 1 \quad (3)$$

The numerical accuracy of the OSS model is pre-selectable and implicitly determines the number of points to approximate the exact radiances in each channel.

Table 4-1 shows the number of OSS points used in the current modeling of CMIS radiances. The *rms* threshold for the spectral point selection was set to 0.05 K. The channel number corresponds to our internal (not the official) channel numbering system.

Table 4-1: Number of Spectral Points Selected for CMIS.

Channel #	Center Frequency (GHz)	Number of OSS Frequencies	RMS (K)
1	6.800	1	0.0005
2	6.800	1	0.0005
3	10.650	1	0.0016
4	10.650	1	0.0016
5	10.650	1	0.0016
6	10.650	1	0.0016
7	18.700	1	0.0143
8	18.700	1	0.0143
9	18.700	1	0.0143
10	18.700	1	0.0143
11	18.700	1	0.0143
12	18.700	1	0.0143
13	23.800	1	0.0033
14	23.800	1	0.0033
15	36.500	1	0.0066
16	36.500	1	0.0066
17	36.500	1	0.0066
18	36.500	1	0.0066
19	89.000	2	0.0004
20	89.000	2	0.0004
21	166.000	1	0.0277
22	183.310	3	0.0233
23	183.310	4	0.0132
24	183.310	3	0.0085
28	50.300	1	0.0083
29	52.240	3	0.0205
30	53.570	7	0.0049
31	54.380	4	0.0033
32	54.905	2	0.0313
33	55.490	2	0.0212
34	56.660	1	0.0393
35	59.380	3	0.0040
36	59.940	3	0.0019
37	60.371	1	0.0267
38	60.414	2	0.0367
39	60.512	2	0.0372
40	62.448	2	0.0130

Figure 4-1 and Figure 4-2 compare the brightness temperatures for this set of CMIS channels obtained with the OSS approach and the commonly used “central frequency” approximation with the “exact” calculations from Rosenkranz’s model. The *rms* differences between the models do not include errors due to optical depth interpolation. These errors can be made arbitrarily small by increasing the number of entries in the optical depth look-up tables (see paragraph 4.1.3).

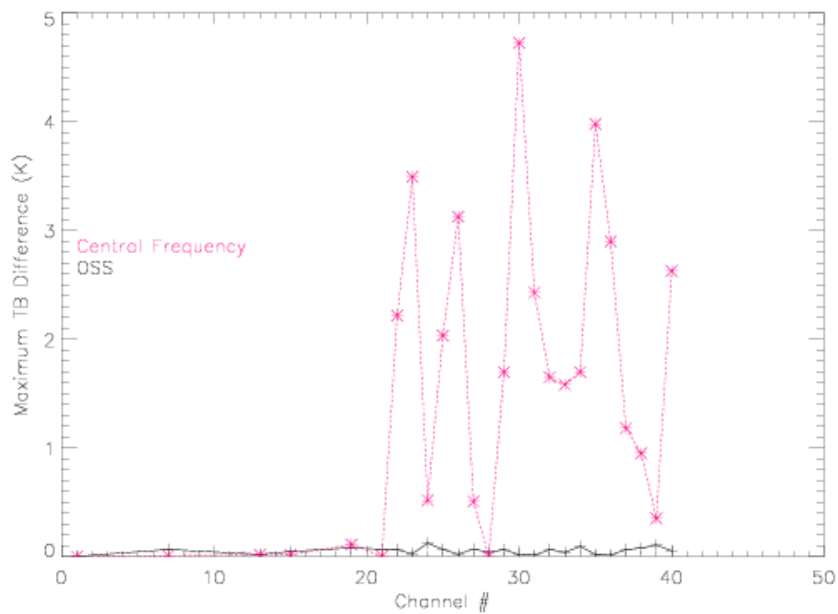


Figure 4-1: Comparison OSS/Central Frequency (Maximum Differences).

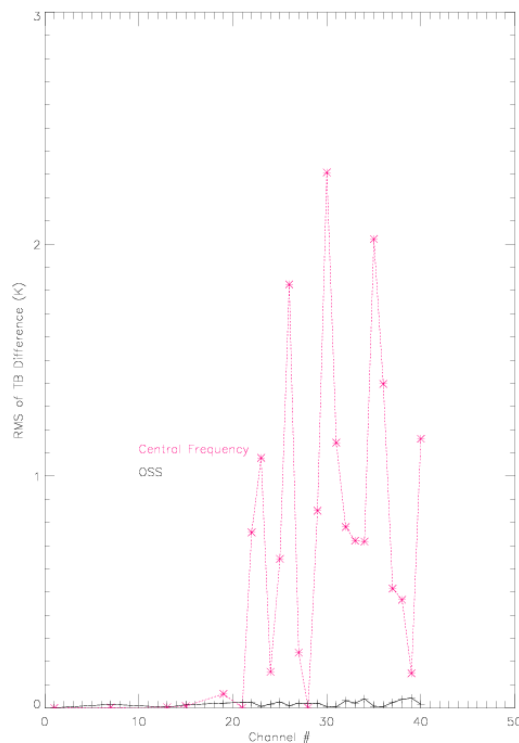


Figure 4-2: Comparison OSS/Central Frequency (*rms*).

#### 4.1.3. Transmittance Model

The OSS model computes transmittances from optical depths. For the fixed gases, the OSS model makes use of pre-stored monochromatic layer optical depths at the selected wavenumber locations. The optical depths are stored at a set of temperature and water vapor amounts for each pressure layer used in the discrete radiative transfer model. For each layer, the temperature and

water vapor ranges span the values expected for that layer based on the NOAA-88 atmospheric profile databases (see Appendix 1 for more details about this dataset). This domain is sampled uniformly and the optical depths are stored at an array of 20 temperatures and 20 water vapor amounts.

For a given layer, each optical depth is linearly interpolated to the layer temperature and water vapor amount. Water vapor is handled similarly to the fixed gases, but the tabulated parameter is the absorption coefficient. After the coefficient has been interpolated linearly in temperature and water vapor amount, it is multiplied by the water vapor amount to obtain the optical depth. By this procedure, the quadratic dependence of continuum absorption can be represented.

The total optical depth due to gases is computed as:

$$\tau_l^0 = \tau_{O_2}(\bar{p}_l, \theta_l, \omega_{O_2}) + \tau_{H_2O}(\bar{p}_l, \theta_l, \omega_{H_2O}) \quad (4)$$

where  $\tau$  is the optical depth,  $\omega$  is the absorber amount,  $p$  is the layer pressure and  $\theta$  is the temperature. The calculations are done using the Rosenkranz model [Rosenkranz, 1995].

#### 4.1.4. Radiance Calculation

##### 4.1.4.1 Overview of the Method

Since the OSS method is a monochromatic approach to the radiative transfer, the gradient of the forward model with respect to all relevant atmospheric/surface parameters can be computed efficiently using an analytical scheme. Computation of radiances and derivatives with the OSS method uses a generic recursive scheme developed for the modeling of upward, downward-looking and limb-viewing instruments and used in atmospheric retrievals from CIRRIS [Miller *et al.*, 1999].

Figure 4-3 defines the numbering conventions for the layered atmosphere.  $T_l$  and  $T_l^*$  denote the transmittances from space to level  $l$  and surface to level  $l$  computed along the upward (u) and downward (d) atmospheric paths, defined as:

$$T_l = \exp\left(-\sum_{i=1}^l \tau_i^0 \sec \theta_{obs}\right) \quad (5)$$

and:

$$T_l^* = \exp\left(-\sum_{i=1}^{N-l} \tau_{l+i}^0 \sec \theta_d\right) \quad (6)$$



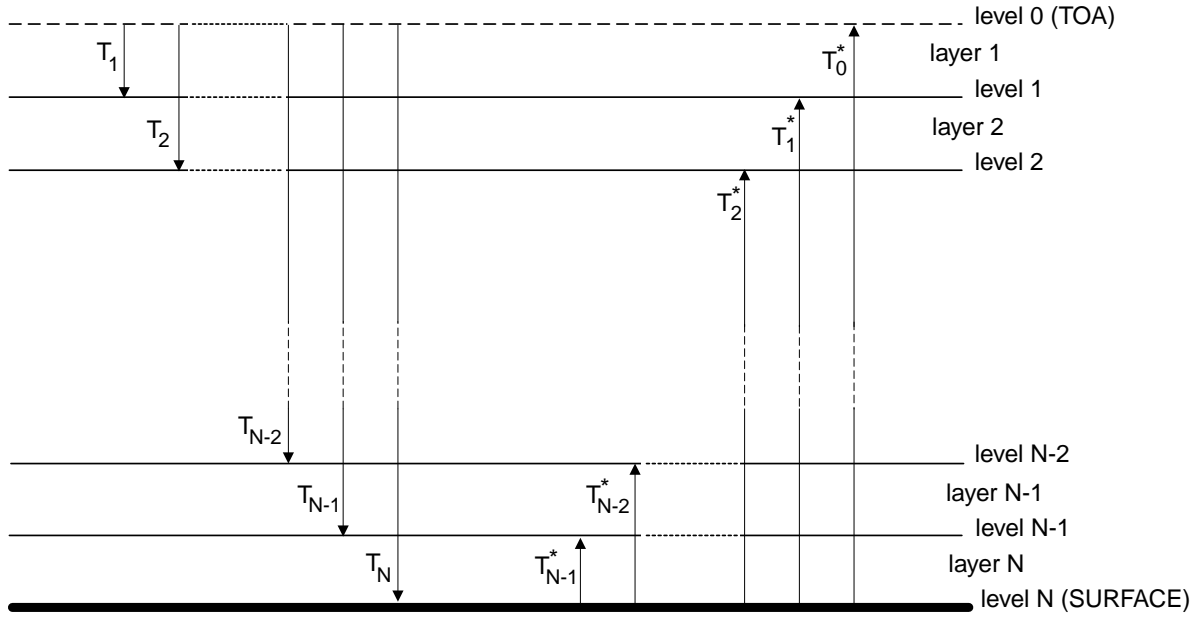


Figure 4-3: Schematic diagram showing the numbering convention for the atmospheric layers used by OSS, where  $T$  refers to transmittances, level 0 represents the top of the atmosphere (TOA) and level  $N$  the surface.

Radiances in clear conditions are computed using the following expression derived using a discrete form of the radiative transfer equation:

$$R_v = \sum_{i=1}^N (T_{v,i-1} - T_{v,i}) B_{v,i}^+ + \varepsilon_{vs} T_{v,N} B_{v,s}^+ + (1 - \varepsilon_{vs}) T_{v,N} \sum_{i=1}^N (T_{v,i}^* - T_{v,i-1}^*) B_{v,i}^- \quad (7)$$

where  $B_v^\pm$  represents the upward and downward Planck emission of the layer/surface and  $\varepsilon_{vs}$  is the surface emissivity. Derivatives of  $R_v$  with respect to constituents concentration or temperature in layer  $l$  are obtained by differentiating the previous equation:

$$\begin{aligned} \frac{\partial R}{\partial X_l} = & -\frac{\partial \tau_l^0}{\partial X_l} \left\{ \left[ -T_l B_l + \sum_{i=l+1}^N (T_{i-1} - T_i) B_i + T_N \varepsilon_s B_s + (1 - \varepsilon_s) T_N \sum_{i=1}^N (T_i^* - T_{i-1}^*) B_i \right] \sec \theta_{obs} \right. \\ & \left. + \left[ -(1 - \varepsilon_s) T_N T_{l-1}^* B_l + (1 - \varepsilon_s) T_N \sum_{i=1}^{l-1} (T_i^* - T_{i-1}^*) B_i \right] \sec \theta_d \right\} \\ & + \frac{\partial B_l^+}{\partial X_l} (T_{l-1} - T_l) + (1 - \varepsilon_s) T_N \frac{\partial B_l^-}{\partial X_l} (T_l^* - T_{l-1}^*) \end{aligned} \quad (8)$$

or, by introducing the two-path attenuation from level  $l$  to space,  $T_l' = (1 - \varepsilon_s) T_N T_l^*$ :

$$\begin{aligned}
 \frac{\partial \mathcal{R}}{\partial X_l} = & -\frac{\partial \tau_l}{\partial X_l} \left[ -T_l B_l + \sum_{i=l+1}^N (T_{i-1} - T_i) B_i + T_N \varepsilon_s B_s + \sum_{i=1}^N (T'_i - T'_{i-1}) B_i \right. \\
 & \left. - T'_{l-1} B_l + \sum_{i=1}^{l-1} (T'_i - T'_{i-1}) B_i \right] \\
 & + \frac{\partial B_l^+}{\partial X_l} (T_{l-1} - T_l) + \frac{\partial B_l^-}{\partial X_l} (T'_l - T'_{l-1})
 \end{aligned} \tag{9}$$

where  $X_l$  stands for either  $\theta_l$  or  $\omega_l$ .

This procedure uses the fact that a perturbation in temperature or constituent concentration in any given layer of the atmosphere does not affect the emission in the atmospheric slab comprised between this layer and the observer. Therefore, derivatives can be obtained at low cost if the RTE is integrated by adding layers sequentially in the direction of the observer. The procedure is more apparent by introducing the quantities  $\Sigma_l^-$  and  $\Sigma_l^+$  defined as the contribution to the observed radiance of the downward emission (reflected at the surface) from the atmosphere above level  $l$  and the contribution of the atmosphere below level  $l$  plus reflected downward radiation, e.g.:

$$\Sigma_l^- = \sum_{i=1}^l (T'_i - T'_{i-1}) B_i^- \tag{10}$$

and:

$$\Sigma_l^+ = \sum_{i=l+1}^N (T_{i-1} - T_i) B_i^+ + \varepsilon_s T_N B_s + \sum_{i=1}^N (T'_i - T'_{i-1}) B_i^- \tag{11}$$

where (two-path transmittance):

$$T'_l = (1 - \varepsilon_s) T_N T_l^* \tag{12}$$

Using the definitions of the previous equations, one can write:

$$\begin{aligned}
 \frac{\partial \mathcal{R}}{\partial X_l} = & \left[ \frac{\partial \mathcal{R}}{\partial X_l} \right]_u + \left[ \frac{\partial \mathcal{R}}{\partial X_l} \right]_d \\
 = & \left[ \frac{\partial \tau_l}{\partial X_l} (-\Sigma_{l-1}^- + B_l^- T'_{l-1}) + \frac{\partial B_l^-}{\partial X_l} (T'_{l+1} - T'_l) \right] \\
 & + \left[ \frac{\partial \tau_l}{\partial X_l} (-\Sigma_l^+ + B_l^+ T_l) + \frac{\partial B_l^+}{\partial X_l} (T_l - T_{l-1}) \right]
 \end{aligned} \tag{13}$$

In the current version of the CMIS algorithm, layer emission is computed from the average Planck emission over the layer ( $\bar{B}_l$ ).

This approximation is adequate as long as layers are not optically thick, e.g. vertical pressure grid is sufficiently fine. The trade-off between coarseness of the vertical sampling and the use of a more sophisticated approach such as linear-in-tau approximation has not been evaluated yet. It results in approximation that  $\partial B_l / \partial \tau_l = 0$ .

#### 4.1.4.2 Practical Implementation

In a first pass, at any given wavenumber, the algorithm computes the profile of transmittance from space. The recursive procedure for the computation of radiances and analytical derivatives follows directly the last equation written above.

1) Initialization: set  $\Sigma_0^- = 0$ .

2) If  $(1 - \varepsilon_s)T_N > 10^{-4}$ , add layers successively from TOA down to surface.

Update  $\Sigma_l^-$  at each step and compute first part of radiance derivatives.

$$\left[ \frac{\partial R}{\partial \tau_l} \right]_d = -\Sigma_{l-1}^- + \bar{B}_l T'_{l-1} \quad (14)$$

and:

$$\left[ \frac{\partial R}{\partial \Theta_l} \right]_d = \frac{\partial \bar{B}_l}{\partial \Theta_l} (T'_l - T'_{l-1}) \quad (15)$$

$$\Sigma_l^- = \Sigma_{l-1}^- + (T'_l - T'_{l-1}) \bar{B}_l \quad (16)$$

3) Add surface term and compute derivative with respect to surface emissivity and temperature.

$$\frac{\partial R}{\partial \Theta_s} = T_N \varepsilon_s \frac{\partial B_s}{\partial \Theta_s} \quad (17)$$

and:

$$\frac{\partial R}{\partial \varepsilon_s} = T_N B_s - \Sigma_N^- / (1 - \varepsilon_s) \quad (18)$$

$$\Sigma_N^+ = \Sigma_N^- + T_N \epsilon_s B_s \quad (19)$$

4) Update  $\Sigma_l^+$  by adding layers from surface up to TOA and compute second part of derivatives.

$$\frac{\partial R}{\partial \tau_l} = -\Sigma_l^+ + \bar{B}_l T_l + \left[ \frac{\partial R}{\partial \tau_l} \right]_d \quad (20)$$

and:

$$\frac{\partial R}{\partial \Theta_l} = \frac{\partial \bar{B}_l}{\partial \Theta_l} (T_{l-1} - T_l) + \left[ \frac{\partial R}{\partial \Theta_l} \right]_d \quad (21)$$

$$\Sigma_{l-1}^+ = \Sigma_l^+ + (T_{l-1} - T_l) \bar{B}_l \quad (22)$$

4) Set  $R_v = \Sigma_0^+$  and compute derivatives with respect to layer amounts for water vapor as:

5)

$$\frac{\partial R_v}{\partial w_l} = \frac{\partial R_v}{\partial \tau_l} \cdot \frac{\partial \tau_l}{\partial w_l} \quad (23)$$

#### 4.1.4.3 Microwave Cloud Liquid Water

Cloud optical depths and their derivatives are computed in a subroutine that outputs a profile of cloud optical depth per layer and the derivatives of the layer optical depths with respect to three cloud parameters: total liquid water ( $Q$ ), cloud top pressure ( $p_t$ ), and cloud thickness ( $\Pi$ ).

The layer optical depths are computed as:

$$\tau_{ij} = Q k_{ci}(\bar{T}_j) f \frac{\Delta_j}{\Pi} \quad (24)$$

where  $\tau_{ij}$  is the optical depth in layer  $j$  for frequency index  $i$ ,  $k_c$  is the mass absorption coefficient for liquid water,  $\bar{T}_j$  is the average temperature of the cloud within layer  $j$ ,  $f$  is the cloud fraction within the field of view (FOV).

The cloud proportion that is in layer  $j$  is represented by  $\Delta_j / \Pi$ , where  $\Delta_j$  is given in Table 4-2 and cloud base is  $p_b = p_t + \Pi$ . If the entire cloud depth is within layer  $j$ , then  $\Delta_j = \Pi$ .

The mass absorption coefficient is computed from the model of Liebe *et al.* [Liebe *et al.*, 1991], with the alternative, exponential formulation for the primary relaxation frequency dependence on temperature:

$$\gamma_1 = 20.1 \exp(7.88\theta) \quad (25)$$

where:

$$\theta = 1 - \frac{300 \text{ K}}{T} \quad (26)$$

The derivative with respect to total cloud liquid is given as:

$$\frac{\partial \tau_{ij}}{\partial Q} = k_{ci}(\bar{T}_j) f \frac{\Delta_j}{\Pi} \quad (27)$$

As a practical matter, the derivative is computed and then  $\tau$  is computed as  $Q \frac{\partial \tau_{ij}}{\partial Q}$ .

The derivatives with respect to cloud top and cloud thickness are respectively:

$$\frac{\partial \tau_{ij}}{\partial p_t} = Q k_{ci}(\bar{T}_j) f \frac{1}{\Pi} \frac{\partial \Delta_j}{\partial p_t} \quad (28)$$

and:

$$\frac{\partial \tau_{ij}}{\partial \Pi} = a k_{ci}(\bar{T}_j) f \left[ \frac{1}{\Pi} \frac{\partial \Delta_j}{\partial \Pi} - \frac{\Delta_j}{\Pi^2} \right] \quad (29)$$

The formulae for  $\Delta$  and its derivatives are in Table 4-2.

The discrete formulation of the cloud radiative transfer makes  $\partial \tau / \partial p_t$  and  $\partial \tau / \partial \Pi$  discontinuous functions of  $p_t$  and  $\Pi$ . To make these derivatives smoother, they are computed as:

$$\frac{\partial \tau}{\partial p_t} = \frac{1}{5} \sum_{m=1}^5 \left. \frac{\partial \tau}{\partial p_t} \right|_m \quad (30)$$

and:

$$\frac{\partial \tau}{\partial \Pi} = \frac{1}{5} \sum_{m=1}^5 \left. \frac{\partial \tau}{\partial \Pi} \right|_m \quad (31)$$

where  $p_t|_m = p_t + (m-3)\delta$  and  $\delta$  is an increment of pressure equivalent to a height increment of about 500m.

The derivatives of  $R$  with respect to cloud parameters are:

$$\frac{\partial R_i}{\partial Q} = \sum_j \frac{\partial R_i}{\partial \tau_{ij}} \frac{\partial \tau_{ij}}{\partial Q} \sec \theta_{obs}, \quad (32)$$

$$\frac{\partial R_i}{\partial p_t} = \sum_j \frac{\partial R_i}{\partial \tau_{ij}} \frac{\partial \tau_{ij}}{\partial p_t} \sec \theta_{obs} \quad (33)$$

and:

$$\frac{\partial R_i}{\partial \Pi} = \sum_j \frac{\partial R_i}{\partial \tau_{ij}} \frac{\partial \tau_{ij}}{\partial \Pi} \sec \theta_{obs} \quad (34)$$

Table 4-2:  $\Delta$  and its Derivatives.

Condition on layer j	$\Delta_j$	$\frac{\partial \Delta_j}{\partial p_t}$	$\frac{\partial \Delta_j}{\partial \Pi}$
Outside cloud $p_{j+1} \leq p_t$ or $p_b \leq p_j$	0	0	0
Contains cloud top $p_j \leq p_t \leq p_{j+1} \leq p_b$	$p_{j+1} - p_t$	-1	0
Entirely within cloud $p_t \leq p_j \leq p_{j+1} \leq p_b$	$p_{j+1} - p_j$	0	0
Contains cloud base $p_t \leq p_j \leq p_b \leq p_{j+1}$	$p_b - p_j$	1	1
Contains entire cloud $p_j \leq p_t \leq p_b \leq p_{j+1}$	$\Pi$	0	1

#### 4.1.5. Scattering Model

This is a non-polarized radiative transfer code. This model computes the thermal radiation in a multi-layer cloud in the atmosphere. Three approximate solutions to the radiative transfer equation in scattering media are available: single scattering approximation, Eddington second approximation and a hybrid approximation combining single scattering and Eddington solutions. This model was developed by Deeter and Evans (1998). The inputs to this model are the cloud properties which are the ice water path (IWP) and the particle size distribution mean diameter (Dme) for each layer. The scattering properties are computed off-line and pre-stored in files. There may be different scattering tables for different types of clouds. The properties are calculated either by the Mie code assuming spherical shapes or by the DDA code for randomly oriented non-spherical particles.

#### 4.2. Inversion Approach

The Core Physical Inversion Module takes advantage of new features:

- A non-linear inversion method which improves the convergence of the original maximum likelihood method when the first guess is far away from solution by explicitly taking into account the impact of linearization noise at each iteration.
- The use of an EOF (Empirical Orthogonal Functions) representation for temperature and water vapor profiles and spectral emissivity which provides better stability and reduces computation time.

#### 4.2.1. General Inversion Methodology

The inversion methodology adopted for the core retrieval module is based on a classical constrained non-linear least square approach.

The solution to the inverse problem is found by minimizing a cost function of the form:

$$\phi(x) = \|y_0 - F(x)\|^2 + g(x) \quad (35)$$

where the first term is the error associated with the unconstrained solution, and the second term is the penalty function which constrains the solution.  $Y_o$  is a vector represent the observed radiances.  $F(x)$  is a vector which contains the calculated radiances using the OSS forward model.

Rodgers [1976] showed that the cost function, for a maximum likelihood solution is:

$$\phi(x) = [y_0 - F(x)]^T S_y^{-1} [y_0 - F(x)] + (x - x_a)^T S_x^{-1} (x - x_a) \quad (36)$$

Here,  $S_y$  is an error covariance matrix that describes the instrument and forward modeling errors.  $x_a$  and  $S_x$  are the background vector (prior) and the associated error covariance matrix, respectively.

The iterative solution can be written in Rodgers well-known form by minimizing the cost function and using the Gauss-Newton method (neglecting the term associated with second derivative of  $F(x)$ ):

$$x_{i+1} = x_a + (K_i^T S_y^{-1} K_i + S_x^{-1})^{-1} K_i^T S_y^{-1} [y_o - y_i - K_i (x_a - x_i)] \quad (37)$$

where  $y_i$  is the current value of  $F(x)$  linearized about a reference state  $x_a$  and  $K$  is a matrix containing the current partial derivatives of  $y_i$  with respect to  $x$ .

The need for a constraint relates to the fact that the inversion problem is generally ill-conditioned, e.g. the existence of null-space of the observing system leads to a non-uniqueness of solution. The use of *a priori* information, when available, is a way to ensure that the derived solution is physically acceptable. This information may be used to stabilize the solution and control the step size. The background covariance constraint introduces inter-level correlation in the temperature and moisture profiles, which prevents the solution from being unstable. There are some concerns that if the constraint is biased, it will introduce errors into the solution. To ensure a successful retrieval of the state parameters, the covariance must be derived from a large ensemble of independent measurements that describe large variability in the state parameters. For atmospheric temperature and moisture profiles,  $S_a$  are derived from global radiosonde and rocketsonde measurements that meet the variability requirement.

#### 4.2.2. Pseudo Linearization Noise

One major shortcoming of the standard Gauss-Newton procedure is that it does not provide a mechanism to account for errors due to linearization. Ignoring this error term degrades the rate of convergence when the problem is highly non-linear or when the first-guess is far away from the solution.

It is implied that the “best” solution is one that fits the observation within the model noise, i.e., it ignores the fact that the linear model cannot fit the observation better than:

$$\varepsilon_{NL}(x) = F(x) - F(x_0) - K(x - x_0) \quad (38)$$

There are two consequences of failing to take  $\varepsilon_{NL}(x)$  into account:

- For univariate problems there is a risk of overshooting, which may slow down convergence rate.
- For multivariate optimization problems, where conditioning is marginal, it destabilizes the solution by giving too much weight to the unconstrained solution. That is, it over fits the radiances and introduces spurious structure in the solution vector due to amplification of non-linear noise (e.g., for cloud parameters spurious structure moves the result further away from the actual solution and convergence may never be reached).

An acceptable solution for a certain class of multivariate optimization problems (such as atmospheric profiling) is to reduce the dimension of the state vector at the beginning of the



iterative process and increase it progressively as the solution gets closer to the truth. This avoids the problem of noise amplification. Such a method has been successfully applied for ozone profiling [Snell, 1999]. However, this procedure is not applicable for loosely correlated parameters such as cloud optical depth and cloud top altitude. For such problems, ill-conditioning can be avoided by estimating the pseudo-linearization error from the radiance residuals.

An empirical method was devised based on extensive retrieval simulations. This method attempts to use information about the problem (e.g. the degree of non-linearity) in combination with the radiance residual, which is used as a measure of the distance from the truth, to provide an estimate of the nonlinearity error. In this approach, the diagonal covariance matrix of the measurement/modeling errors ( $S_y$  in Eq. 37) is replaced by a matrix with diagonals set to either some fraction of the error in the observed space, i.e., the difference between  $y_i$  and the observed radiance ( $y_o$ ), or to the noise variance:

$$S'_y(j, j) = \max \left\{ \frac{1}{\alpha} [y_i(j) - y_o(j)]^2, S_y(j, j) \right\} \quad (39)$$

where  $\alpha$  is the error control parameter and  $S_y(j, j) = \sigma^2(j)$  is the instrument noise variance for the  $j^{\text{th}}$  channel. This is done for each iteration of the retrieval, and the role of  $\alpha$  is to limit the  $\delta x$  at each iteration step. Typical values of  $\alpha$  range between 4 (for highly non-linear problems encountered in atmospheric remote sensing) and 100 for temperature inversion problems (tends toward ML result). The parameter alpha is relatively insensitive to initial guess. The most noticeable increase in performance is when the initial guess for each algorithm was constructed based on climatology information. It is well known that cloud parameters change the radiative transfer equation in a highly non-linear way. (See also [EN #10](#) response.)

It has been demonstrated that the method is capable of simultaneously solving for cloud parameters and atmospheric/surface parameters. This is an important consideration in selecting an appropriate inversion technique for an operational algorithm.

#### 4.2.3. Eigenvector Transformation of Retrieved Parameters

Several regularization methods that aim at reducing the dimensionality of the problem and therefore stabilizing the solution are proposed in the literature (e.g., Pseudo Inverse, and Singular Value Decomposition). In the current algorithm, regularization is achieved by projecting the solution vector onto a set of pre-computed Empirical Orthogonal Functions (EOFs) derived from

a large ensemble of temperature and moisture profiles representative of global climatology. The EOFs are obtained by applying a principal component analysis (PCA) to an error covariance matrix ( $S_x$ ) derived from the NOAA-88 database (see detailed description in Appendix 1). The use of EOF representations for the temperature and water vapor profiles and the spectral emissivity provides better retrieval stability by eliminating the EOFs with small eigenvalues. This also serves to reduce the required computation time. The iterative equation is not changed by the EOF transformation.

By retrieving the coefficients which project the temperature and moisture profiles onto the selected EOFs, PCA provides a reduction in the dimension of the state vectors to be retrieved. The number of EOFs retained for the retrieval is dependent on the noise and spectral resolution of the sensor. Trade studies for the CMIS instrument show that the temperature profiles may be represented by the first 20 EOFs derived from the temperature covariance matrix, and moisture profiles by 10 EOFs derived from the moisture covariance matrix. In our previous retrievals, the background covariance matrix was somewhat ill-conditioned for the upper level moisture profiles due to the lack of real measurements above 300 mb. The current approach avoids this potential problem.

Before the inversion,  $\Delta x = x_{i+1} - x_a$  and  $K_i$  are transformed into the EOFs domain according to the following equations:

$$\Delta \tilde{x} = U^T \Delta x \quad (40)$$

and:

$$\tilde{K}_i = K_i U \quad (41)$$

where  $U$  is a matrix which contains only the selected significant EOFs. The diagonalization of  $S_x$  is given by:

$$\Lambda = U S_x U^T \quad (42)$$

The transformed retrieval equation may now be written as:

$$\Delta \tilde{x}_{i+1} = \Lambda \tilde{K}_i^T (\tilde{K}_i \Lambda \tilde{K}_i^T + S_y)^{-1} (y_0 - y_i + \tilde{K}_i \Delta \tilde{x}_i) \quad (43)$$

#### 4.2.4. Retrieved Parameters

The retrieved parameters are listed in Table 4-3. In the current algorithm, the surface pressure is obtained from numerical weather prediction (NWP) model output combined with knowledge of

local topography (see also Appendix 2). In the absence of NWP data the algorithm will default to climatological values for the surface pressure. (See also [EN #49,97](#) responses.)

Uncertainties in surface pressure produced by current NWP models vary seasonally and are estimated at 2.5 mb globally (e.g., Devenyi and Schlatter 1994, Goerss and Phoebus 1993). These uncertainties are derived through a regular intercomparison of the deterministic forecast produced by seven different reference models (ECMWF, 2000). These uncertainties do not include errors in the interpolation performed as part of the pre-processing required for input into the CMIS algorithm. The errors can be much larger locally in instances of rapid cyclogenesis. For example, comparisons between mesoscale models and actual measurements performed in the context of North Atlantic Storm Experiment indicated errors as large as 13 mb.

Table 4-3: List of Retrieved Parameters (EOF Domain).

Parameters	Representation
Atmospheric Temperature	20 eigenvectors (full channel set) - number depends on noise (i.e. resolution) and channel selection
Water vapor	10 eigenvectors (full channel set) – algorithm also handles layer representation
$\Delta T_{\text{skin}}$	Difference between skin surface temperature and surface air (shelter) temperature
Surface Emissivity	12 eigenvectors (full channel set)
Water clouds	CLW and cloud top pressure - Sensitivity to thickness when external constraint on cloud top pressure (from e.g. VIIRS) is available
Ice clouds	Requires treatment of scattering (enhancement) IWP, mode radius, cloud top pressure

The temperature and water vapor profiles are retrieved as the projection coefficients of the pre-determined EOFs. Trade studies for the CMIS instrument show that to adequately represent the atmospheric variability and stabilize inversion algorithm, the temperature profiles should be represented by 20 EOFs, while the moisture profiles require only 10 EOFs. The determination of the appropriate number of eigenvectors is discussed in Volume 3, Part 1 of the ATBD (“Atmospheric Vertical Moisture Profile EDR”).

The retrieval algorithm provides a mechanism for taking into account uncertainties in the modeled emissivity by retrieving the surface emissivity in the EOF representation. This allows the algorithm to compensate for spectral variability that would not be captured if only the model coefficients were retrieved. Some uncertainties that may cause a mismatch between the model

and the measurement include specification of the dielectric constant for saline water and uneven foam coverage or variable wind speed within the field-of-view. Currently, 12 EOFs are used to fully capture the correlation between different channels. For ocean scenes the Wilheit model [Wilheit, 1979; Kohn and Wilheit, 1995] is used to specify the surface emissivity, while for land cases the algorithm uses data from Prigent [Prigent *et al.*, 1997]. These databases are described in more detail in Appendix 3, and both the ocean and land emissivity specification will be refined in the next phase of the project. This will be done using a technique similar to that of Prigent, who derived the land emissivity using a combination of SSM/I and TOVS data. In order to have a database available for the operational algorithm upon launch of CMIS, the new analysis will be conducted first using sensor data available prior to launch, such as from SSMIS and/or AMSR. But, after the launch of CMIS, an improvement to the land emissivity database will be derived using data from CrIS and VIIRS. This has the advantage of using data from co-located sensors and will allow for an improved specification of the water vapor and correction for the IR surface emissivity and clouds.

The retrieval of the surface skin temperature and the surface air temperature relies on the natural correlation between these quantities. However, variations in the surface terrain height can result in variations in the surface pressure, which complicates the algorithm implementation. In order to avoid the complexity of having to modify the background error covariance to accommodate variations in surface terrain height, the algorithm is set to retrieve  $T_{sfc}$  and  $\Delta T = T_{skin} - T_{sfc}$  instead of  $T_{sfc}$  and  $T_{skin}$ . In this scheme the surface air temperature also drives the surface skin temperature and the correction term  $\Delta T$  represents the departure of actual surface skin temperature from  $T_{sfc}$ . It should be noted that the retrieval itself is unaffected by this change of variables. However, because  $\Delta T$  is statistically uncorrelated with  $T_{sfc}$ , the background profile and background error covariance matrix remain independent of terrain height.

The measured brightness temperatures are sensitive to the effective emission of the cloud and include contributions from both liquid water and ice. The details about the method of computing the radiative transfer are given in Section 4.1.4.3: Microwave Cloud Liquid Water and Section 4.1.5: Scattering Model.

Liquid water clouds are modeled by assuming a fixed thickness and uniform vertical distribution of droplets within the cloud, and the radiative transfer is treated by assuming Rayleigh

absorption for cloud droplets. This assumption ignores the scattering effects of the water droplets, which are of only secondary importance to the overall radiative transfer. While the algorithm is further simplified by assuming a plane-parallel cloud layer, this poses some problems with the high incidence angles associated with CMIS. Future versions of the algorithm will address this by treating the cloud as two effective cloud layers, one for the downwelling path and one for the upwelling path. It is assumed that the impact of the vertical and horizontal distribution of clouds is negligible. This assumption may not hold for clouds with a high density of water droplets near the cloud top, and tests will be conducted to fully validate this assumption and, if necessary, develop a different scheme.

Two liquid water cloud parameters are retrieved, the total liquid water and either the cloud top pressure or the effective cloud thickness. If cloud top altitude information is available from VIIRS, the CMIS algorithm will retrieve the effective cloud thickness. However, the CMIS algorithm will retrieve the cloud top in the absence of VIIRS information. This scheme is necessary because the algorithm must allow for multiple degrees of freedom in order to fit the observed radiances.

For ice clouds, the default mode for the radiative transfer is to include the particles without scattering. This is done to provide a faster algorithm. The current algorithm does have the capability of including the treatment of scattering for the high frequency channels, since scattering is required for the ice water path (IWP) EDR and provides a correction for the water vapor sounding channels from ice effects. Three parameters are used to model the ice clouds: IWP, median particle diameter, and the cloud top pressure. The cloud top pressure can be obtained either as an external EDR from VIIRS, or from a CMIS retrieval.

#### **4.2.4.1 Background Selection**

While the algorithm assumes background errors have a Gaussian distribution, the errors are not perfectly Gaussian, particularly when a global climatology is used. Non-linear statistical methods (e.g. classification/discrimination) have the ability to capture climatological correlations between atmospheric parameters. The result is a better than average performance wherever null-space dominates the retrieval error (i.e., the radiometric information is insufficient to resolve the vertical structure). The Core Module can be improved by pre-classifying by air mass or region (applies only at 50 km resolution), as described in Appendix 5.

The selection of the appropriate surface emissivity background follows the flow diagram shown in Figure 4-4, and depends on whether or not the climatology operating mode has been chosen. The first test with the climatology mode is whether or not the scene is considered to be “land”, based on the land-mask classification. Land pixels always use the “land” covariance. If the pixel is not considered to be “land”, a test is done to see whether or not sea-ice is detected. If no ice is present then the “ocean” covariance is used.

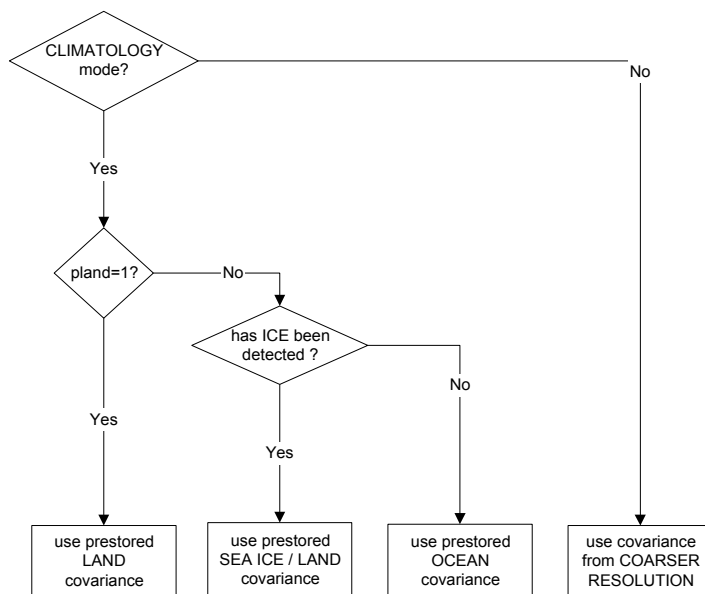


Figure 4-4: Flow Diagram Illustrating the Background Selection for the Surface.

There are two different methods for determining the “land” covariance. For regions of rapidly changing surface type the most robust is a background/covariance derived from the Prigent database. This database is described in more detail in Section . We will also maintain a dynamic database of day-to-day geo-located surface emissivity values derived from the CMIS retrievals. This data will be used to select the background and covariance for regions where the temporal change in emissivity is small.

#### 4.3. Physical Constraints on Retrieval Solution and Quality Control of Retrieved Parameters

Identifying the quality of the retrieved atmospheric and surface parameters will be paramount for integrating this data into numerical models. We have identified a set of quality control criteria that will estimate the accuracy, and hence the usability, of the retrievals. This approach relies on both physical constraints, i.e., ensuring that the solution meets geophysically acceptable values, and numerical convergence criteria.

The first set of quality control checks involves the geophysical evaluation of the retrieved parameters. This occurs between retrieval iterations. Such tests include checking the surface emissivity to be sure it is between 0 and 1, checking to be certain the values of cloud liquid water (CLW) are positive, and checking the cloud top and base altitudes to be sure that they are at least 20 mb above the surface. If the retrieved solution fails any of these tests, appropriate action is taken to push the retrieval back in the proper direction. For example, negative values of CLW are reset to zero and the covariance matrix is tightened.

In addition to tests during the retrieval process, a post-retrieval test of the water vapor profile is performed to see if super-saturation occurs. The current algorithm will flag cases which have a relative humidity above 110% at any given level. However, a more robust check is currently under evaluation whereby the vertical structure of the relative humidity profile is assessed for super-saturation. This additional complexity is better suited for partly cloudy scenes.

The baseline algorithm uses the chi-square test  $\chi_n^2$  as a measure of numerical convergence:

$$\chi_n^2 = \frac{1}{N_c} \sum_{i=1}^{N_c} \frac{(R_i - R_i^*)^2}{\sigma_i^2} \quad (44)$$

where  $N_c$  is the number of CMIS channels used in the retrieval,  $R_i$  is the observed radiance in channel  $i$ ,  $R_i^*$  is the simulated radiance in channel  $i$  using the forward model, and  $\sigma_i$  is the error standard deviation associated with  $R_i$ . A good convergence gives  $\chi_n^2 \leq 1$ .

The chi-square convergence criterion is also useful for detecting radio-frequency interference (RFI). A test at the SDR processing level will screen for RFI, and for cases above a threshold the retrieval will not be performed. However, the chi-square retrieval convergence criterion provides an additional check on the intra-channel consistency of the measurement. The ability to compute this metric is another advantage of a physical-based retrieval algorithm over a regression algorithm. Retrievals which do not pass the chi-square convergence criterion will be flagged for further investigation into the cause of the problem. (See also [EN #88](#) response.)

The highest quality solution is obtained when the retrieval solution satisfies all of the physical criteria and the  $\chi^2$  is less than 1.

## 5. Core Physical Inversion Module Performance Analysis

This section provides an overview of the overall system performance for the core module output parameters (i.e., temperature and moisture profiles along sensor view path, surface skin temperature and emissivity, cloud liquid water and total integrated water vapor). In the current CMIS EDR scheme, the final EDRs are obtained by post-processing of the core module output. Therefore the performance characteristics of the core module are driving the final EDR performances.

### 5.1. Test Data Sets

The core algorithm has been tested using both simulated data and real measurements from available spaceborne microwave sensors (SSM/I, TMI, and AMSU).

In simulations, atmospheric temperature and water vapor, as well as surface temperature datasets are obtained from the NOAA-88 data set.

The NOAA-88 dataset contains 8344 profiles derived from radiosonde observations (RAOBs) taken in 1988. Temperature and moisture profiles from the surface to 1 mb were based on radiosonde reports. Temperature profiles were extrapolated using information from rocketsondes having similar stratospheric temperature in the overlap pressure regime, and moisture was extrapolated based on climatology. More details about the NOAA-88 database and the remapping of the NOAA-88 water vapor profiles are given in Appendix 1 of the Core Module ATBD.

The water clouds are simulated assuming a uniform distribution of cloud liquid water between the specified cloud base and cloud top. In non-precipitating conditions, cloud liquid water is varied between 0 and 0.5 mm. To avoid unrealistic conditions, the 0.5 mm limit is reduced for very dry atmospheres. Cloud top is varied randomly between the freezing level (253 K, profile dependent) and 50 mb above the surface, and unless specified otherwise, cloud base varies randomly between the cloud top and the surface, with a minimum thickness of 50 mb.

Ice clouds are specified in terms of particle size and mass density of the cloud particles. The following assumptions have been made for the Cloud Ice Water Path (CIWP) simulations:

- The cirrus distribution variance follows a gamma law with  $\alpha=2$ .



- The ice particles are considered to be spherical (no ice shape effect).
- The  $D_{me}$  (particle median diameter) varies from 50 to 1000  $\mu\text{m}$ .
- The Ice Water Path (IWP) varies from 0 to 1000  $\text{g}/\text{m}^2$ .
- The cloud thickness is fixed at 50 mb.
- The tropopause is at freezing level.

Over ocean, Wilheit's surface emissivity model [Wilheit, 1979; Kohn and Wilheit, 1995] is used to specify the emissivities at all CMIS frequencies for given wind speed and sea surface temperature. The model for the dielectric constant of seawater is that Klein and Swift [Klein and Swift, 1977] with fixed salinity.

Over land, the emissivity data used in the present study is derived from global map of monthly mean SSM/I land emissivities derived by Prigent *et al.* [Prigent *et al.*, 1997], based on co-located SSM/I and TOVS measurements (see Appendix 3 for more details and discussion on the inter/extrapolation of surface emissivities to CMIS frequencies.) (See also [EN #83](#) response.)

Two types of data sets are used in the development and performance evaluation of the core physical retrieval algorithm. (See also [EN #11](#) response.)

*-The first data set (randomized data set)* consists of 1000 atmospheric profiles (with corresponding surface temperatures) selected at random from the NOAA-88 data set described above. For each profile, CLW, cloud top height and wind speed are randomly assigned. For wind speed a uniform distribution between 0 and 20 m/s is assumed. No correlation is assumed between cloud and surface parameters and the rest of the parameters. In order to account for situations for which the field-of-view is only partially filled, the atmospheres are not saturated within clouds.

*- The second data set (stratified data set)* is used for algorithm tuning and to test the robustness of the algorithm. The data set consists of only three temperature profiles chosen to encompass the range of conditions encountered globally. For each temperature profile, water vapor (from original data set) is scaled so that total integrated water vapor assumes standard values between the driest and moistest observations for each temperature profile. The seven standard values used are (1mm, 5mm, 20mm, 30mm, 40mm, 50mm and 60mm). For each profile, TOA radiances are computed for 7 values of  $T_{\text{skin-Tair}}$  ( $\pm 10$ ,  $\pm 5$ ,  $\pm 2.5$ , 0), 3 values of cloud top (800, 650, 500 mb) and 5 values of

CLW (0, 0.05, 0.1, 0.25, 0.5 mm). Cloud thickness is held fixed at 100 mb. The whole data set is run each time for different selected land/ocean emissivities. Sensitivity to noise is obtained by performing the retrieval for 50 different realizations of the random radiometric noise. This test set is particularly stressful and is used to evaluate the behavior of the algorithm over the whole range of possible conditions and to make sure that it can handle the most extreme situations.

## 5.2. Emissivity Retrieval Results

As discussed above, the surface emissivity is retrieved by the Core Module as part of the geophysical vector. (See also [EN #83](#) response.) To demonstrate the feasibility of the microwave retrieval over land, real Special Sensor Microwave Imager (SSM/I) data was used as input to the Core Module.

Over land, *a priori* information is needed to constrain the retrieved surface emissivity. To accomplish this, an emissivity covariance matrix was generated based on the emissivity database described by Prigent [Prigent, *et. al.*, 1997]. This database was developed from co-located IR, SSM/I measurements and numerical weather prediction analyses over Africa and Europe. Before proceeding with the retrieval, the SSM/I brightness temperature measurements were interpolated to the 19 GHz footprint using the method described in Appendix 3.

The land emissivity retrieval was tested over North America using data for the one-week period from 1 October to 6 October 1995. The emissivity was retrieved at the SSM/I frequencies of 19.35, 37.0, and 85.5 GHz for both vertical (Vpol) and horizontal (Hpol) polarization and for the 22.235 GHz at the vertical polarization. The retrieval results presented in Figure 5-3 show that the 19 GHz Vpol emissivity is stable during the entire one-week period, except for October 3rd. All frequencies and polarization show the same pattern of retrieval statistics.

On October 3<sup>rd</sup>, a significant decrease in retrieved surface emissivity is observed in some areas, particularly in Texas, and for some locations the data is “missing” because the retrieval did not converge. This is observed in all of the channels. An examination of the ground-based weather radar reflectivities for the period approximately one hour before the satellite overpass (also shown in Figure 5-3) indicates that a heavy rain was falling in these regions. For the case of “missing” data, the rain was sufficient to keep the retrieval from converging. In the other regions, the heavy rain likely produced large areas of surface water, or very wet soil. Since

water has a much lower microwave emissivity than land, this scenario is consistent with the lower land-surface-emissivity retrievals produced by the core module.

The retrieved emissivity is also qualitatively consistent with the global emissivity maps provided by Prigent (personal communication, 1999) which include North America. Further, we are able to obtain a coherent emissivity retrieval with the Core Module even if the covariance matrices are established with data taken from Africa. Figure 5-1 compares the Prigent data and the Core Module Retrieval for the 19 GHz Hpol emissivity (high geographical variability in this channel), while Figure 5-2 shows the same emissivity retrievals at 19 GHz Vpol (more stability with geographic features in this channel).

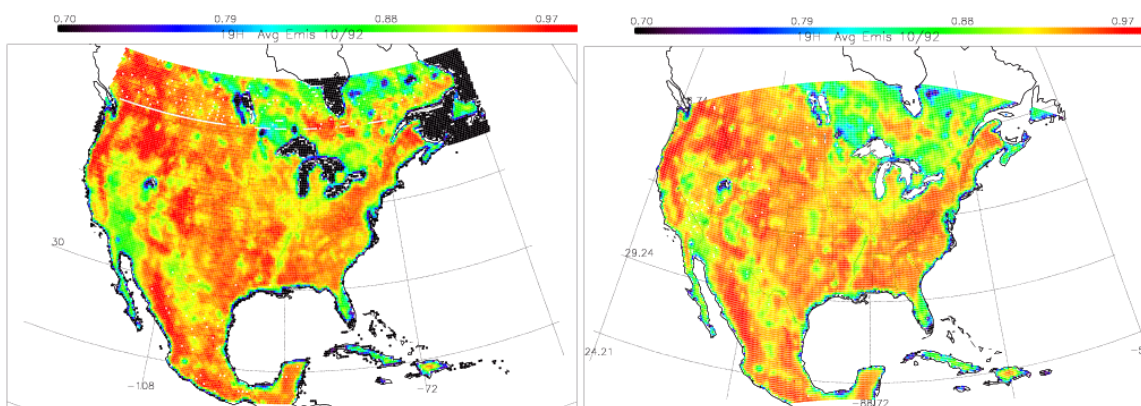


Figure 5-1: 19 GHz Hpol - Monthly Average - October 1992

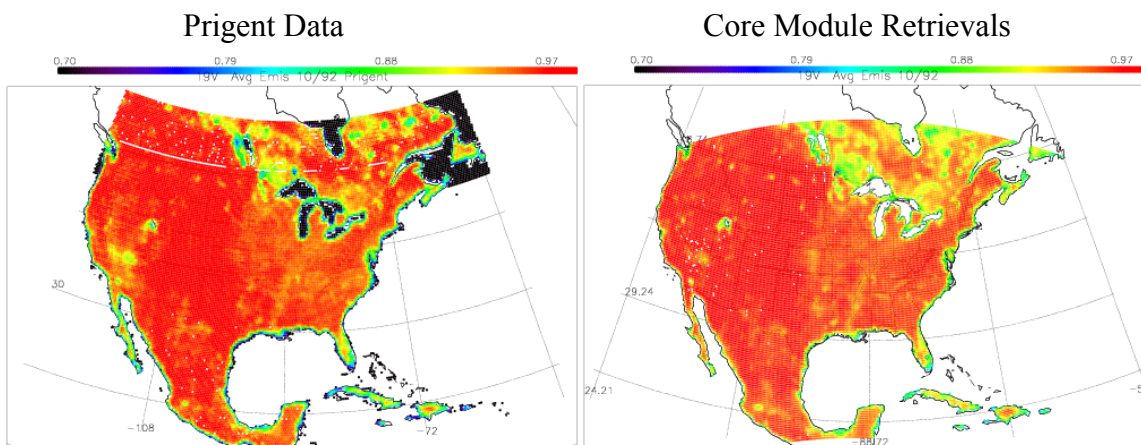


Figure 5-2: 19 GHz Vpol - Monthly Average - October 1992

# CORE PHYSICAL INVERSION MODULE PERFORMANCE ANALYSIS

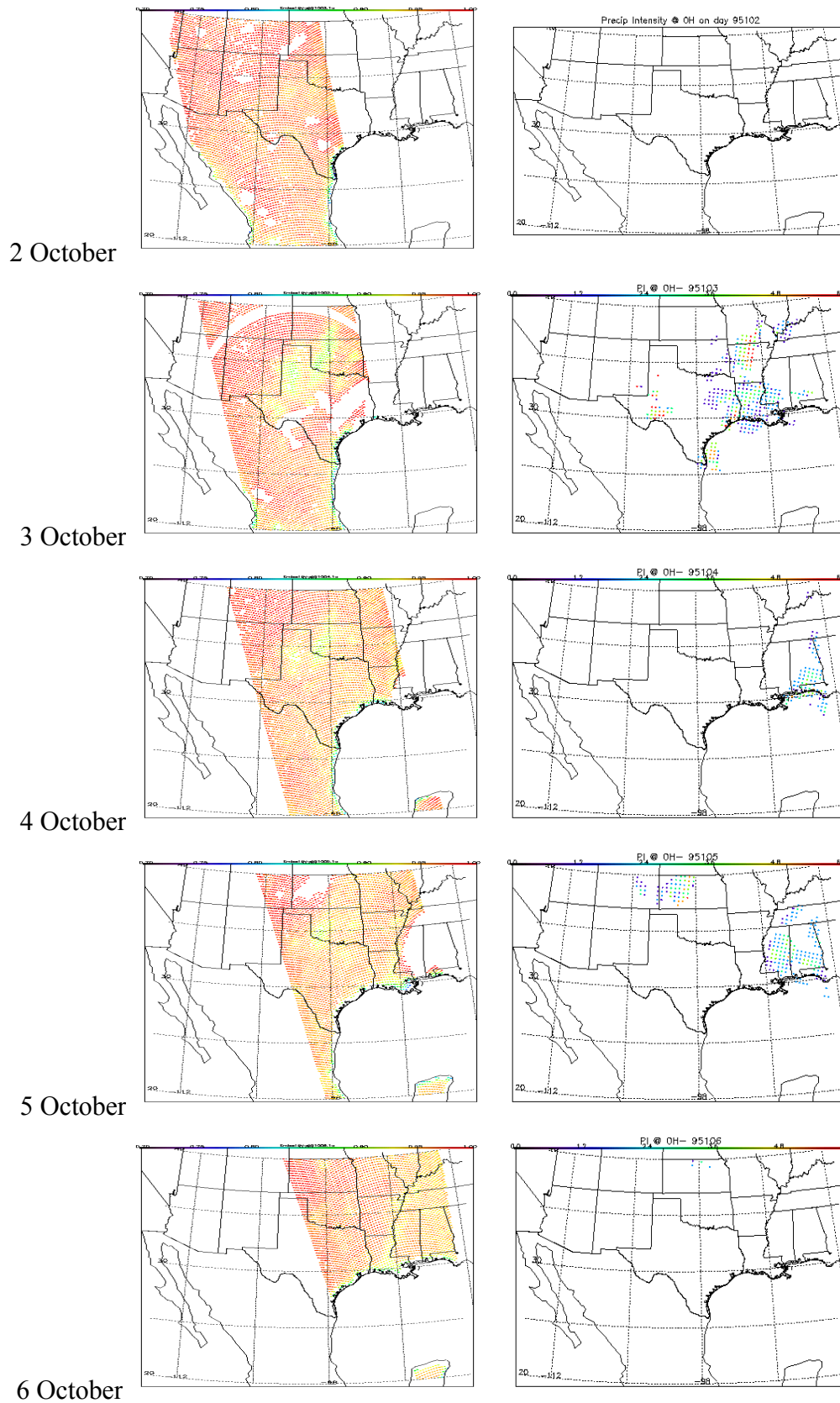


Figure 5-3: Core module retrieval from SSM/I data and precipitation index from ground-based radar.

It should be noted that the *a priori* land and ocean databases will be updated during Phase 2 using SSMIS data. They will be updated again after the launch of the first CMIS unit. The techniques developed by Prigent will be used over land and over ice to construct this database, though there will be many refinements after launch of CMIS due to the co-location with CrIS (high accuracy moisture/temperature sounding) and VIIRS (LST and cloud screening) data. Also note that Prigent's approach avoids physical surface emissivity model limitations. For example, many existing physical models do not fit many naturally observed spectra, are not valid over the full range of CMIS, and have difficulty reproducing global/seasonal variability without arbitrary assumptions regarding the composition and physical characteristics (e.g. topography, roughness, and vegetation cover) of nature surfaces or mixed surface types at the CMIS resolution.

### 5.3. Performance Stratification and Algorithm Robustness

An extensive set of retrieval tests were conducted to evaluate the core module performance over a broad spectrum of stratified environmental conditions. The purpose was to evaluate algorithm robustness for application to environments that may be unusual but important to CMIS users.

Table 2-1 describes lists the conditions over which performance was stratified. DeltaTskin refers to the difference between the surface skin temperature and the air temperature at the surface. Precipitable water was varied by taking the base mixing ratio profile and scaling it to achieve the target integrated value. There were three base profiles about which we varied other parameters. For each variation, made 20 different noise realizations. The number of simulated conditions becomes 3600 ( $5 \text{ deltaTskin} \times 3 \text{ TPW} \times 3 \text{ CLW} \times 2 \text{ Cloud Top} \times 2 \text{ surface types} \times 20 \text{ realizations}$ ) for each of the base profiles.

Table 5-1: Stratification parameters

	#1	#2	#3	#4	#5
Profile	Midlatitude summer	Tropical	Polar Winter		
DeltaTskin (K)	-10.	-5	0.	5.	10.
Precipitable Water ( $\text{kg/m}^2$ )	10.	30.	50.		
Cloud Liquid Water ( $\text{kg/m}^2$ )	0.	0.25	0.5		
Cloud Top (mb)	500.	700.			
Surface type	Ocean (wind speed 7 m/s)	Land (mean mixed forest)			

Examples of stratified performance results for the ocean surface are in Figure 5-4, Figure 5-5, Figure 5-6, and Figure 5-7, for temperature profile, water vapor profile, precipitable water, and cloud liquid water, respectively. Regression results are included on each plot for reference. The robustness of the core physical inversion is clear from the stability of the performance across the stratification categories.

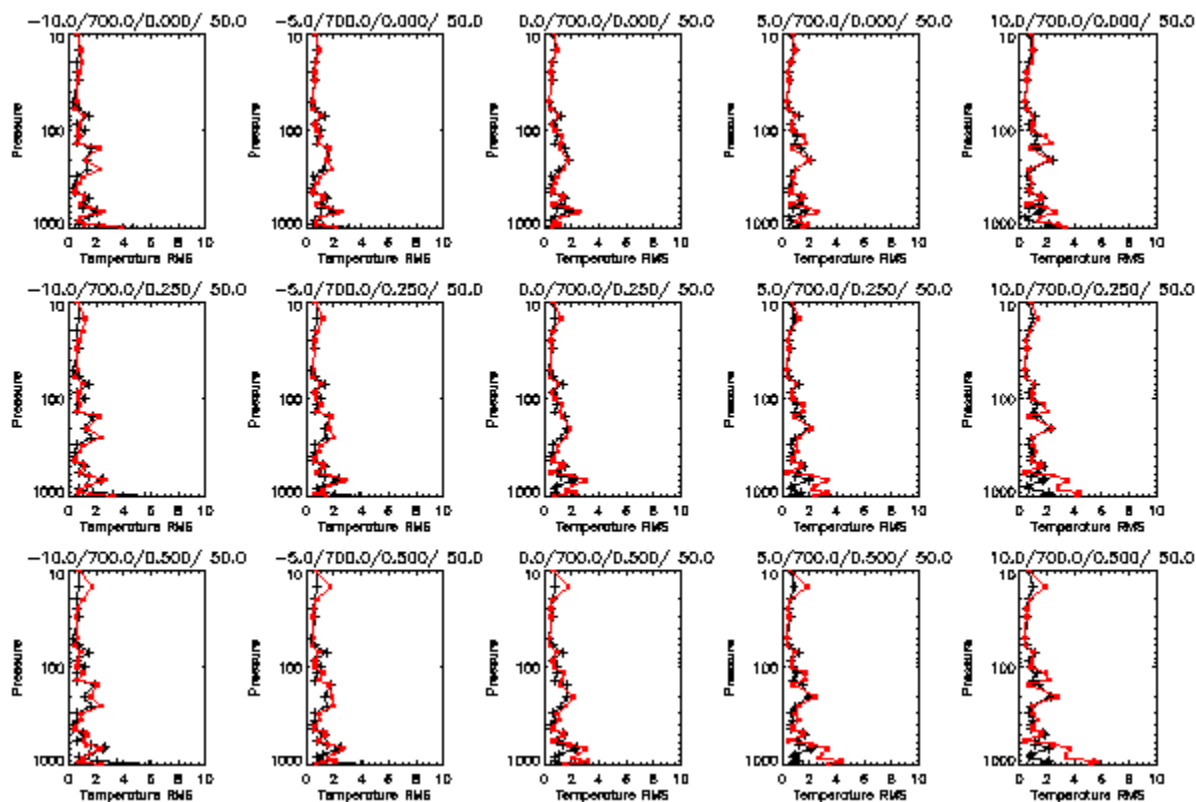


Figure 5-4: Temperature profile (not vertically averaged) rms error for ocean surface, midlatitude summer atmosphere, 50  $\text{kg/m}^2$  precipitable water, 700 mb cloud top, DeltaTskin varying from -10 to 10 K (left to right) and cloud liquid water varying from 0 to 0.5  $\text{kg/m}^2$  (top to bottom). The black curves are for the core physical algorithm and the red curves are for regression.

# CORE PHYSICAL INVERSION MODULE PERFORMANCE ANALYSIS

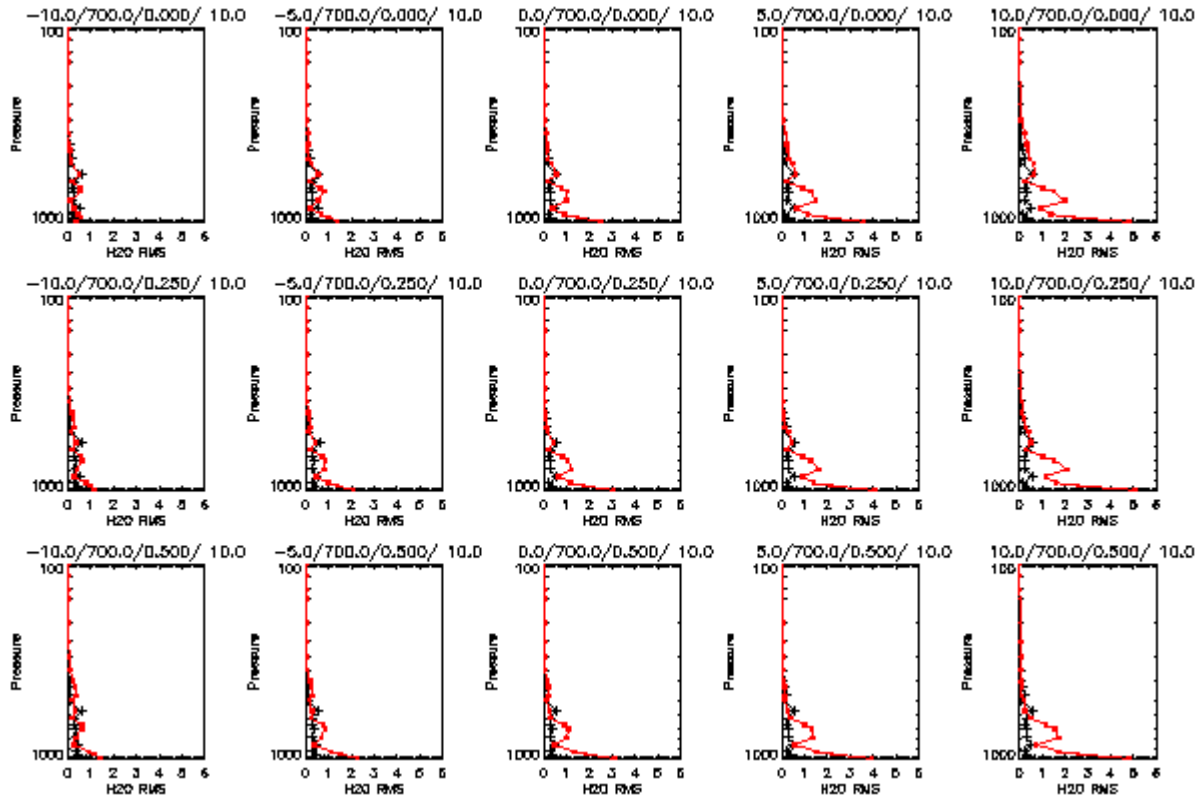


Figure 5-5: As in Figure 5-4, but for water vapor mixing ratio, and 10 kg/m<sup>2</sup> precipitable water.

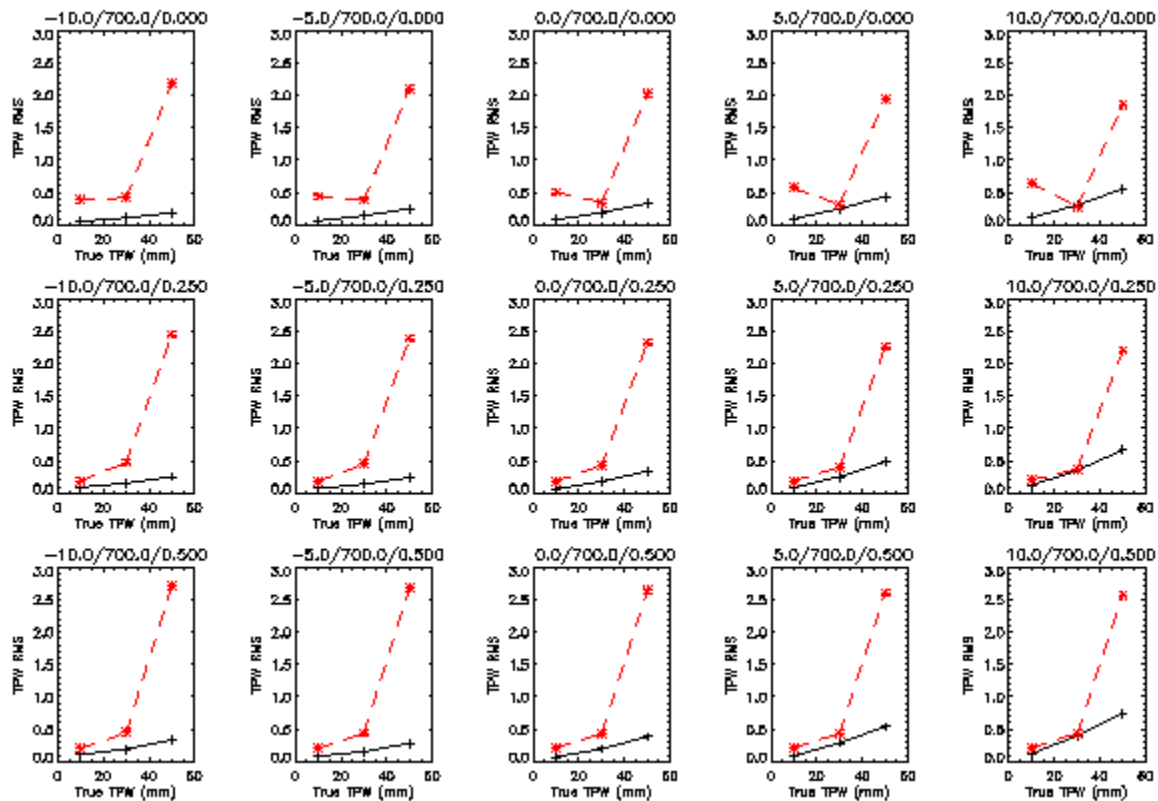


Figure 5-6: As in Figure 5-4, but for precipitable water, plotted versus precipitable water.



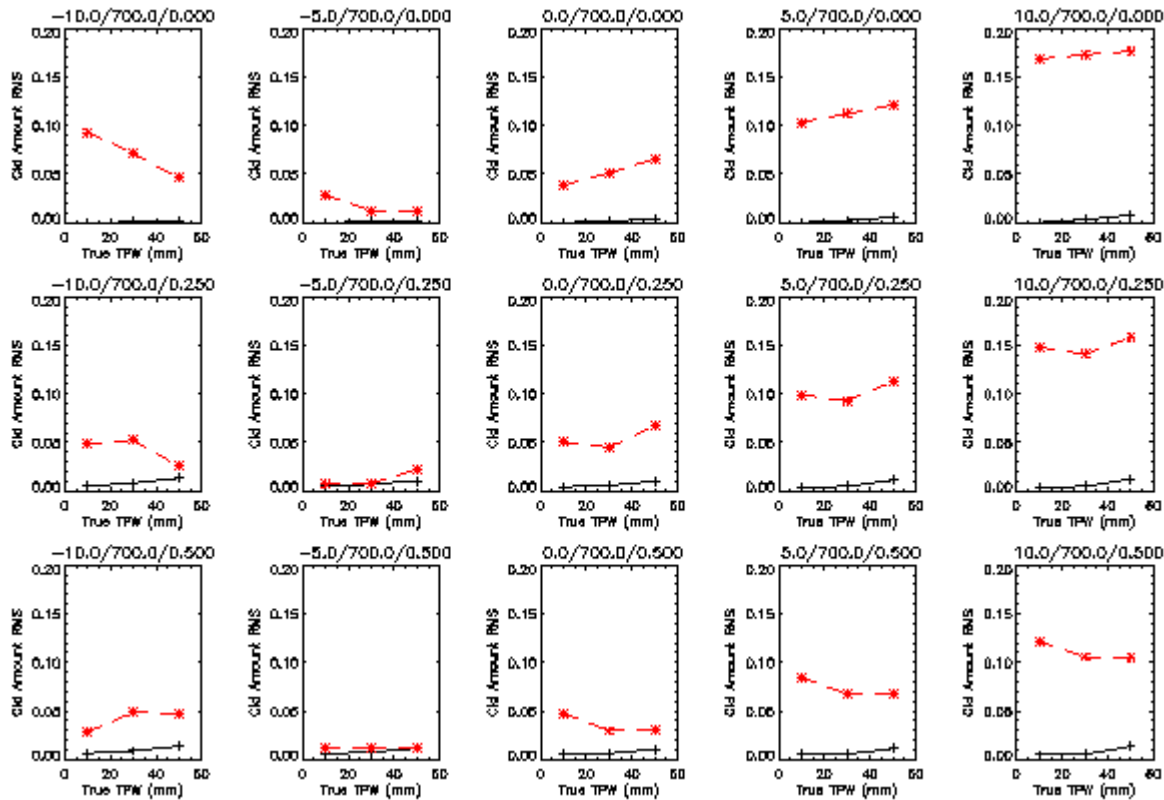


Figure 5-7: As in Figure 5-4, but for cloud liquid water, plotted versus precipitable water.

Additional stratification evaluations were made for individual EDRs derived from the core module, and are presented in the respective ATBDs.

#### 5.4. Graceful Degradation

It is inherent in the physical inversion methodology (sec. 4.2.1) that the core module degrades gracefully when channels are lost. If a channel is missing (turned off), the algorithm avoids executing radiative transfer computations for that channel and avoids loading that channel into the inversion operation. The basic retrieval function is unaffected. Examples are shown for exclusions of the indicated bands for land surface temperature (Figure 5-8), precipitable water over ocean (Figure 5-9), and cloud liquid water over ocean (Figure 5-10), for 50-km composite field of view sizes.



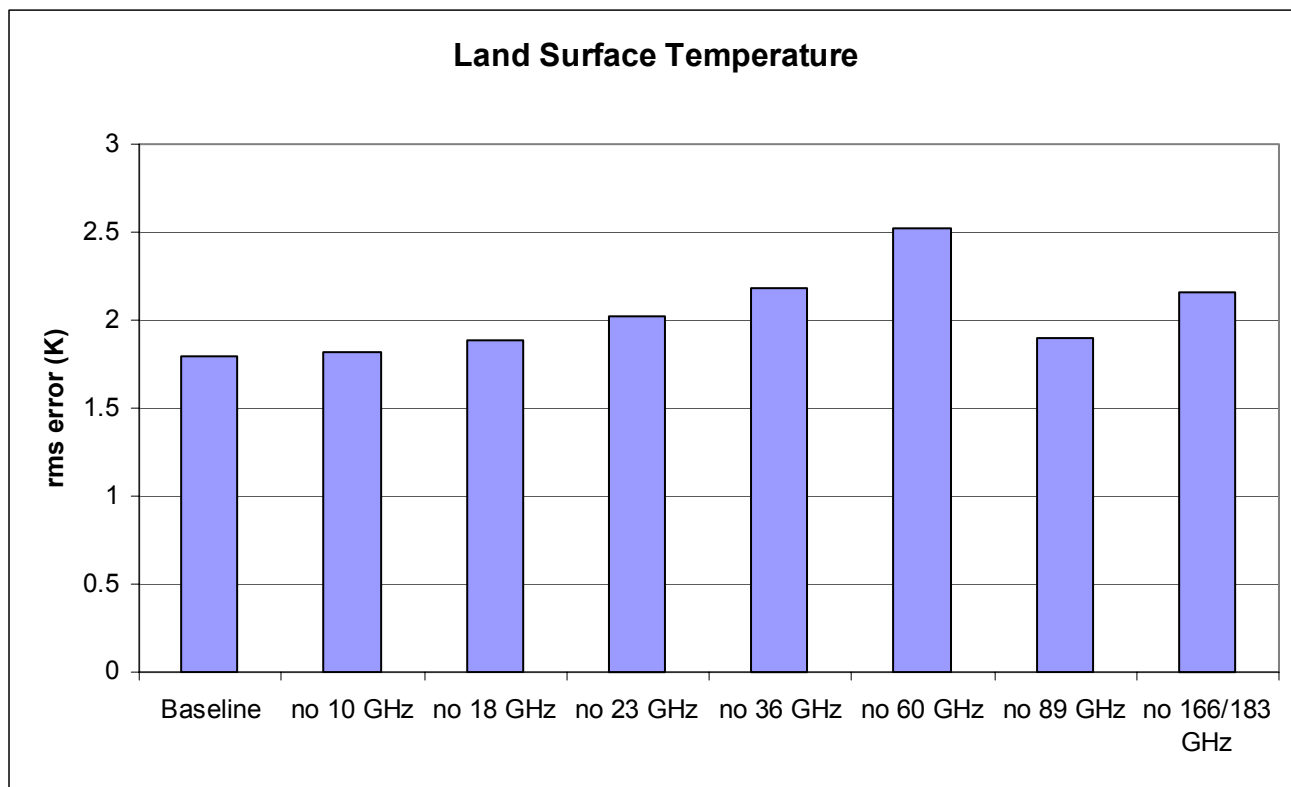


Figure 5-8: Impact of loss of the indicated bands on land surface temperature retrieval error.

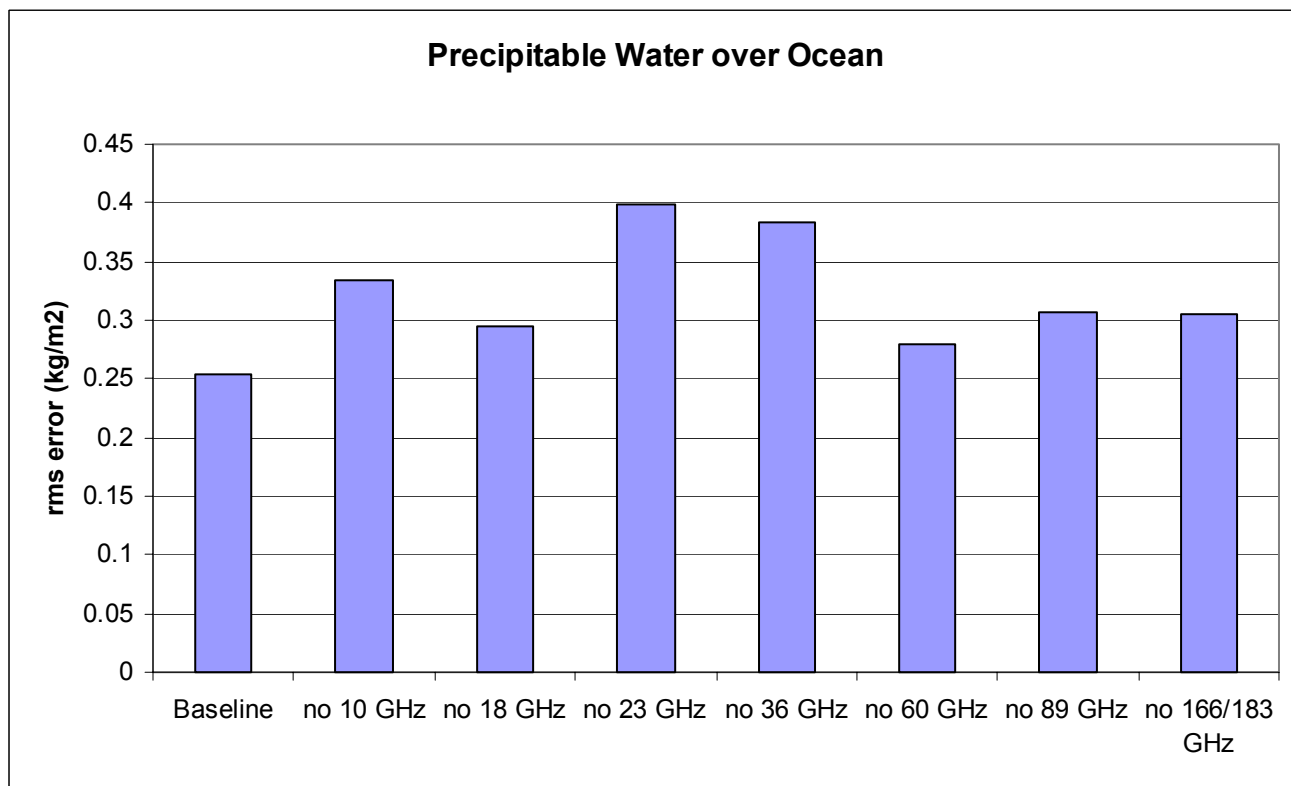


Figure 5-9: Impact of loss of the indicated bands on precipitable water retrieval error.

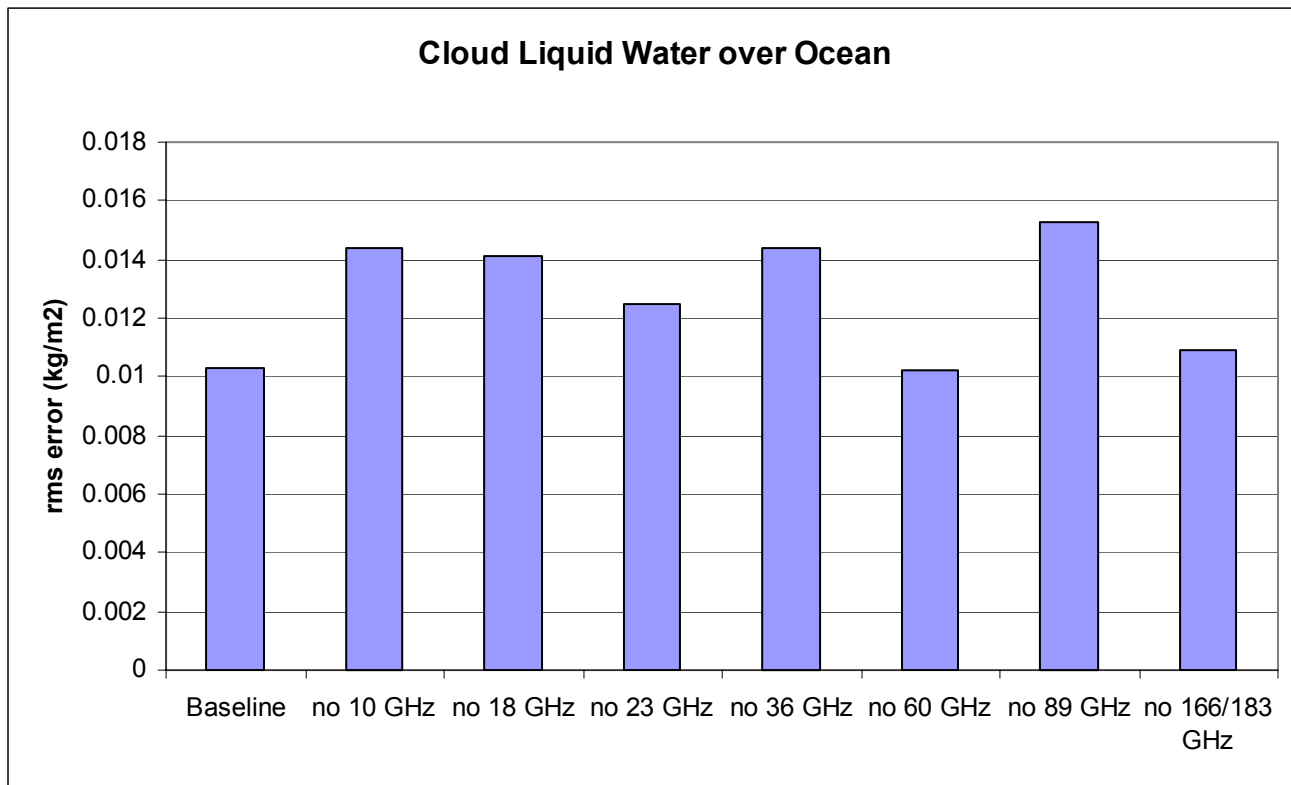


Figure 5-10: Impact of loss of the indicated bands on cloud liquid water retrieval error.

The algorithm similarly degrades gracefully with the loss of external data. In particular, the mathematical formalism of the physical inversion method accepts external data in the form of statistical constraints, and the method accommodates the inclusion or exclusion of those constraints without any change to the basic retrieval function. The impact of loss of external data is addressed for the individual EDRs in their respective ATBDs.

### 5.5. Sensitivity to Land Surface Emissivity and Prior Knowledge

Retrieval experiments were performed to understand the importance of surface emissivity in the retrieval of EDRs over land, with particular attention to land surface temperature (LST), water vapor, and cloud parameters for clear and cloudy conditions. For convenience, we examined precipitable water (PW) and cloud liquid water (CLW) as they provide a good metric for the impact on water vapor and cloud retrievals, respectively.

Tests were conducted for different types of land surfaces and with varying assumptions about the extent of *a priori* knowledge about the surface spectral emissivity. Operationally, for regions with stable emissivity values, a dynamic, localized emissivity database will be used to provide a

better *a priori* estimate of the surface type and emissivity than would be provided by a climatological database. The core module uses the *a priori* emissivity estimates in the form of a statistical constraint – the *a priori* emissivity spectrum and its error covariance matrix (see Section 4.2.4.1). Improvement from a climatological constraint was modeled by adjusting the entire *a priori* emissivity spectrum from the climatological spectrum toward the “true” spectrum (test-case by test-case) using a scale factor. The square of the same scale factor was applied to the emissivity covariance matrix. As the scale factor was reduced from one experiment to the next, the effect was to simulate improved *a priori* emissivity knowledge. A convenient way to represent the overall quality of the *a priori* emissivity knowledge is with the standard deviation of the *a priori* error (the square-root of the covariance diagonal) between 18 and 23 GHz. That point in the emissivity spectrum is particularly important for vapor and cloud retrieval skill, as demonstrated below.

Figure 5-11 and Figure 5-12 show the retrieval errors as a function of the standard deviation of the 18 & 23 GHz emissivity background error for three surface spectral emissivity types, with the typical emissivity values for these types given in Table 5-2. An *a priori* emissivity standard deviation value of 0.12 corresponds to climatology, while smaller values model the increased knowledge provided by a recently updated database. A value of 0.005 is expected for locations with very stable emissivity values. The magnitude of the decrease in retrieval error as the emissivity retrieval becomes more tightly constrained provides information about the sensitivity of the retrieved parameter to surface emissivity *a priori* knowledge. For LST there is very little impact due to the type of surface, but there is a strong dependence on the *a priori* emissivity knowledge. In contrast, for PW and CLW there is a strong dependence on both emissivity (surface type) and the *a priori* emissivity knowledge. For cloudy sky regions the benefit of emissivity knowledge is diminished for PW. For PW, improved *a priori* emissivity knowledge reduces the dependence of retrieval performance on 18/23 GHz emissivity (surface type), as is demonstrated by the convergence of the curves for smaller standard deviations.

Table 5-2: Typical emissivity values for the three surface spectral emissivity types shown in Figure 5-11 and Figure 5-12.

Emissivity Type	Typical Emissivity for 18/23 GHz
Mixed Forest	0.94 – 0.96
Open Shrub	0.86 – 0.90
Barren/Sparse	0.80 – 0.86

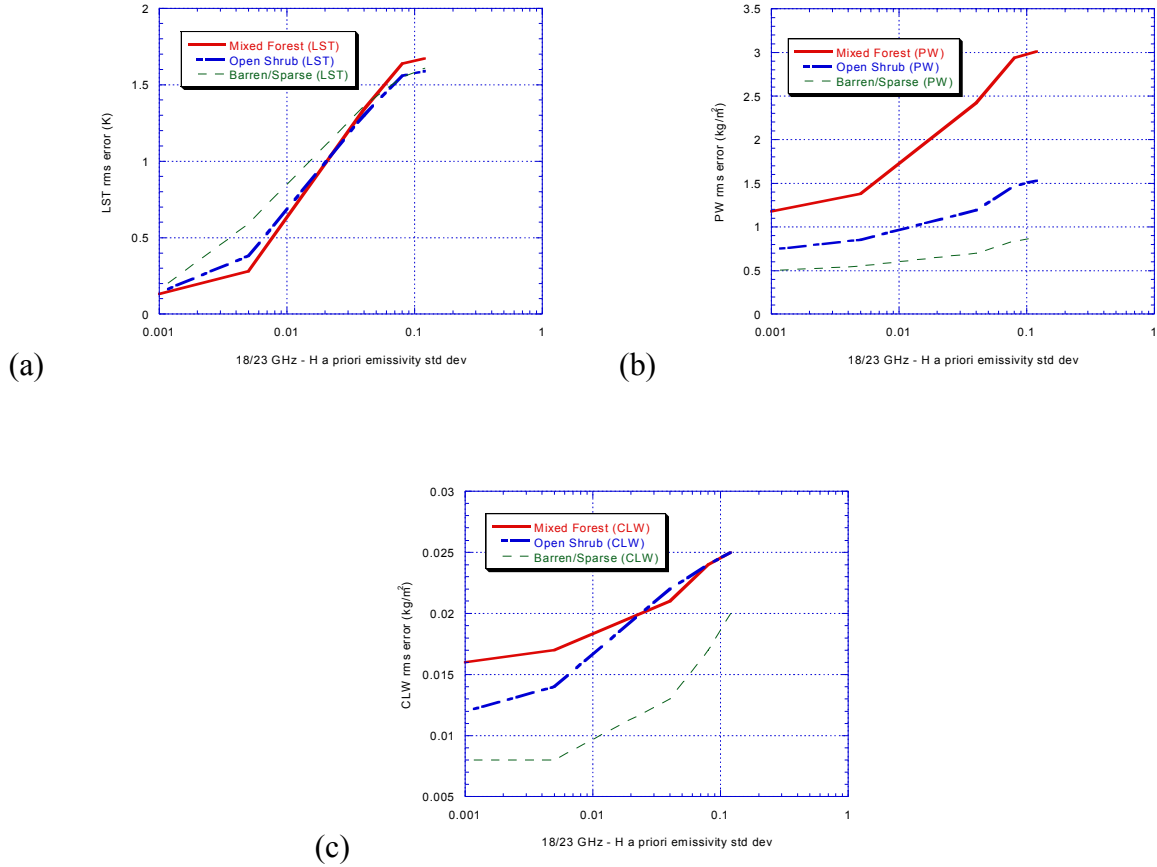


Figure 5-11: Impact of *a priori* land surface emissivity information on clear sky retrievals of (a) land surface temperature, (b) precipitable water, and (c) cloud liquid water.

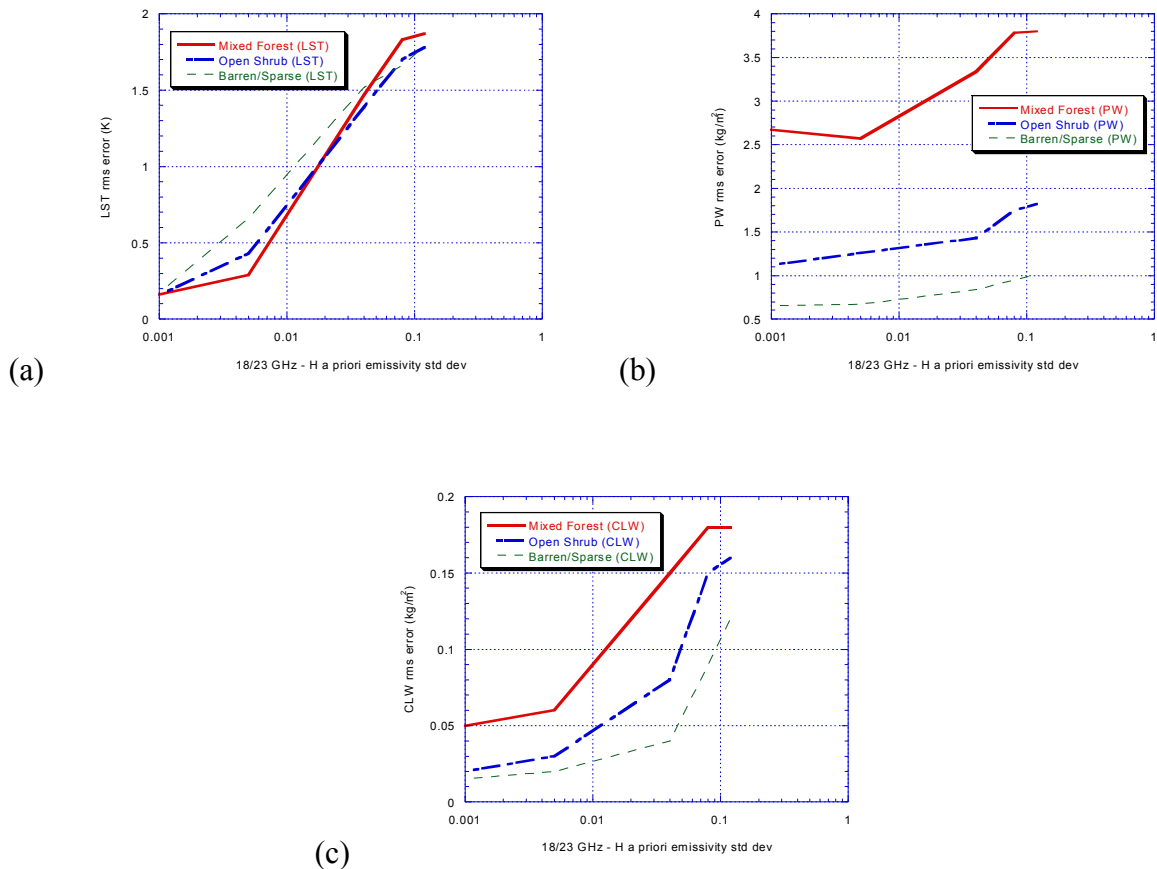


Figure 5-12: Impact of *a priori* land surface emissivity information on cloudy sky retrievals of (a) land surface temperature, (b) precipitable water, and (c) cloud liquid water.

More discussion of issues regarding retrievals over land surfaces is in the individual EDR ATBDs, and particularly the ATBD for Water Vapor EDRs (Vol. 3).

## 5.6. Quality Control

The preliminary functional diagram for the physical inversion is presented in Figure 5-13 and addresses how the algorithm will ensure the quality of the retrieved water vapor profile and column, temperature profile, CLW, and surface EDRs obtained from the core module. A full physical inversion is first performed using all of the CMIS channels. For the cases in which a physical model is not adequate, leading to possible rain-flagged or rejected retrievals, the algorithm will revert to empirical techniques (e.g. a neural-net) to perform the retrieval. The details of these algorithms are given in the ATBD Volume 5 (“Precipitation Type and Rate”), and Volume 7, Part 2 (“Cloud Ice Water Path EDR”) and Part 3 (“Cloud Liquid Water EDR”).

The rationale for first doing the full physical retrieval is dictated by the atmospheric water vapor profile (AVMP) EDR requirements (one of the “1A” EDRs). The physical algorithm is able to provide a more strict test on the retrieval quality than an empirical method. Thus proper convergence of the physical retrieval algorithm ensures “clear-sky” quality for the AVMP EDR. The majority of cases are expected to be successful retrievals and will require no further processing. However, the presence of ice clouds will affect the 166 and 183 GHz channels, depending on the IWP, mass median diameter, and cloud top. In this case there is no longer consistent information between the 166 and 183 GHz channels and the 22 GHz channel and the retrieval will not converge. It is possible, however, for the algorithm to achieve convergence for some ice cloud cases by increasing the water vapor amount below the cloud top to compensate for the ice signal present in the H<sub>2</sub>O sounding channels. However, the water vapor product may still be degraded beyond the threshold, though we may not know it if the residual is small. This behavior has been evaluated and is described below in Section 5.6.1. For this reason, the VIIRS data or EDR product (cloud top height, optical depth and ice water path) is required by the CMIS algorithm.

If ice is detected, two retrieval modes are possible:

- 1) In weather centers which have reasonable computing capability, the multiple-scattering can be turned on for high frequencies only (89 GHz and above), and the retrieval is repeated after adding ice cloud parameters to the state vector (cloud top, median particle diameter and IWP). Note that the production of an IWP EDR is required.
- 2) For weather centers with minimal computing capability, the high frequency channels will be turned off and the process will be repeated using only the frequencies up to 60 GHz. In this case no water vapor profile is reported.

As stated above, when multiple-scattering is included in the retrieval algorithm it is only used for the 89 GHz and higher frequency channels. The rationale for this is that minimizing the number of channels for which the multiple-scattering is computed will significantly reduce the computational resources required to perform the retrieval. The lower frequency channels may neglect multiple scattering because its intensity in precipitating clouds with large particles is proportional to the frequency raised to the power 1.76 (G. Petty private communication, 2000). For small particles the spectral gradient is even larger. For cases where the cloud contains

mixed-phase particles or a very complex structure the retrieval performance will be significantly degraded even if multiple-scattering were included, due to the inability of any algorithm to adequately capture this structure.

For some ice cloud cases the temperature profile will be modified to obtain convergence due to a lack of redundant information in the CMIS channels. The radiometric information is insufficient to detect these cases and must be supplemented with spatial information. Thus the temperature profile will be compared with the profile obtained by interpolating the neighboring (ice and CLW free) grid points. A threshold will be set on how much  $T(p)$  can deviate from these values. Note that this is similar to a technique used to derive rain-rates from a combination of clear and cloudy scenes [Staelin et al., 2000].

Similarly, with warm precipitation, the impact of scattering by large cloud droplets or rain drops on temperature and water vapor profiles needs to be dealt with. The current plan is to rely on the retrieved CLW value. The CLW threshold is currently set to 0.3 mm.

As shown in Figure 5-13 there is a direct link between the core module and the algorithm used for the retrieval of precipitation. The interface between these routines is determined by the core module quality control tests. Several flags added to the core module retrieval output indicate both the path followed in producing the EDRs and the degree of confidence in the quality of the retrieval product. These flags are detailed in Table 5-3.

Table 5-3: List of flags included in the core module output.

Core Module Output Flag	Value
Channels Used	LF (only frequency < 89 GHz) HF (including frequency $\geq$ 89 GHz) (these will be refined to include specific channels used)
VIIRS Data	Included or Not-Included in retrieval
Multiple Scattering	Included or Not-Included in retrieval
Quality of Retrieval	1 = Retrieval meets all quality control criteria (see Section 4.3) 2 = Convergence Achieved but CLW > 0.3 mm 3 = Retrieval rejected

The retrieval path is entirely characterized by a description of the channels used in the retrieval and a flag indicating whether or not multiple scattering was turned on. In addition, the cloud

liquid water (CLW) and ice water path (IWP) variables used by the precipitation algorithm are available to provide information about the cloud type.

The core module is first applied at 50 km spatial resolution. If the retrieval meets all of the quality control criteria, the “Quality = 1” flag is set, while the “Quality = 2” flag indicates the possible presence of rain. Currently no further processing at a higher spatial resolution will occur if the “Quality = 3” flag is set for the 50 km cell, indicating that the retrieval failed to meet the quality control criteria. The quality control tests are more strict for the core module than for the precipitation retrieval algorithm. For instance, there is a test for the presence of ice clouds regardless of whether or not there is precipitation present. The strict tests of quality control ensure that precipitation will only occur in areas where the quality control has failed. The precipitation algorithm will be applied only to those footprints that pass the core module quality control (i.e. Quality = 1 or 2). This avoids having to feed back the output from the precipitation algorithm into the core module output, thus saving computational resources and simplifying implementation.



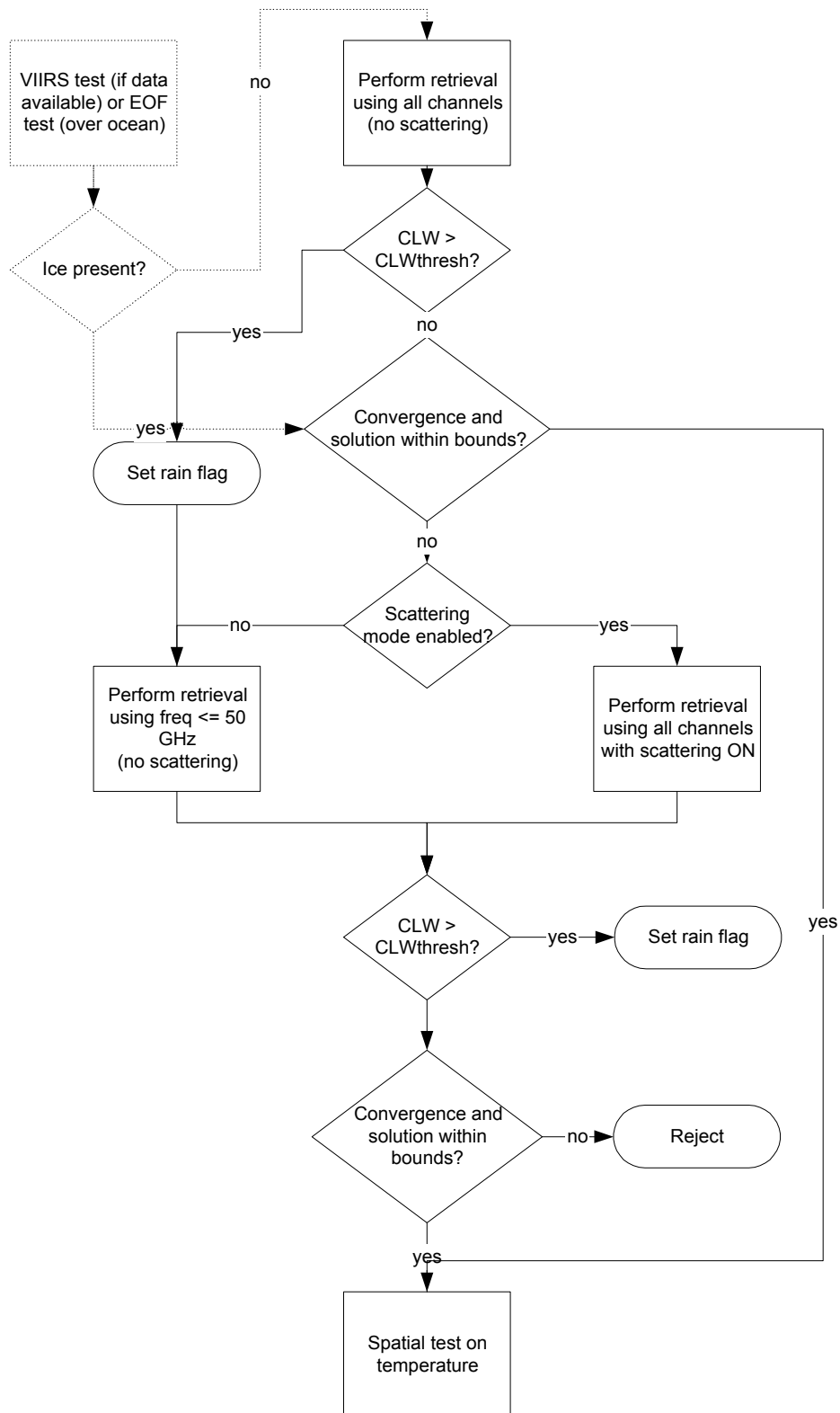


Figure 5-13: Preliminary Functional Diagram for the Physical Inversion.

### 5.6.1. Impact of Ice Water Path (IWP) on Retrieval Process and Performance

Figure 5-14 shows an example of how the presence of ice water path (IWP) can impact the retrieval process and affect the EDR performance without necessarily preventing the algorithm

convergence. A test scene was calculated for a nominal cirrus cloud top of 250 mb. Differences between clear-sky and cloudy-sky radiances determine the minimum detectable IWP for each of the CMIS channels. Each curve in Figure 5-14 represents the minimum value of the IWP required so that the radiance due to the IWP is larger than the sensor noise level. From this figure it is clear that the 183 GHz channels are the most sensitive to the presence of ice. This test assumed the sensor noise level appropriate for a 30 km field-of-view. Moving to a 50 km FOV will reduce the noise, thus making the algorithm sensitive to even smaller values of the IWP.

Although a change in radiance due to increased IWP may be larger than the noise level, this does not necessarily mean that the retrieval will fail the quality control tests (described in Section 4.3). Indeed null-space errors allow for retrieval convergence even with some discrepancy between the measured brightness temperature and the simulated one. Figure 5-15 shows that it is not until the IWP gets quite large, particularly for small particle sizes, that the retrieval algorithm fails to converge. In region I, below the solid curve, the ice is transparent to the CMIS channels. In region III, however, the effect of ice will sufficiently degrade the retrieval performance and the quality control criteria will not be met. Potential problems exist for situations that fall into region II. Here the retrieval will converge, but only because other parameters (water vapor in particular) have been altered to compensate for the IWP. This will degrade the accuracy for these retrievals from the clear-sky performance values. In this region the CMIS information alone is insufficient for detecting the presence of ice water clouds and the retrieval will be degraded. VIIRS data will be used to detect these conditions and flag the water vapor retrievals appropriately. However, if external information does not exist then there is not enough information to determine that these are actually scattering-impacted retrievals, and the retrieval results will be degraded. The claimed clear-sky performance should therefore be weighted by these cases.

To illustrate the impact of IWP on the retrieval process, retrievals were conducted for a set of IWP values with a Dme of 700  $\mu\text{m}$ . The range of variability of the IWP was chosen in order to cover the three regions in Figure 5-15, i.e., no impact to the signal, the non-convergence region, and the area in between. Figure 5-16 shows the percentage of points that passed the QC as a function of IWP. This is consistent with Figure 5-15 showing that in clear sky, all of the points will pass the QC test. Above 40  $\text{g/m}^2$ , <15% of the points passed the QC (which corresponds to the area above the dotted curve in Figure 5-15). In region II of Figure 5-15, for an IWP of 20  $\text{g/m}^2$ , >70% of the points passed the QC. The temperature and water vapor retrieval results are

shown in Figure 5-17. The temperature is only moderately impacted because the 50 GHz sounding channels are less impacted by scattering than the other, higher frequency, channels. However, the water vapor errors peak below the simulated ice cloud as a result of compensating for the IWP-induced signal. Figure 5-18 shows the retrieval *rms* and bias for TPW, Figure 5-19 shows the results for CLW, and Figure 5-20 shows the *T<sub>skin</sub>* retrieval results. These retrieval statistics are calculated only for the profiles that passed the quality control criteria. It is clear that there is considerable degradation in the retrieval results that is not evident from the QC criteria for values of IWP that fall in the retrieval null-space (region II) of Figure 5-15.

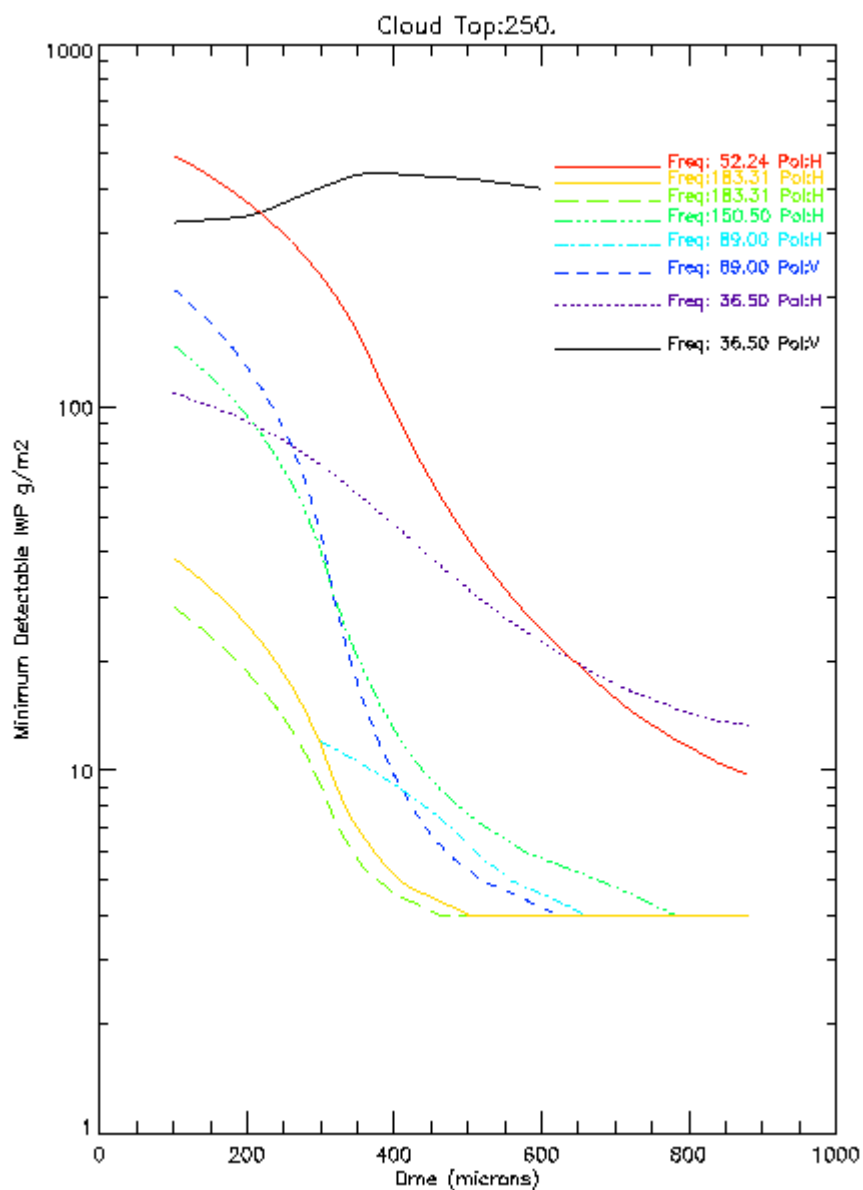


Figure 5-14: Minimum detectable IWP as a function of the mean diameter of the particle size distribution, defined as the minimum amount of ice necessary to induce a brightness temperature change greater than the sensor noise for a given channel. The cirrus cloud top in this case is 250 mb and its thickness is 50 mb.

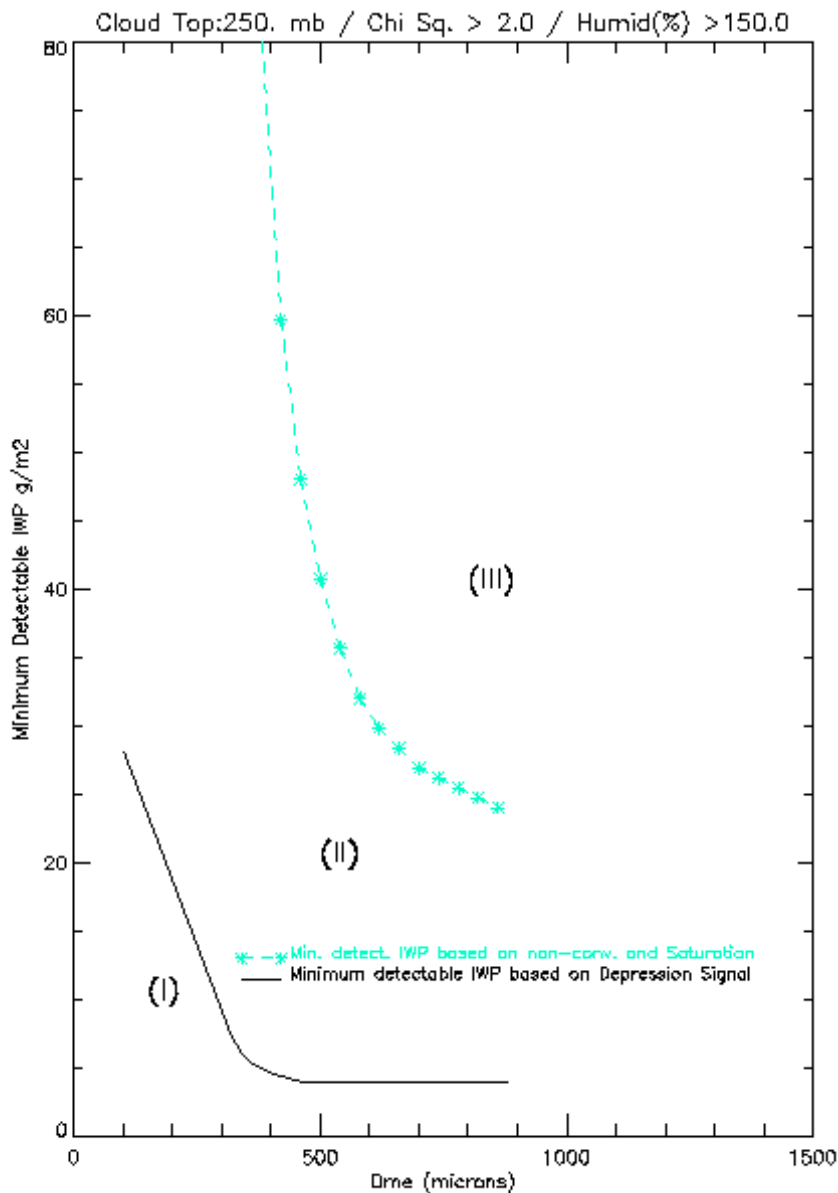


Figure 5-15: The solid curve shows the minimum detectable IWP based on the IWP induced depression for the worst of the channels (183 GHz). The dotted curves show the minimum detectable IWP based on the convergence failure criterion. Below the solid curve there is little impact on the retrieval. The curve with “+” symbols represents the chi-square converge criterion while the curve with “\*” symbols represents that obtained when using both the chi-square and super-saturation as a quality control metric. In the region between the solid curve and “\*” curve the retrieval passes the quality control, but the EDR performance is degraded.

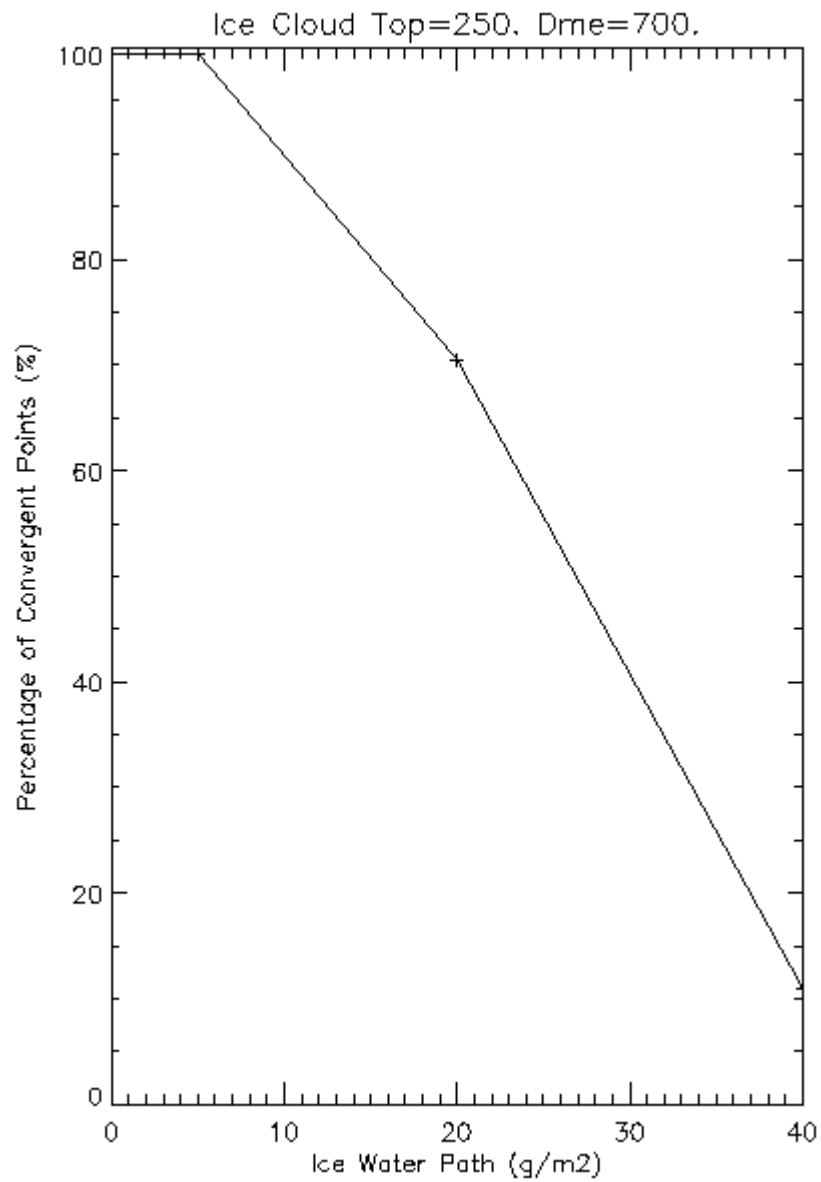


Figure 5-16: Percentage of points (out of 200 total) that did pass the quality control tests for IWP values of 0, 5, 20, and 40 g/m<sup>2</sup>.

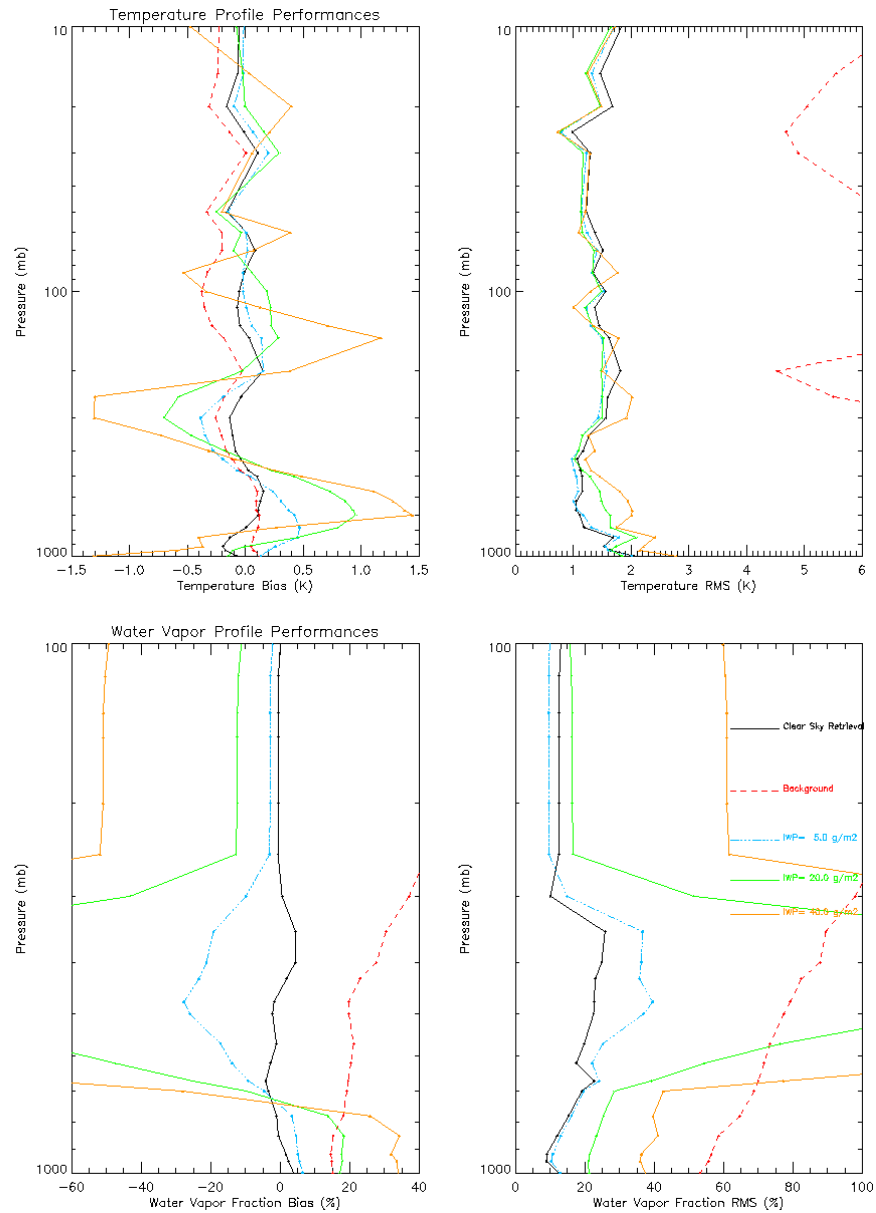


Figure 5-17: Impact of IWP (*rms* and *bias*) on the temperature and moisture profile retrievals.

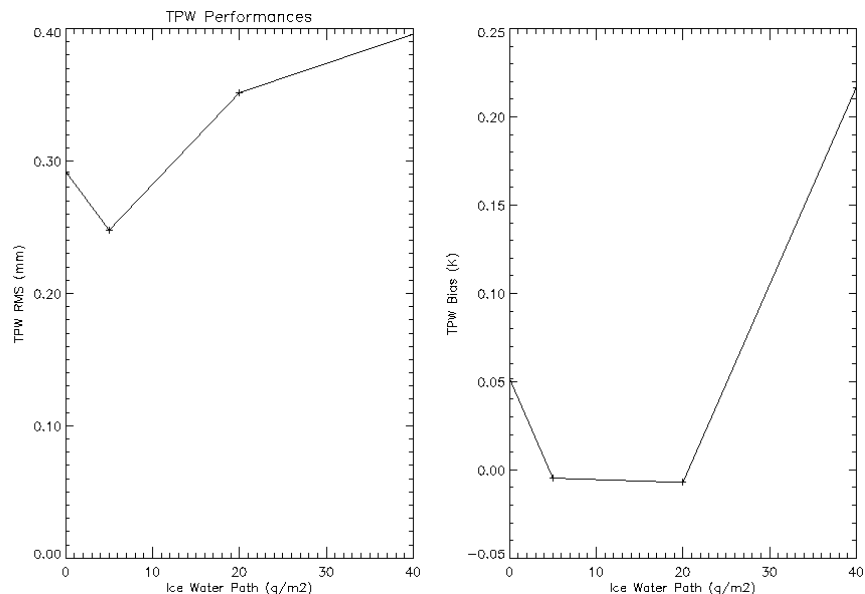


Figure 5-18: Impact on TPW (*rms* and *bias*) of not explicitly accounting for the scattering in the retrieval process while the brightness temperatures are affected by increasing values of the IWP (with a Dme of 700  $\mu\text{m}$  and a cloud top at 250 mb).

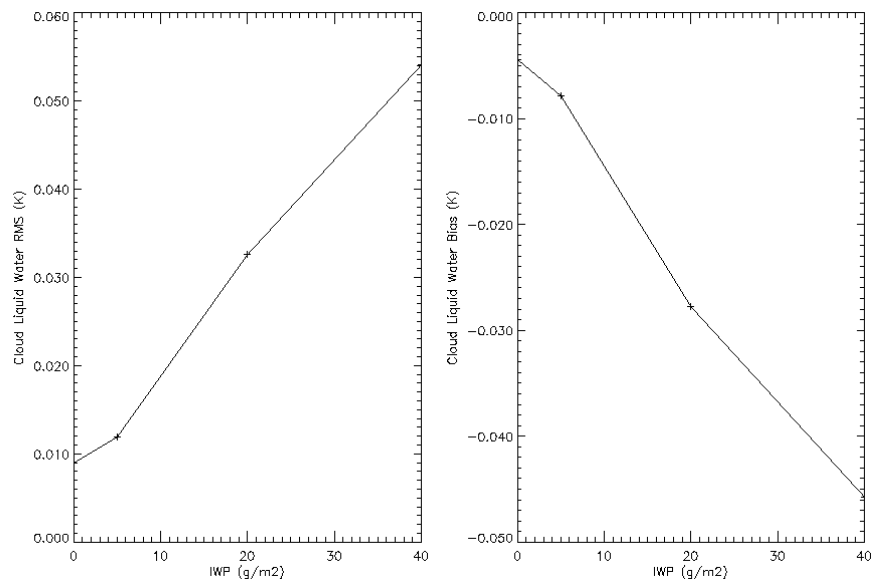


Figure 5-19: Impact on CLW (*rms* and *bias*) of not explicitly accounting for the scattering in the retrieval process while the brightness temperatures are affected by increasing values of the IWP (with a Dme of 700  $\mu\text{m}$  and a cloud top at 250 mb).

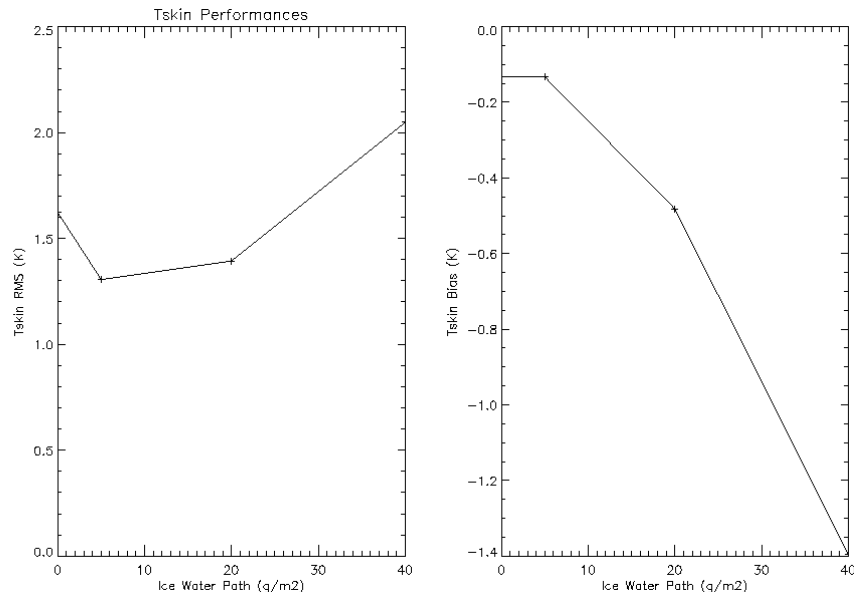


Figure 5-20: Same as previous figure but for Tskin. In this particular case, an IWP of 20 g/m<sup>2</sup> could come as a bias in the Tskin retrieval of more than 0.4 K with only a moderate impact to the points passing the QC test (see Figure 5-16).

It should be noted that the above retrieval simulations include all of the CMIS channels. However, it was shown that the major impact of ice occurs to the higher frequency channels, with the largest impact to the 183 GHz channels. These channels are used for the water vapor profile measurement in order to meet the threshold EDR requirements, and is not required for accurate temperature sounding. One of the steps shown in Figure 5-13 is to perform the retrieval using only the channels less than 60 GHz if ice is present and the scattering-mode of the algorithm is turned off. Figure 5-21 shows the minimum detectable IWP when the channels greater than 60 GHz are not included. The results of these retrievals are shown in Figure 5-22 - Figure 5-24. The use of only those channels less than 60 GHz clearly impacts the retrieval of temperature, even though these channels are less sensitive to ice particles than the higher frequency channels, because some temperature information is contained in the high-frequency channels.



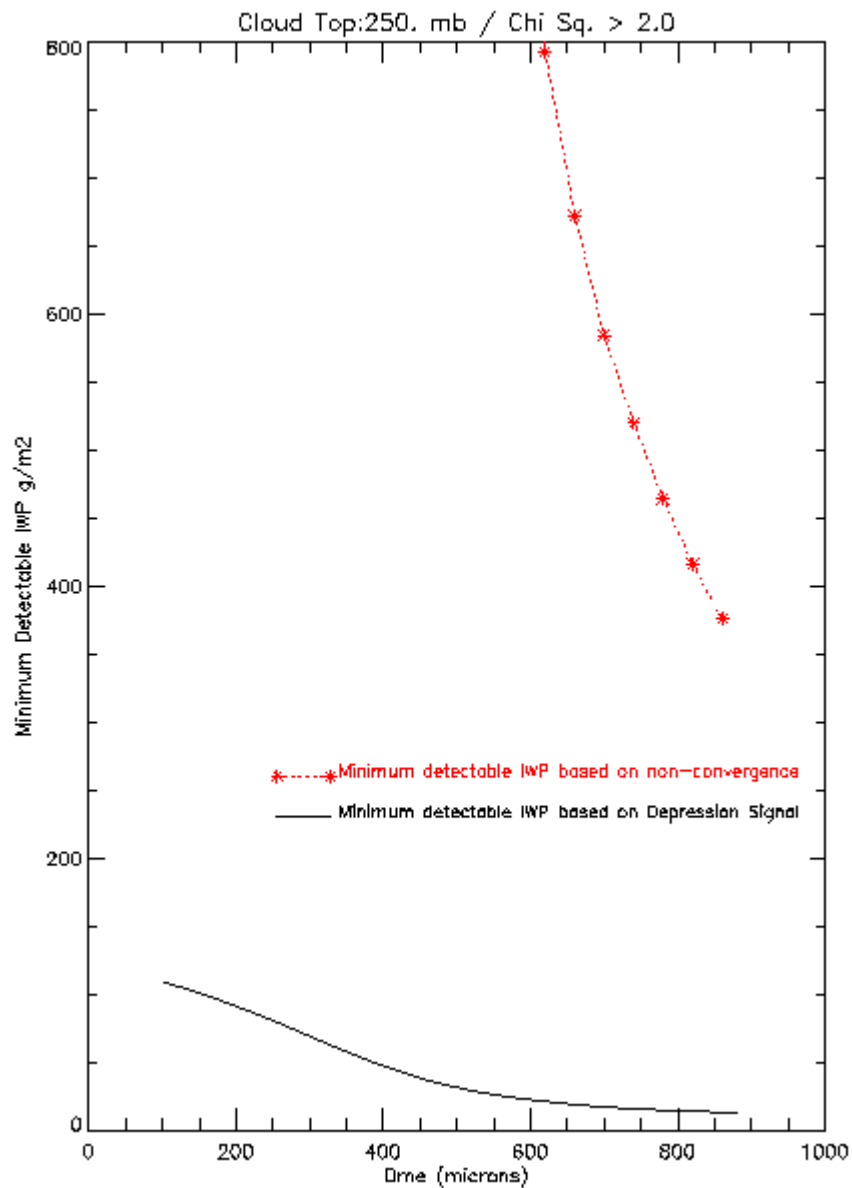


Figure 5-21: Minimum detectable IWP when the channels above 60 GHz are ignored. The solid curve shows the minimum detectable IWP based on the IWP induced depression for the worst of the channels (60 GHz). The dotted curve shows the minimum detectable IWP based on the chi-squared convergence failure criterion.

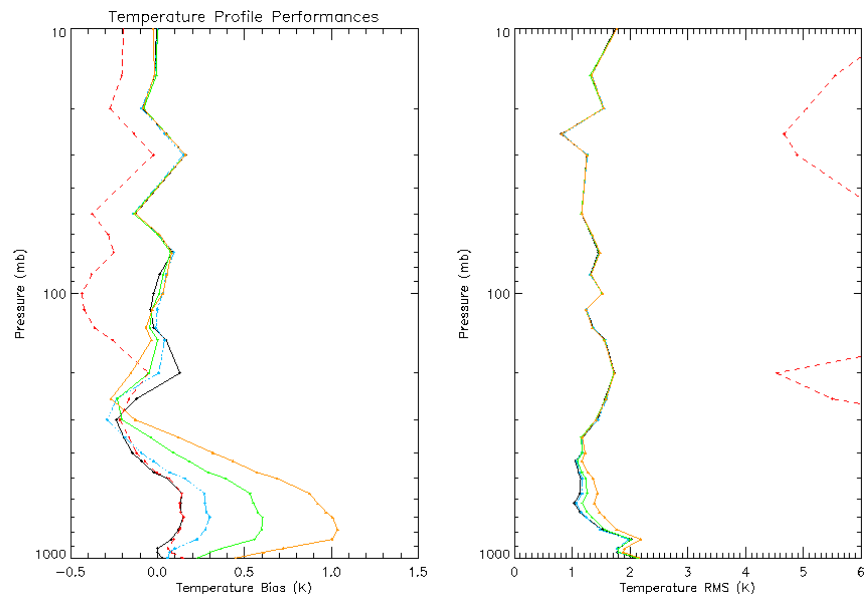


Figure 5-22: Impact of IWP on the temperature and moisture profile retrieval when using only the channels less than or equal to 60 GHz. In this case there is no report for the moisture profile.

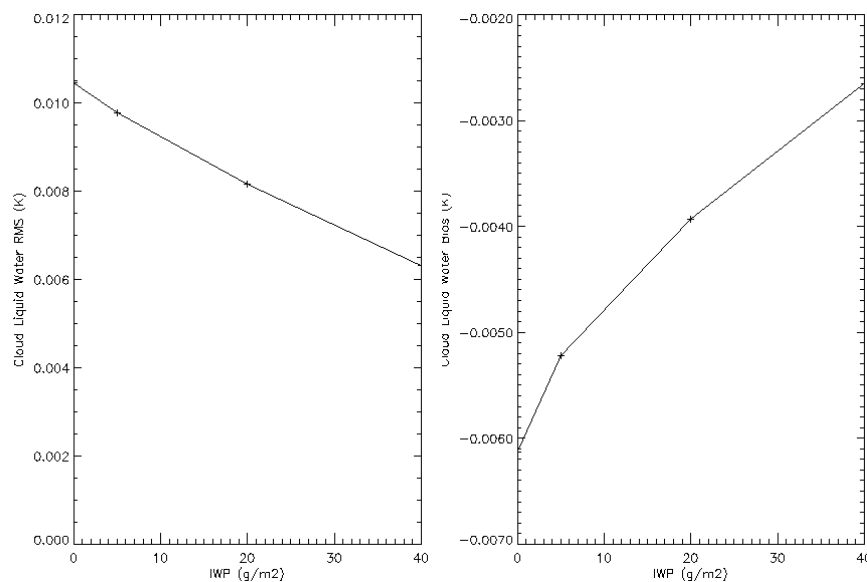


Figure 5-23: Impact on the CLW (*rms* and *bias*) of not explicitly accounting for the scattering in the retrieval process while the brightness temperatures are affected by increasing values of the IWP (with a  $D_{me}$  of 700  $\mu\text{m}$  and a cloud top at 250 mb). This retrieval test used only the channels less than or equal to 60 GHz.

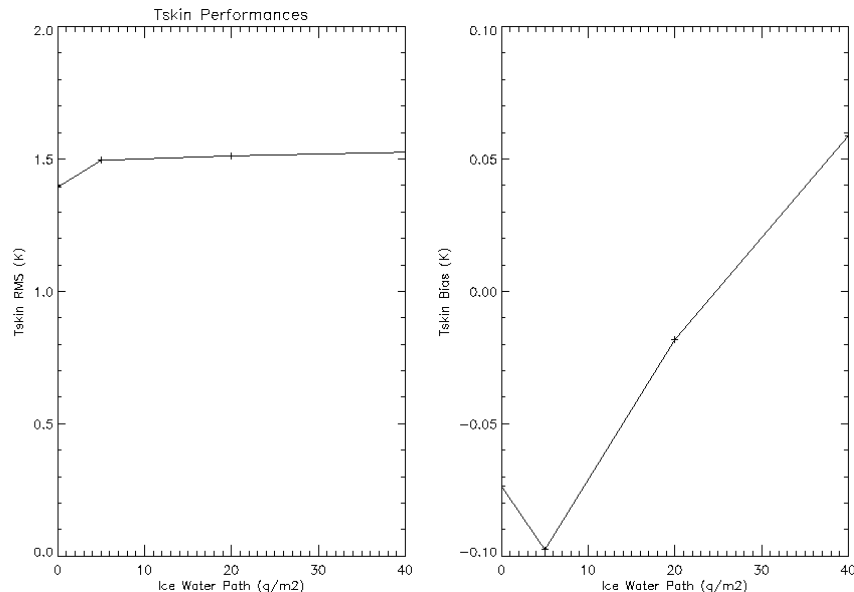


Figure 5-24: Same as previous figure but for Tskin, using only the channels less than or equal to 60 GHz.

### 5.6.2. Impact of Precipitation on Retrieval Process and Performance

Figure 5-25 – Figure 5-29 show an example of how the presence of precipitation can impact the retrieval process and affect the EDR performance. As with IWP, given in Section 5.6.1, precipitation may impact the EDR performance without preventing the algorithm convergence. Test scenes were calculated for cloud top pressures between 400 and 850 mb and the minimum detectable rain-rate (RR) was determined by the point at which the retrieval no longer passes the quality control criteria. As shown in Figure 5-25 this was computed for a retrieval using (a) all of the CMIS channels and (b) for neglecting those channels above 60 GHz. From these plots it is clear that the channels below 60 GHz are much less sensitive to the presence of rain than the channels above 60 GHz. For this reason the algorithm will revert to a retrieval using only the channels below 60 GHz if rain is detected in the field-of-view (Figure 5-13).

As a specific example of the impact of precipitation on the EDR retrievals, Figure 5-26 – Figure 5-29 show the EDR retrieval performances for using all CMIS channels and for neglecting the channels above 60 GHz. These results are for a cloud rain top at 700 mb. Figure 5-26 shows the number of convergent profiles for various values of the rain-rate, and is consistent with the results shown in Figure 5-25. The temperature, cloud liquid water, and Tskin results are shown in Figure 5-27 – Figure 5-29. These simulations have assumed the sensor noise level appropriate for a 30 km field-of-view. Moving to a 50 km FOV will reduce the sensor radiometric noise, thus making the algorithm sensitive to even smaller values of the rain-rate.

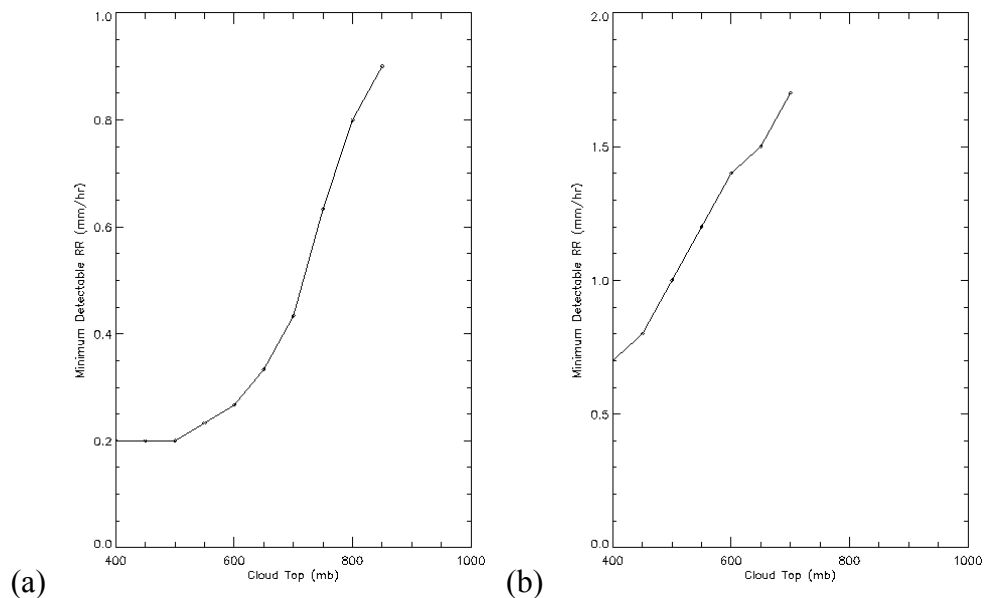


Figure 5-25: Minimum detectable rain-rate (RR) as a function of the cloud top pressure for (a) all channels and (b) ignoring the channels above 60 GHz.

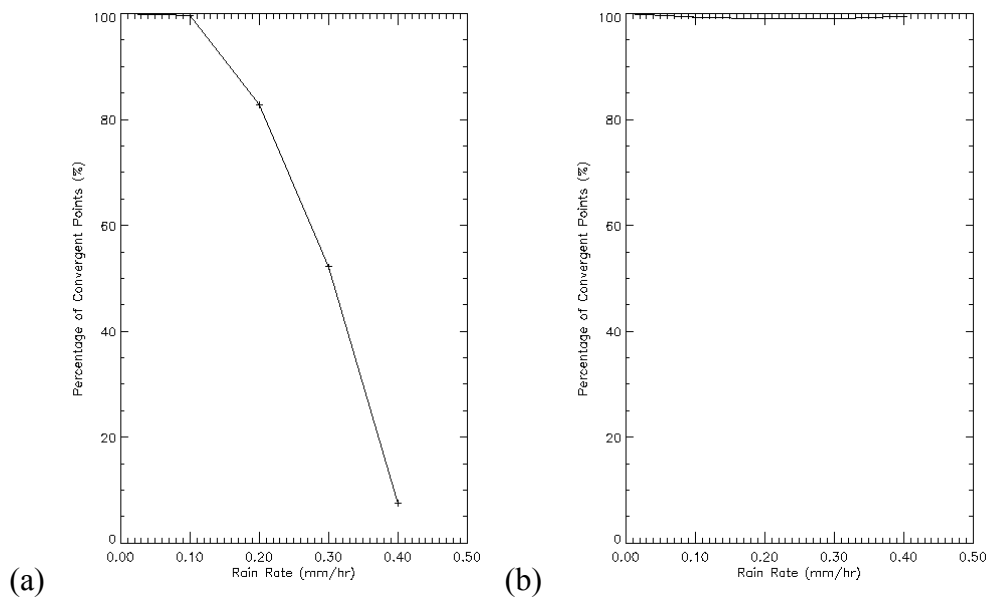


Figure 5-26: Number of convergent points when (a) using all CMIS channels and (b) neglecting channels above 60 GHz. Note that the small amounts of rain have a much larger impact on the channels above 60 GHz.

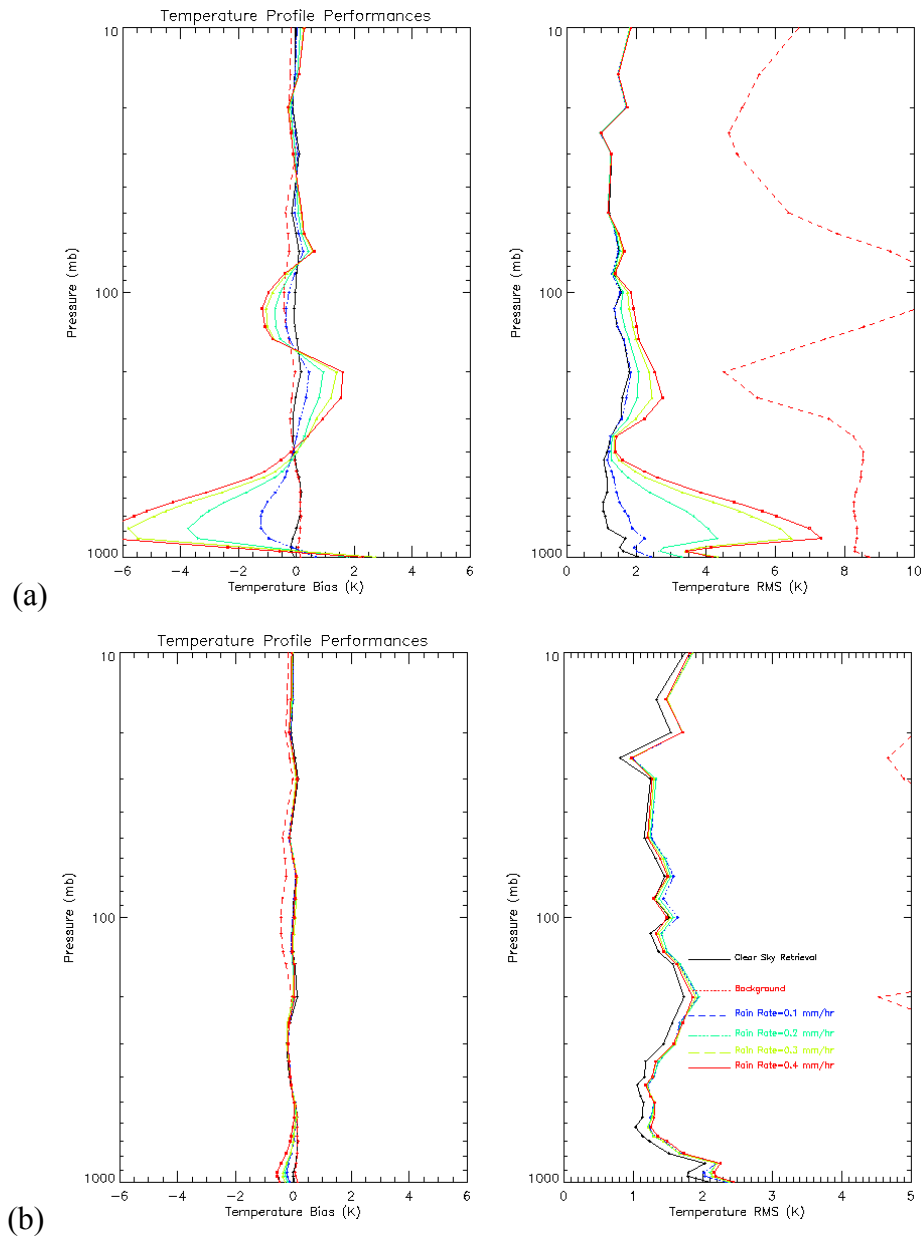


Figure 5-27: Impact of rain-rate on the temperature profile retrieval (a) for all CMIS channels and (b) when neglecting channels above 60 GHz. Note that in this case there is no report for the moisture profile

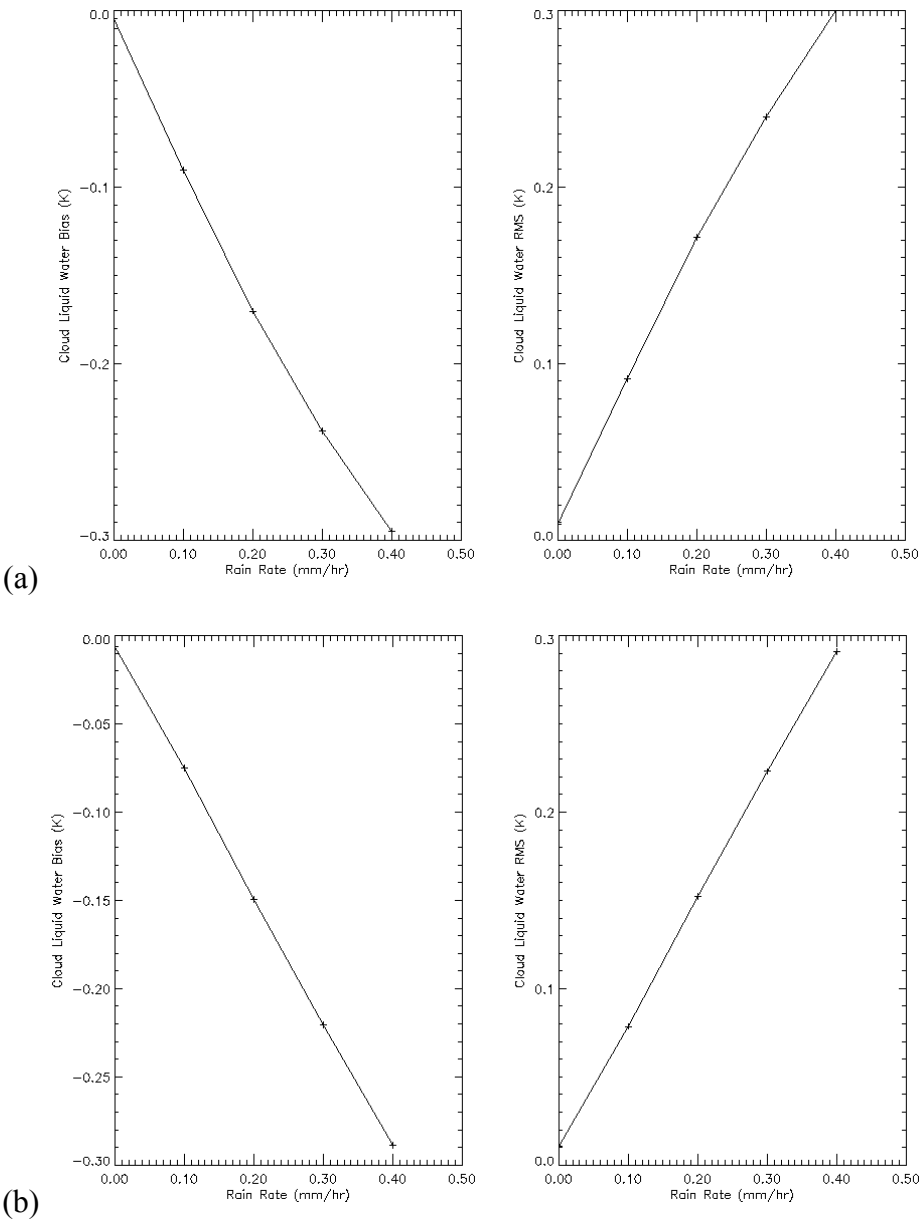


Figure 5-28: Impact of rain-rate on the CLW retrieval (a) for all CMIS channels and (b) when neglecting channels above 60 GHz.

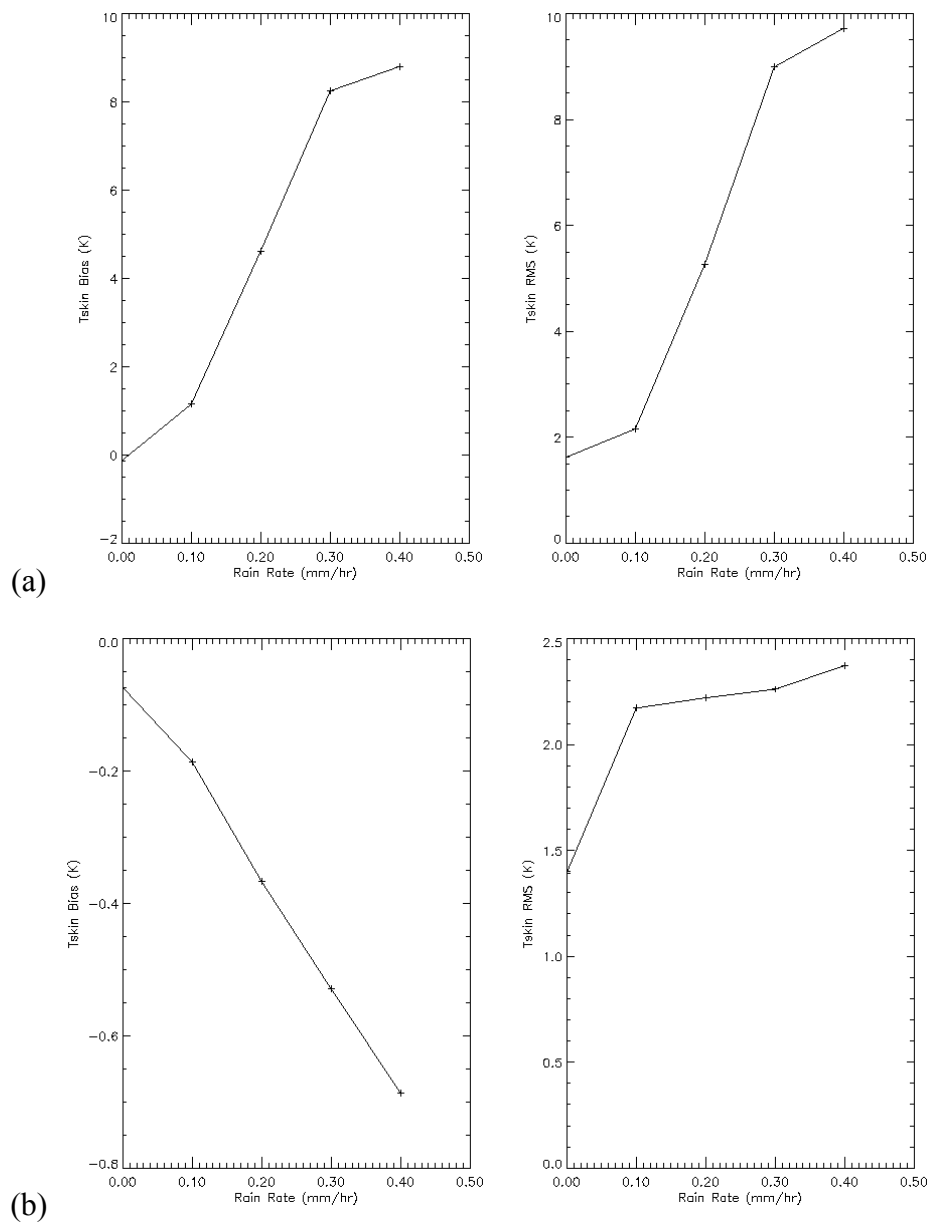


Figure 5-29: Impact of rain-rate on the retrieval of T<sub>skin</sub> (a) for all CMIS channels and (b) when neglecting channels above 60 GHz.

## **6. APPENDIX 1: THE NOAA-88 GLOBAL ATMOSPHERIC PROFILE DATA SET**

### **6.1. Introduction**

The original source of the NOAA-88 data is from the NOAA radiosonde/satellite match archive, known as DSD5. In this data set the radiosonde profiles are recorded at NOAA 40 pressure levels with a minimum pressure of 0.1 mb. The upper levels of the profiles (typically  $\leq 10$  mb) were filled in using a rocketsonde archive. The 40 level profile was then interpolated onto a 66 level standard grid which has a minimum pressure of 1 mb. The 1988 global data set of 8344 profiles contains atmospheric profiles of pressure layer column water vapor and pressure level temperatures. Other parameters accompanying each profile include surface pressure, skin temperature, latitude, longitude and date. The profiles are used to demonstrate the performance of the algorithms and the sensitivity to instrument or algorithm design tradeoffs. Outlined are some statistics of the data set and modifications that have been made to improve the global data set.

### **6.2. Statistics of the Data Set**

To obtain a better understanding of the global data set, statistics were calculated for some of its parameters. Figure 6-1 shows the distribution of observations with respect to latitude. Figure 6-2 shows the histogram of reported surface pressure. Note that the majority of the profiles have a surface pressure of 1000 mb, though some are at 850, 920 or 950 mb. This indicates that the surface pressures were interpolated onto the nearest pressure grid level for each profile. Figure 6-3, the distribution of observations with month, shows a strong peak for January but no observations at all in March. Figure 6-4, the distribution of observations with the time-of-day, shows peaks around the noon and midnight, consistent with standard radiosonde release procedures. A histogram of the total water vapor amounts is shown in Figure 6-5.

### **6.3. Modifications**

#### **6.3.1. Surface Pressure**

The standard NOAA-88 pressure grid includes the values 850, 925, 950, and 1000 mb. The reported surface pressure values are all on a NOAA-88 grid pressure level with the exception of 920 mb values. This correspondence suggests that either the NOAA-88 grid pressure level of 925 mb was supposed to be 920 mb or that the reported surface pressure values of 920 mb should be 925 mb. Changing the pressure grid level from 925 mb to 920 mb introduced an inversion in the mean temperature profile; thus, it was concluded that the surface pressure values reported at



920 mb must be incorrect. The reported surface pressure values of 920 mb were all changed to 925 mb to match the NOAA-88 data set grid pressure level.

### 6.3.2. Water Vapor Profiles

The water vapor profiles are provided as layer column densities, that is, the integral of the density over the layer. Our radiative transfer model computes radiances from water vapor profiles specified as level densities (e.g. mass mixing ratio) at the level boundaries. We converted the layer amounts to level densities as follows.

The total layer column density amounts for a given constituent  $x$  can be expressed as:

$$u_x = \int \rho_x dz \quad (45)$$

where  $\rho_x$  is the density of the constituent. The mass mixing ratio  $w_x$  is defined as:

$$w_x = \frac{\rho_x}{\rho_d} \quad (46)$$

where  $\rho_d$  is the density of dry air. Rearranging (46) in terms of  $\rho_x$  and substituting it into (45) produces:

$$u_x(z) = \int w_x \rho_d dz \quad (47)$$

Here, we will assume an average mixing ratio over each layer:

$$u_x = \overline{w_x} \int \rho_d dz = \overline{w_x} u_d \quad (48)$$

where  $u_d$  is the column density of dry air. Therefore, all that is needed to solve for the average mixing ratio is  $u_d$  as the  $u_x$  is provided in the data set.

The total column density for each layer is assumed to be:

$$M_{air} u_{air}(P) = M_d u_d(P) + M_{H_2O} u_{H_2O}(P) \quad (49)$$

where  $M_{H_2O}$  is the molecular weights of water vapor and  $u_{air}$  is the total column air density. Using the hydrostatic equation, the total column air density is expressed as:

$$u_{air} = \frac{N_a}{M_{air}g} \int dP \quad (50)$$

where  $N_a$  is Avogadro's number and  $g$  is the acceleration due to gravity. Substituting (50) into (49) and rearranging for  $u_d$  we obtain:

$$u_d = \frac{N_a}{M_d g} \Delta P - \frac{M_{H_2O}}{M_d} u_{H_2O} \quad (51)$$

for each layer. Therefore, the average mixing ratio for each constituent for each layer is computed from applying equation (51) to equation (48). The average mixing ratio value for the layer is assigned to a  $P_{eff}$  level;  $P_{eff} = (P_{layer\ top} + P_{layer\ bottom}) / 2$ . The mixing ratio values were then interpolated back onto the original NOAA-88 pressure grid levels that contained level temperature values. To test this method, the computed mixing ratio values on the pressure grid levels were then used to re-compute layer column densities to compared with the initial NOAA-88 grid layer column density values provided in the data set.

Figure 6-6 (a) shows sample profiles of computed water vapor mixing ratios: shown are both the average values on the effective pressure levels and the level values on the pressure grid levels. Figure 6-6 (b) shows the layer amounts both as given in NOAA-88 and as recomputed from the calculated density profiles. The errors in all cases are small. The largest errors will occur when there are sharp inflection points within the layers, as would be expected from the assumption of a constant mixing ratio over a layer. Figure 6-7 show the histogram of the error in the total column amounts over all the profiles. Comparing these figures with the total column amounts in Figure 6-5 shows that the error is less than 1 percent.

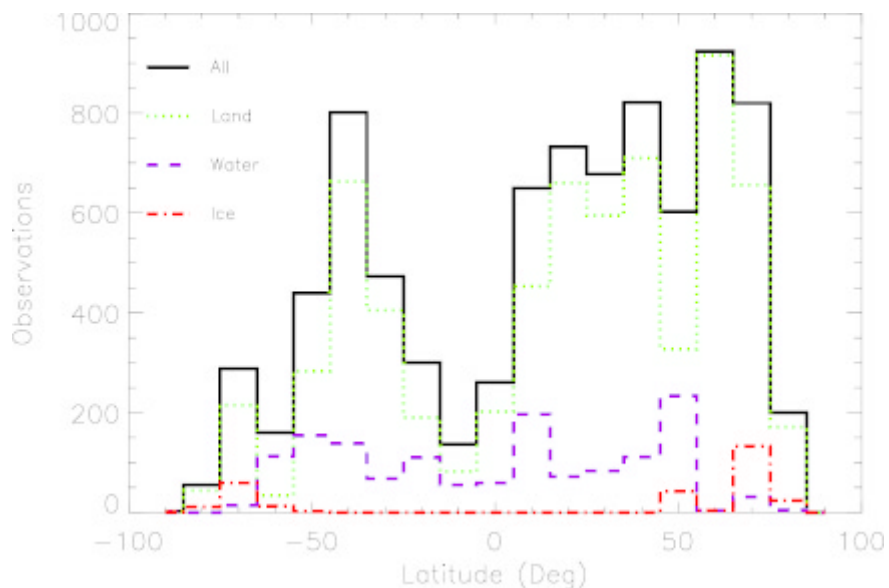


Figure 6-1: Histogram of the number of observations with latitude for the NOAA-88 data set.

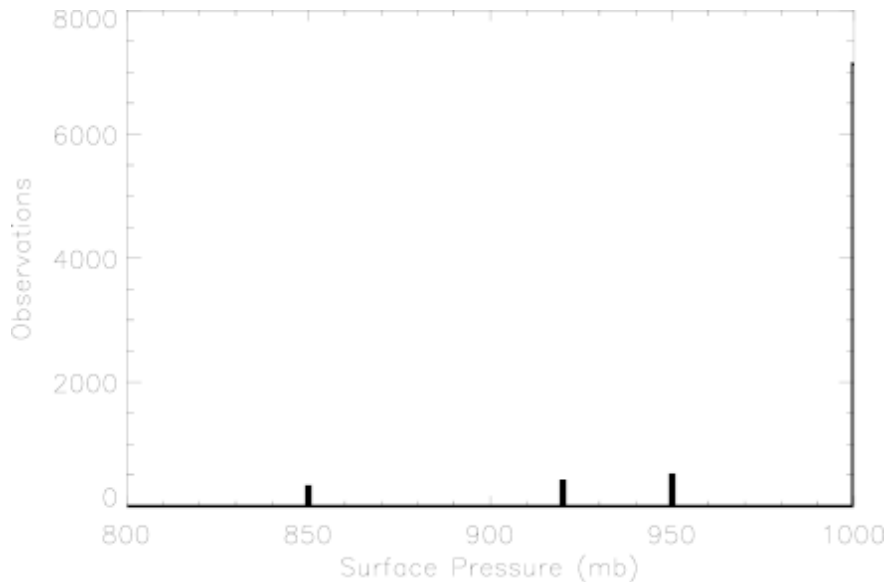


Figure 6-2: Histogram of reported NOAA-88 data set surface pressures.

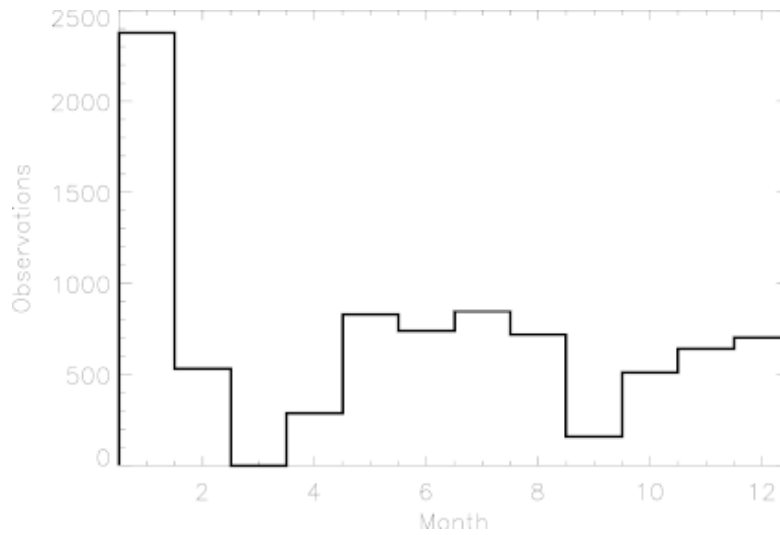


Figure 6-3: Histogram of the number of observations in the NOAA-88 data set for each month.

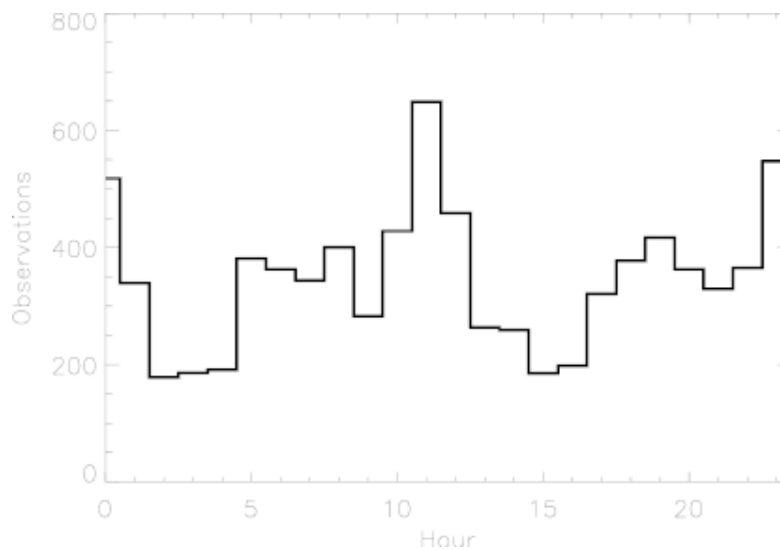


Figure 6-4: Histogram of the time of the day the NOAA-88 data set observations were made.

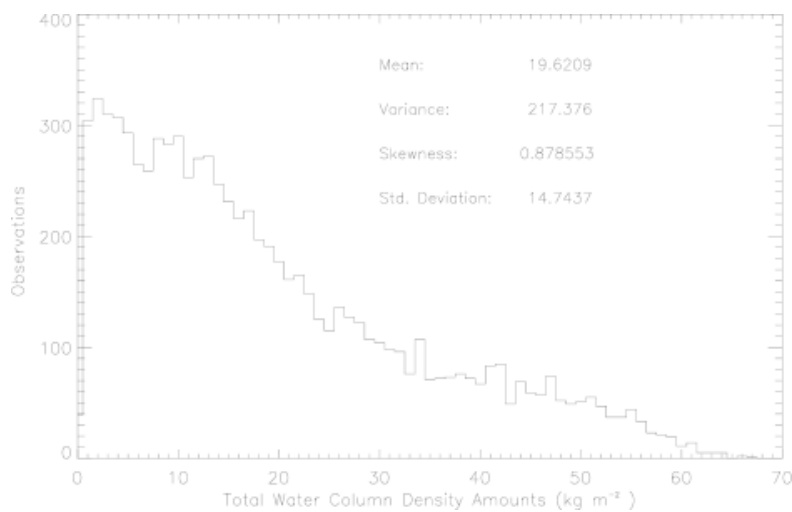


Figure 6-5: Histogram of the total water vapor column density amounts.

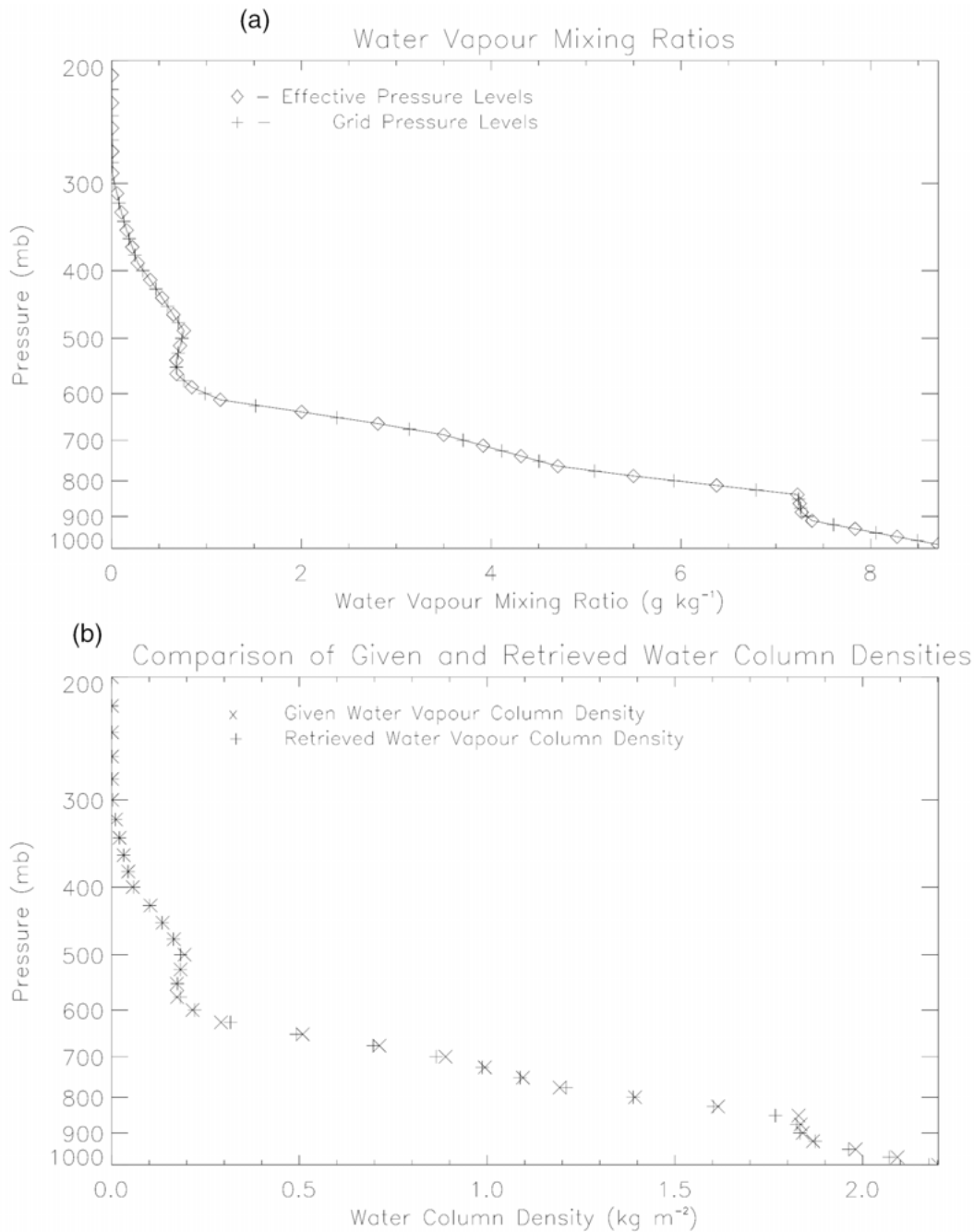


Figure 6-6: The diamonds in plot (a) are profiles of computed pressure levels mixing ratios put on effective pressure levels. The + in this plots are the computed pressure level mass mixing ratio values interpolated back onto the NOAA-88 pressure grid. Plot (b) shows the comparison between the layer column density amounts provided in the NOAA-88 data set and the layer column density amounts computed from the derived pressure level mixing ratio values shown in plot (a).

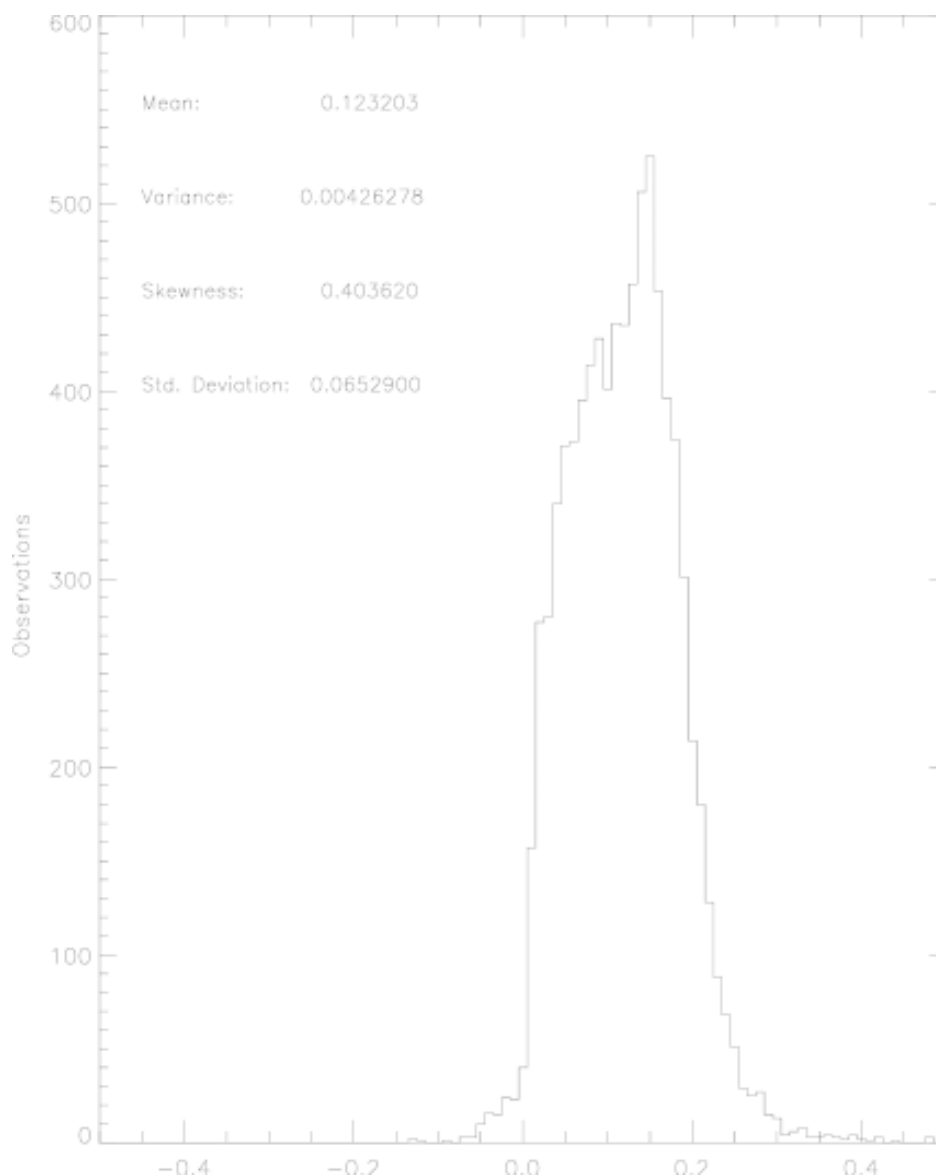


Figure 6-7: Histogram of the difference between the total water vapor column densities provided in the NOAA-88 database and the column densities computed from the derived pressure level mixing ratio values.

## 7. APPENDIX 2: SURFACE PRESSURE COMPUTATION

### 7.1. Basis

Surface pressure needs to be known and is computed from NWP values as follows. Surface pressure of the observed point is computed using satellite inputs (latitude, longitude, time of acquisition of the observable and satellite resolution), NWP data (surface pressure, surface height and virtual temperature) and topography database.

Given a particular point  $X(lat,lon)$  at an altitude  $z$ , we can deduce the surface pressure at this point using the hydrostatic equation for moist air:

$$\frac{dP}{P} = d \ln P = - \frac{g}{R_d T_v} dZ \quad (52)$$

### 7.2. Inputs to the Hydrostatic Equation

The elements needed for the computation of the surface pressure are:

- The surface pressure  $P_{ref}$  which corresponds to the NWP output,
- The height  $H_{ref}$  corresponding to  $P_{ref}$ ,
- The temperature at the height  $h_m = (z + H_{ref}) / 2$ ,
- The specific humidity at the height  $h_m = (z + H_{ref}) / 2$ .

One could reduce the number of inputs by considering the virtual temperature instead of dealing with both the temperature and the specific humidity. In this case, we make the assumption that the virtual temperature is linearly related to the height, the humidity effect on the variation being very small. (See also [EN #97](#) response.)

### 7.3. Interpolation

In case of the NWP data, both interpolation in time and space are necessary. Let us consider that the meteorological data are available with a refresh period of  $\Delta t_{nwp}$ . Usually  $\Delta t_{nwp} = 6hours$ , so that the NWP data are renewed at  $t_{nwp1} = 00h00$ ,  $t_{nwp2} = 06h00$ ,  $t_{nwp3} = 12h00$  and  $t_{nwp4} = 18h00$ .

Let us consider that the resolution in latitude and longitude of the NWP model is  $\Delta Lat_{nwp}$  and  $\Delta Lon_{nwp}$ .

As far as the satellite is concerned, let us consider that the data acquisition has been done at a time  $t_m$  and the measurement (center of the footprint) corresponds to a geographical location X defined by the latitude  $lat_m$  and the longitude  $lon_m$ . The satellite is supposed to have a spatial horizontal resolution that could be defined by the grid of length  $dlon_m$  and a width  $dlat_m$ .

Then the inputs for our module will be three arrays corresponding to three inputs (height, surface pressure and virtual temperatures). Each array correspond to four space points ( $Y_i$  where  $i=1,4$ ) surrounding the point X, at two different times  $t_{nwp(i)}$  and at two different heights  $H_{ref1}$  and  $H_{ref2}$ . These heights must correspond to the levels surrounding the altitude  $z$  so that  $t_{nwp(i)} \leq t_m \leq t_{nwp(i+1)}$  and  $H_{ref1} \leq h_m \leq H_{ref2}$ .

In case the surface at an altitude  $z$  is below the lowest level of the NWP model, the module expects the two lowest NWP levels. Extrapolation will be made to the altitude  $z$ .

The interpolation is then performed in time and then in space (latitude/longitude). The hydrostatic equation is then used to compute the surface pressure (interpolation in height).

Instead of handling both the temperature and the specific humidity, we will make the assumption that the virtual temperature varies linearly in  $z$ , that is:

$$\frac{\partial T_v}{\partial z} = const \quad (53)$$

The Lagrange two point interpolation formula (linear interpolation) is used for interpolation in time and in height.

The interpolation in space (latitude/longitude) is a four point bilinear method.



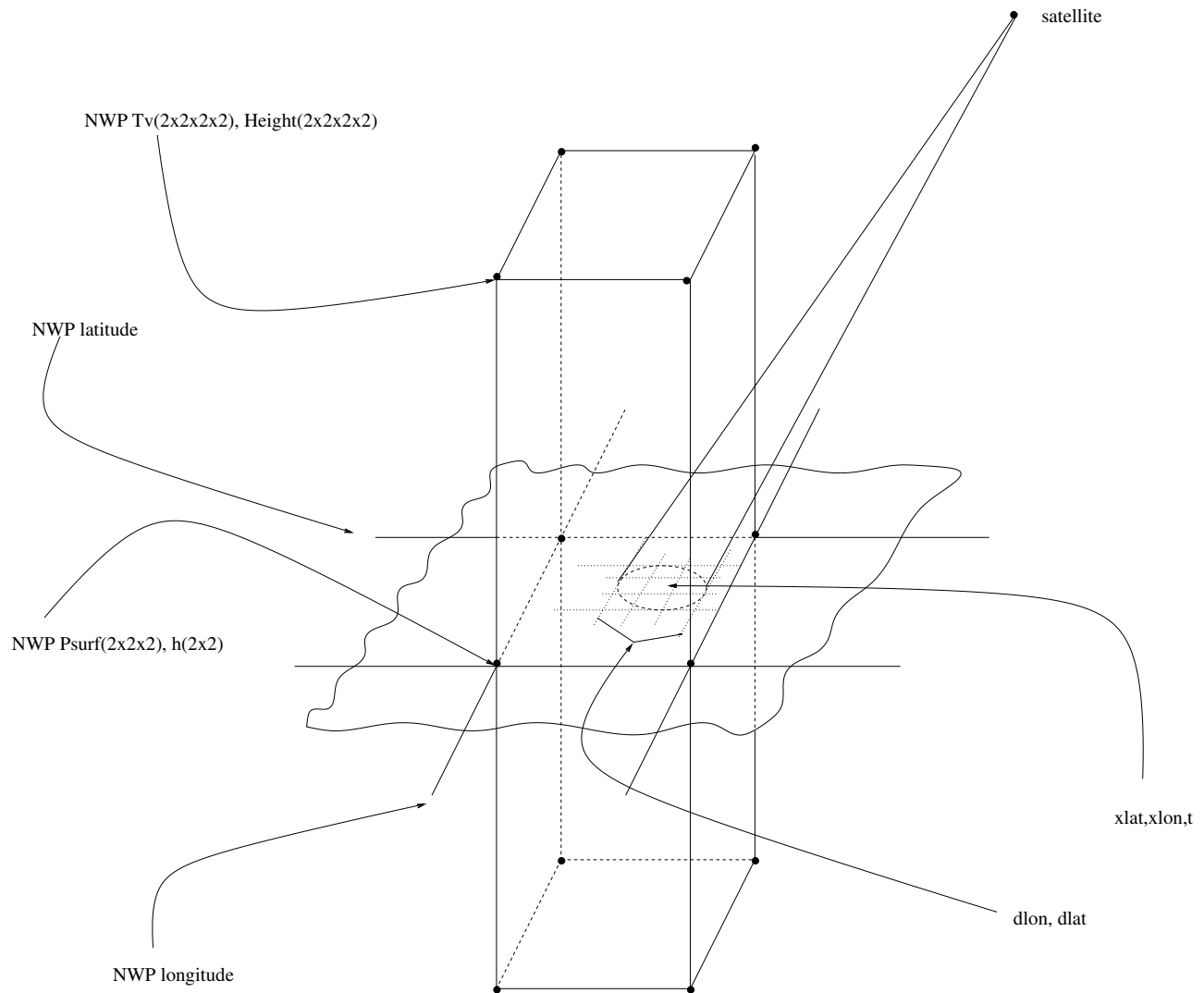


Figure 7-1: NWP Data needed to Compute Surface Pressure.

#### 7.4. Data Sources

The required meteorological data (inputs) come from either the NWP model outputs (if available) or from a monthly averaged database. The operational meteorological inputs should be a past (prior to the satellite acquisition) analysis field and a forecast field. An alternative solution could be two forecast fields surrounding the time of the satellite acquisition.

The selection between operational NWP or climatological data is supposed to be done outside the module. The topography database should be sampled at a space resolution (in latitude and longitude)  $dlat_i$  and  $dlon_i$  such as  $dlat_i \leq dlat_m / 2$  and  $dlon_i \leq dlon_m / 2$ .

### 7.5. Particular Cases Handling

Several particular cases can occur:

- If during the satellite swath, the time of acquisition crosses the  $\Delta t_{nwp}$  period and the inputs have not been refreshed, the module will make an extrapolation for all the times falling outside the range  $[t_{nwp(i)}, t_{nwp(i+1)}]$ .
- An assumption has been made here, that the footprint of the satellite is smaller in size than the NWP model grid size. In other words, we suppose that  $dlat_m \leq \Delta Lat_{nwp}$  and that  $dlon_m \leq \Delta Lon_{nwp}$ .

If this is not the case, a degradation of the NWP model resolution must be done before using this module. This degradation should be done to fit approximately the satellite footprint size so that  $dlon_m \leq \Delta Lon_{nwp}$  and  $dlat_m \leq \Delta Lat_{nwp}$ .

### 7.6. Possible Improvement

Instead of storing a high-resolution topography database containing the height only, one could also/instead store the difference between the individual heights and the mean NWP height. The mean NWP topography would have to be processed off-line with the high-resolution topography. This will accelerate the processing of the hydrostatic equation. This will also reduce the number of inputs as we will not need the *Href* input anymore. The down side of this improvement is that the module will be less agile. Each time the NWP topography or the high-resolution topography are modified, the *dZ* database will have to be processed again.

## 8. APPENDIX 3: SURFACE EMISSIVITY MODELING

### 8.1. Emissivity Modeling Approach

Realistic surface emissivity spectra are required for development and testing of the retrieval algorithms. As explained below, surface emissivity data from Prigent were used to avoid various limitations inherent in surface emissivity parameterization models. Namely, existing models do not fit some naturally observed spectra and have difficulty reproducing global and seasonal variability without arbitrary assumptions regarding composition and physical characteristics (e.g., topography, roughness, and vegetation cover) of natural surfaces (or a mixture of surface types) at the CMIS spatial resolution.

While the Prigent approach provided very useful data for treatment of surface emissivity for CMIS algorithm development, the databases used during the initial algorithm testing will be updated using data from SSMIS. Further, many refinements are expected after the launch of CMIS due to excellent co-location with CrIS (high accuracy moisture and temperature sounding) and VIIRS (land surface temperature and cloud-clearing). These updates will use the techniques described in the following sections. In the operational computing environment, these database updates will occur off-line.

### 8.2. Initial Emissivity Datasets

Realistic emissivity spectra are required for the estimation of the CMIS atmospheric and LST retrieval algorithms uncertainties over land. To obtain these surface emissivity datasets, we started from two datasets of derived emissivity values obtained from C. Prigent.

*Dataset 1:* The dataset is described in Prigent *et al.* [Prigent *et al.*, 1997]. Prigent derived SSM/I emissivities (19V, 19H, 22V, 37V, 37H, 85V, 85H GHz) as monthly means of clear sky cases using ISCCP LST (from AVHRR, assuming IR emissivity = 1) and TOVS atmospheric temperature and humidity. The Meteosat coverage area was used (Africa, Middle East, most of Europe). March, July, October, and December were analyzed. The fixed map projection of the ISCCP Meteosat product was used (25 km spacing) yielding about 37,000 map points per month. Emissivity retrieval errors are probably worse than 1% with higher errors at 22 and 85 GHz.

*Dataset 2:* The dataset is described in Prigent *et al.* [Prigent *et al.*, 1998]. Prigent derived SSM/I emissivities (19V, 19H, 22V, 37V, 37H, 85V, and 85H GHz) as monthly means of clear sky cases using ISCCP LST (from AVHRR, assuming IR emissivity = 1) and NCEP analyzed

atmospheric temperature and humidity profiles. Global land and polar ocean (> 50N/S latitude) emissivities are provided. July and October, 1992 are available to date. (Note that Prigent [1998] discusses October 91 data.) Monthly standard deviation mode values (most commonly occurring) range from 0.008 (19 and 37 GHz) to 0.017 (22 and 85 GHz) in the October 91 data.

The SSM/I emissivities have been inter/extrapolated to the following standard frequencies (in GHz, with V and H polarization):

6.0000 6.5645 7.1820 7.8577 8.5969 9.4057 10.2906 11.2587 12.3179 13.4767  
 14.7446 16.1317 17.6494 19.3098 21.1264 23.1139 25.2884 27.6675 30.2704 33.1182  
 36.2339 39.6427 43.3722 47.4525 51.9167 56.8009 62.1447 67.9911 74.3875  
 81.3857 89.0423 97.4192 106.5842 116.6114 127.5819 139.5845 152.7163 167.0835  
 182.8024 200.0000

### 8.3. Extrapolation Method

#### 8.3.1. Extrapolation Method Approach and Description

The extrapolation methods are described. The point of creating this dataset was to create a plausible emissivity universe with as stressing as, or more stressing situations than the real world, in order to test our algorithms.

Frequencies from 19-37 GHz and 37-85 GHz are found by interpolation with noise added by the following formulas:

$$\text{noise}(19_X < f < 37_X) = -0.4 * \text{diff}(1937_X) * |\text{rand}| * (f - 19) * \frac{(37 - f)}{(37 - 19)^2} \quad (54)$$

$$\text{noise}(37_X < f < 85_X) = -0.4 * \text{diff}(3785_X) * |\text{rand}| * (f - 37) * \frac{(85 - f)}{(85 - 37)^2} \quad (55)$$

where X stands for V or H,  $\text{curve} = \text{sign}(\text{grad}3785_X - \text{grad}1937_X)$ , rand is a normally distributed random number with zero mean and variance one, and  $\text{diff\_f1\_f2}_X = e(f2) - e(f1)$ . The original 22V data was thrown out because of high noise and the desire to have consistency between the 23.5V and 23.5H data. The absolute value of rand and curve are used to force the 37-85 second derivative to have the same sign as the 19-85 GHz curvature. The 19-37 second derivative always has the same sign as the gradient. The noise scales with the emissivity difference

because phenomenon with small gradients may also have less spectral variability. Note that one rand value is used for all interpolations in the same set including V and H polarizations.

To extrapolate to frequencies above 85 GHz, the 37 to 85 GHz gradient was used as a starting point:

$$\text{grad3785}_x = \frac{85_x - 37_x}{85 - 37} \quad (56)$$

When extrapolating, it is possible that emissivities may exceed 1. Note however that the Prigent datasets have many emissivities greater than 1. For example, the number of cases exceeding 1 in the Oct-92 set was:

19V	19H	22V	37V	37H	85V	85H
9957	31	5086	440	1	30	6

The extrapolation was reduced by a frequency-dependent factor designed to limit unrealistic or unphysical emissivity values using:

$$\begin{aligned} &\text{if } (\text{grad3785}_x \geq 0) \\ &\quad e(85_x < f < 200_x) = 85_x + \text{grad3785}_x * (f - 85.5) * \frac{(\text{emax} - 85_x) * (85 - 37)}{(\text{emax} - 37_x) * (200 - 85)} \\ &\text{if } (\text{grad3785}_x < 0) \\ &\quad e(85_v < f < 200V) = 85_v + \text{grad3785}_v * (f - 85.5) * \frac{(85_v - \text{emin}_v) * (85 - 37)}{(37V - \text{emin}_v) * (200 - 85)} \\ &\quad e(85_H < f < 200H) = 85_H + \text{grad3785}_H * (f - 85.5) * \frac{(85_H - \text{emin}_H) * (85 - 37)}{(37H - \text{emin}_H) * (200 - 85)} \end{aligned} \quad (57)$$

The constants  $\text{emin}_v = 0.55$  and  $\text{emin}_H = 0.25$  are the minimum 37 and 85 GHz, V and H pol. emissivities from the October 1991 set ( $\text{emin}^X$ ). Emax is the highest emissivity retrieved in the Prigent set (about 1.05).

Added noise was designed to be a function of emissivity and frequency. A maximum noise of 0.1 at 200 GHz and minimum emissivity was added. The added noise drops to zero at  $e=1$  or  $f=85$ :

$$\text{noise}(85_x < f < 200_x) = 0.1 * \text{rand} * \frac{(1 - e(f))}{(1 - e_{\min_x})} * \frac{(f - 85)}{(200 - 85)} \quad (58)$$

Note that one rand value is used for all interpolations in the same set including V and H pol.

To extrapolate to frequencies below 19 GHz, the 19 to 37 GHz gradient was used:

$$\text{grad1937}_x = \frac{37_x - 19_x}{37 - 19} \quad (59)$$

$$e(6_x < f < 19_x) = 19_x + \text{grad1937}_x * (f - 19.35) * [C_x(1) + (C_x(2) - C_x(1)) * (f - 6)/(19 - 6)] \quad (60)$$

where  $C_x = [0.5 \ 0.75]$  for negative  $\text{grad1937}_x$  and  $[0.75 \ 1]$  for positive  $\text{grad1937}_x$ . We set  $C_x$  to lower values for scattering spectra to account for more flattening of the curve expected below 19 GHz.  $C_x(1)$  is less than  $C_x(2)$  to allow the spectrum to become flatter closer to 6 GHz.

Added noise was given by:

$$\text{noise}(6_x < f < 19_x) = 0.021 * |\text{rand}| * \frac{(1 - e(f))}{(1 - e_{\min_x})} * \frac{(19 - f)}{(19 - 6)} \quad (61)$$

Added noise was designed to be a function of emissivity and frequency. A maximum noise of 0.02 at 6 GHz and minimum emissivity was added. The added noise drops to zero at  $e=1$  or  $f=19$ .

Note that one rand value is used for all interpolations in the same set including V and H pol.

The final quality control logic sets to 1.0 all emissivity values which are greater than 1, all emissivities which are less than  $e_{\min_x}$  to  $e_{\min_x}$ , and sets  $e_H = e_V$  where  $e_H > e_V$  due to noise addition or errors in the Prigent set.

### 8.3.2. Extrapolation Method Validation

The mean and standard deviation of a set of 1000 emissivities, after the emissivities were translated to the CMIS channels, are shown in Figure 8-1. The mean emissivity at V-polarization is higher than for H-polarization. The H-polarization emissivities in these test data are significantly more variable than the V-polarization emissivities, as can be seen from the standard deviation plot. Without the random perturbations, the standard deviations would dip to lower values where interpolations were made around 23 GHz and 50 GHz. The lack of such dips and the tendency of the standard deviations to trend upward on the high and low ends are

indications that the extrapolation/interpolation methods used conservative assumptions (pessimistic for retrieval performance).

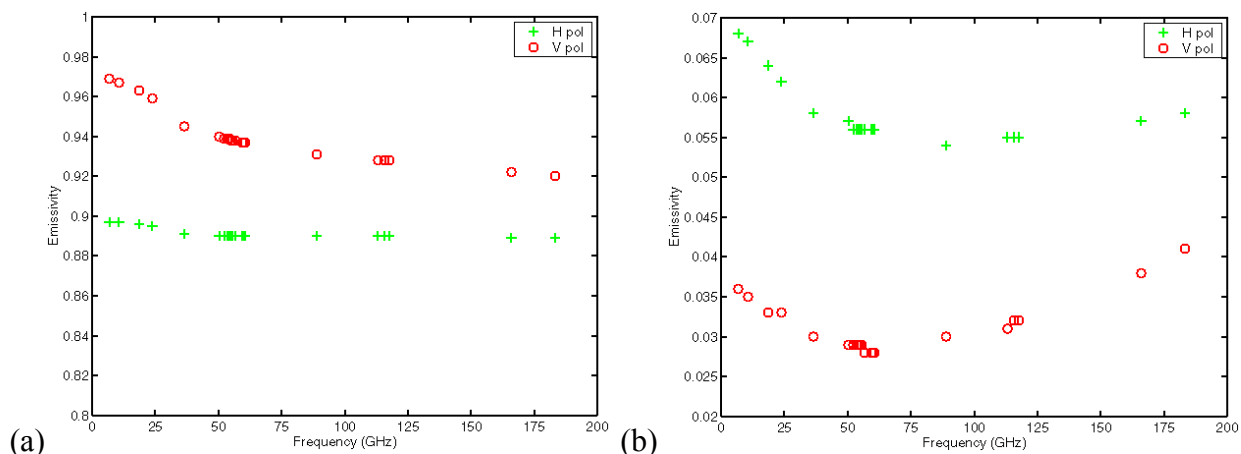


Figure 8-1: MeanFigure 8-2 (a) and standard deviation (b) of surface emissivity values at CMIS channel frequencies.

To determine whether or not the interpolations/extrapolations assume an unrealistic correlation, Figure 8-3 shows the correlation of each channel emissivity with a reference frequency. The two references are 18 and 36 GHz. The input Prigent data are at 18, 36 and 89 GHz. If an appropriate amount of randomization was applied to the interpolated values at 23 and 50 GHz, the correlations should decrease smoothly through these frequencies. This is shown in Figure 8-3, indicating that the simulations do not assume an unrealistic correlation.

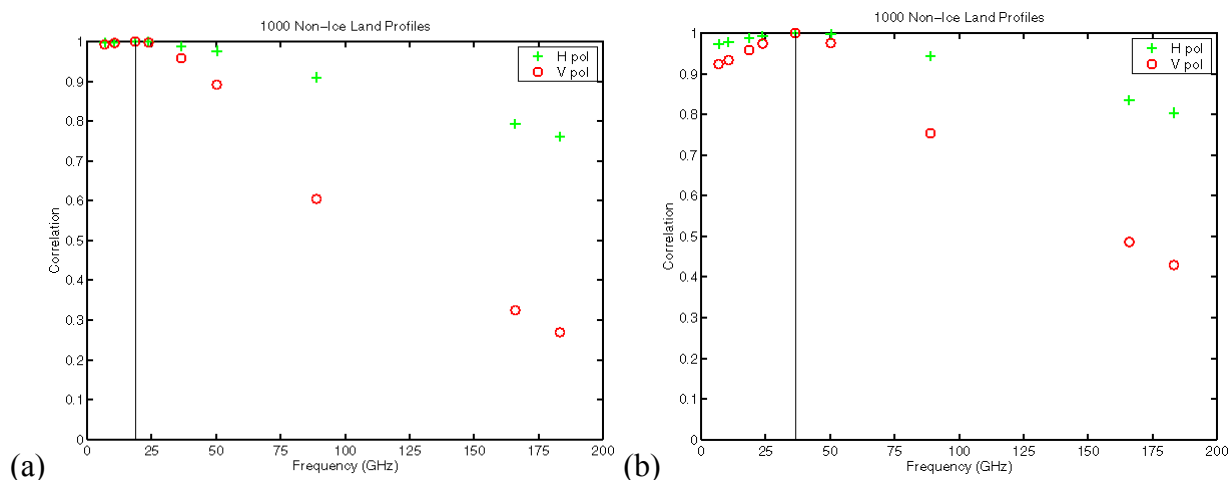


Figure 8-3: Correlation of each channel emissivity with a reference frequency of (a) 18 GHz and (b) 36 GHz.

## **9. APPENDIX 4: IMPACT OF DYNAMIC EMISSIVITY ON CORE MODULE RETRIEVALS**

### **9.1. Purpose**

We have investigated the impact to the core module retrievals from using time-averaged emissivities. The idea is to perform retrievals over a period of time using a background and covariance based on climatology. A new background and covariance may then be generated from the retrieved emissivities, and this is used in the retrieval for the subsequent time-step. The intent is that the averaged emissivity will converge after a short period of time to a value with a small bias relative to the true emissivity, and that the covariance will be small enough to constrain the retrieval close to the truth. A better first guess and tighter constraint should result in an improvement in our ability to retrieve the other surface and atmospheric parameters.

### **9.2. Simulations and Results**

We have tested this approach in simulations using both NOAA-88 profiles and NWP fields. The input emissivity values are taken from the Prigent/Rossow data set of monthly averaged emissivities for SSM/I channels (see more details about these datasets in Appendix 1 and Appendix 3). Since we are applying this to a CMIS configuration, the missing emissivities were generated by extrapolation and interpolation as discussed in Appendix 3. In this report we present results when applied to a 9-day period for NWP fields.

The NWP fields were taken from models run for 1-9 October 1995. We used 176 grid points located in eastern U.S. and Canada. The fields only go up to 300 mb for relative humidity and 70mb for temperature. Also, the vertical resolution is coarser than required input to the core module. Thus, interpolation and extrapolation were required to obtain the core module 40-level grid from 1000 mb to 0.1 mb. For temperature, the extrapolation was based upon a regression which was generated from climatology data. For water vapor, we extended the mixing ratio using the (pressure ratio)<sup>3</sup> decay rate down to a value of 0.003 g/kg, and from there a constant value. Further, what was being reported for the skin temperature differed in many cases from the lowest layer temperature by much more than climatology, so we divided that difference by 4 to get a more reasonable skin temperature. (See also [EN #61](#) response.)

An example of the final temperature and mixing ratio profiles and difference between skin temperature and lowest layer temperature for the first 16 time-steps are shown in Figure 9-1. The profiles are for the grid point (40.0,-77.5).



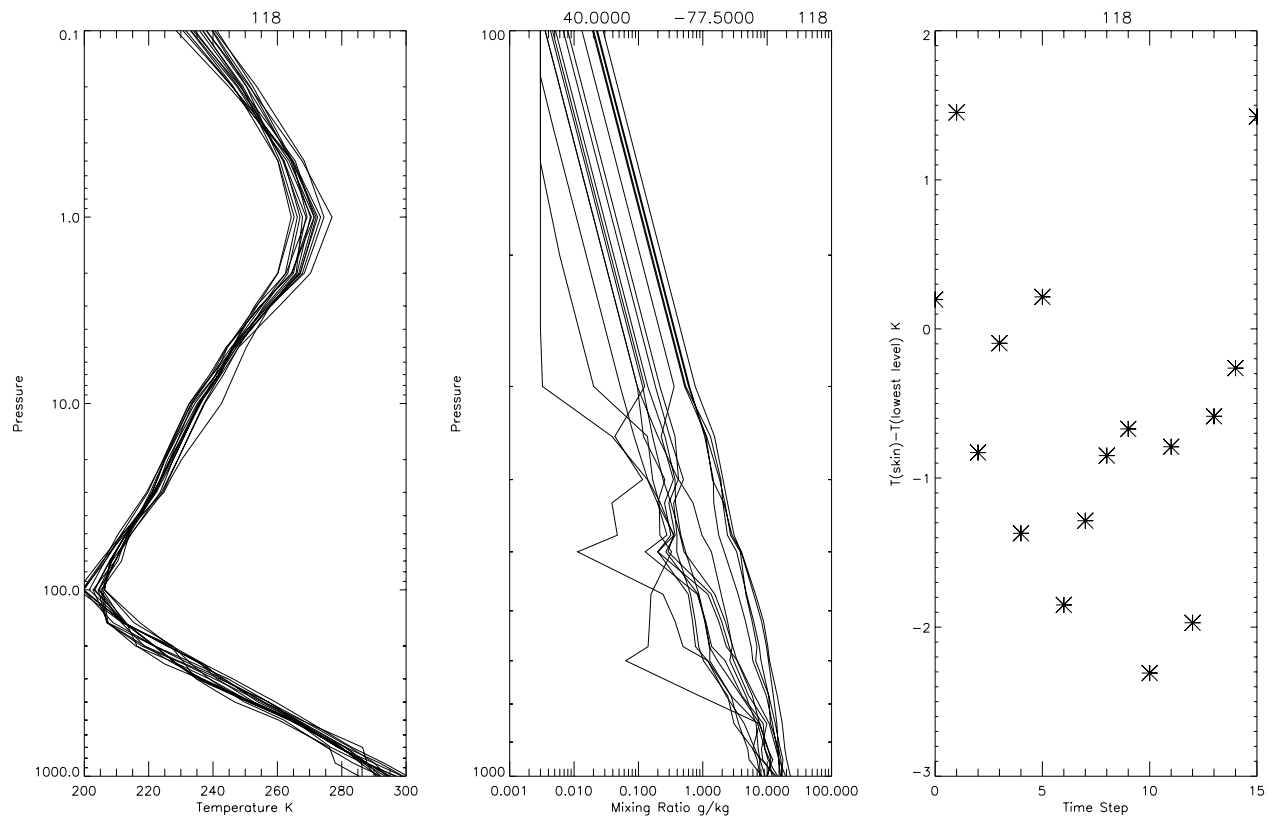


Figure 9-1: NWP temperature and mixing ratio profiles and skin and surface air temperature difference for grid point (40.0, -77.5). Eight days at times 0Z and 12Z.

The above profiles were fed into the OSS forward model to generate the radiance, to which the sensor noise was added. The noise was varied for each time-step. The resultant radiance was used as the input for the core module. The core module retrieves temperature and mixing ratio profiles, emissivity profiles for 12 distinct channels, skin temperature and cloud liquid water. The retrieved emissivity for the 16 times-steps were then averaged. Figure 9-2 shows the retrieved emissivity and the time-averaged emissivity for 10 surface channels for the grid point (40.0, -77.5). In Figure 9-3 we present the *rms* and Bias of the difference between retrieved and true over the 176 grid points.

Figure 9-2 shows the variation in the instantaneous retrieved emissivity and the convergence of the time-averaged for an individual grid point. The variations with time increase as the atmospheric contribution to the channel radiance increases (as frequency increases from 10 to 89 GHz). It can be seen from Figure 9-3 that these patterns hold in general. The *rms* of the difference between the time-averaged values and the truth varies from 0.0025 for 10V to 0.01 for 89H. By comparing the first column with the second it can be seen that the time-averaged is typically closer to the true value than the instantaneous retrieval.

## APPENDIX 4: IMPACT OF DYNAMIC EMISSIVITY ON CORE MODULE RETRIEVALS

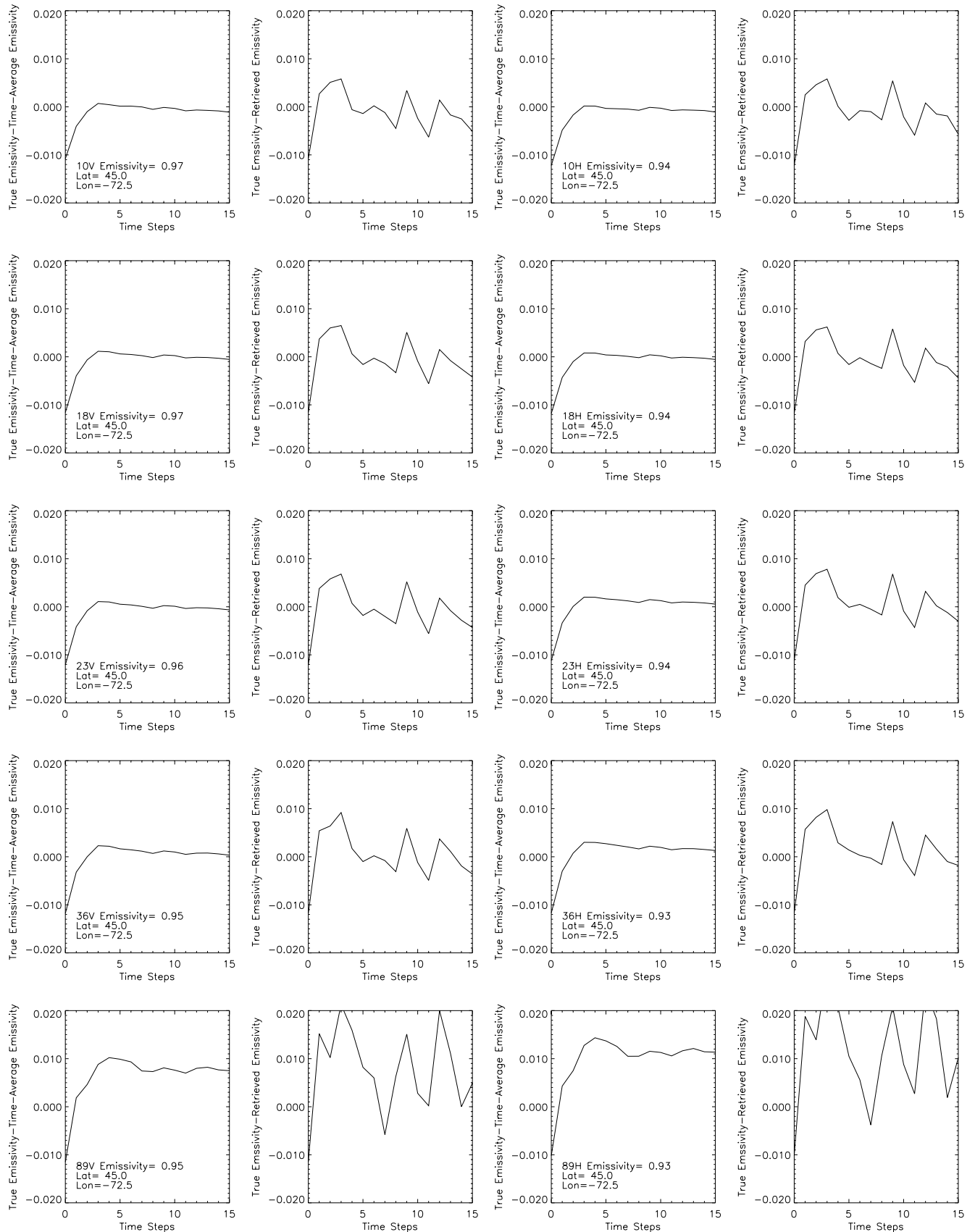


Figure 9-2: Difference at each time step between 1) cumulative time-averaged and true emissivities and 2) retrieved and true emissivities. Results for the surface channels 10V, 10H, 18V, 18H, 23V, 23H, 36V, 36H, 89V, and 89H for the grid point at (40.0,-77.5)

## APPENDIX 4: IMPACT OF DYNAMIC EMISSIVITY ON CORE MODULE RETRIEVALS

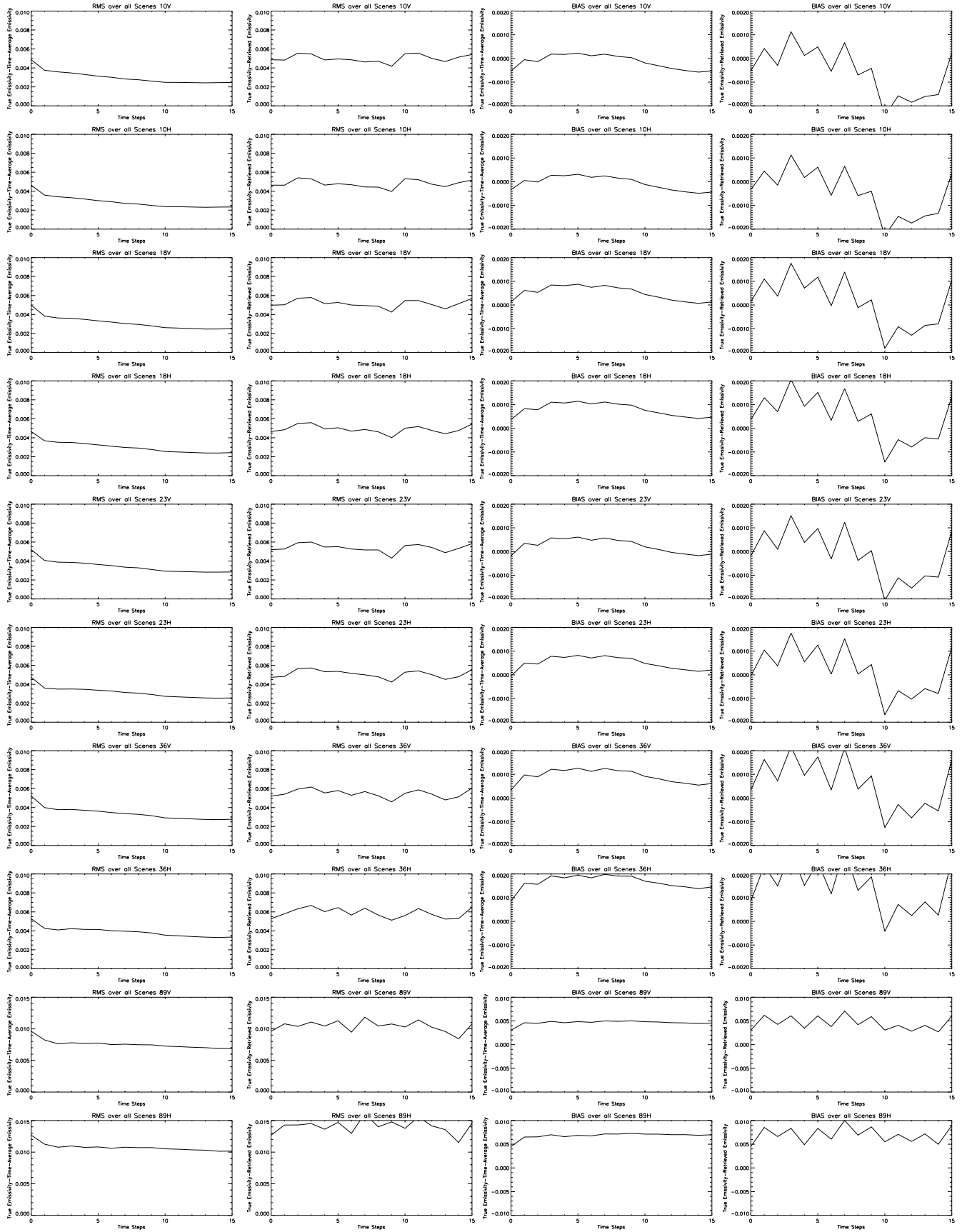


Figure 9-3: The *rms* and bias over 176 grid points of the difference between 1) time-averaged and true and 2) retrieved and true. Results for the 10 surface channels.

The goal of developing a means of dynamic emissivity calculation is to generate a more representative background and tighter covariance for the emissivity, thus improving our retrieval capabilities of the other parameters. It was shown above that emissivities can be generated which are, on average, closer to the truth. In this section we examine the effect of using the new background and covariance in a retrieval. The experiment went as follows. For the 16 times we performed retrievals as described above. The retrieved emissivity values were averaged and an associated background and covariance matrix was generated for each grid point. Then, for time-step 17, two separate retrievals were performed. The first retrieval was like the other 16 while the other used the time-averaged background and covariance. In Figure 9-4 we show the retrieved, truth, and the difference, for skin temperature, TPW, and the emissivity at 23GHz H-pol for the first scenario, i.e. climatology background. The overall *rms* error for skin temperature and TPW were 1.4 K and 2.7 kg/m<sup>2</sup> respectively.

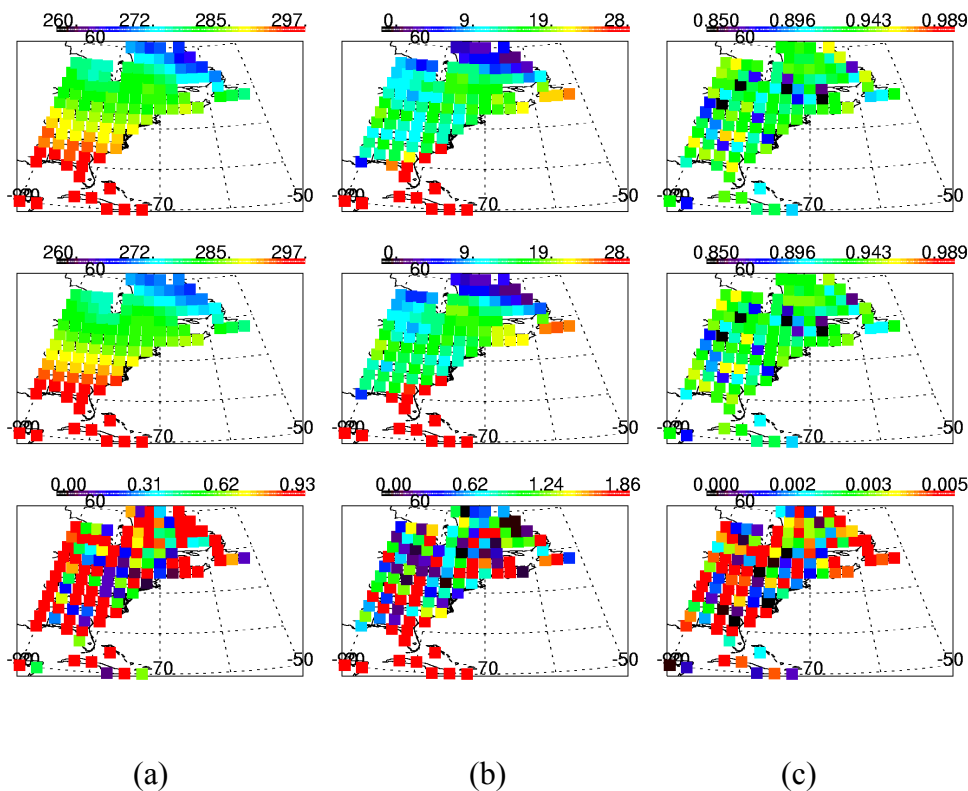


Figure 9-4: climatology background case. Retrieved, true and true minus retrieved. Row (1) is the retrieved, row (2) is the true and row (3) is the difference. Column (a) is skin temperature, (b) is TPW and (c) is 23GHz H-pol emissivity.

In Figure 9-5, the results using the time-averaged background and covariance are presented. The *rms* error on skin temperature and TPW are reduced to 0.75 K and 2.09 kg/m<sup>2</sup> respectively. By

comparing Figure 9-4 and Figure 9-5 we see that the emissivity error has decreased also. It can also be seen from Figure 9-6 that the *rms* error of the retrieved temperature and mixing ratio profiles also decrease.

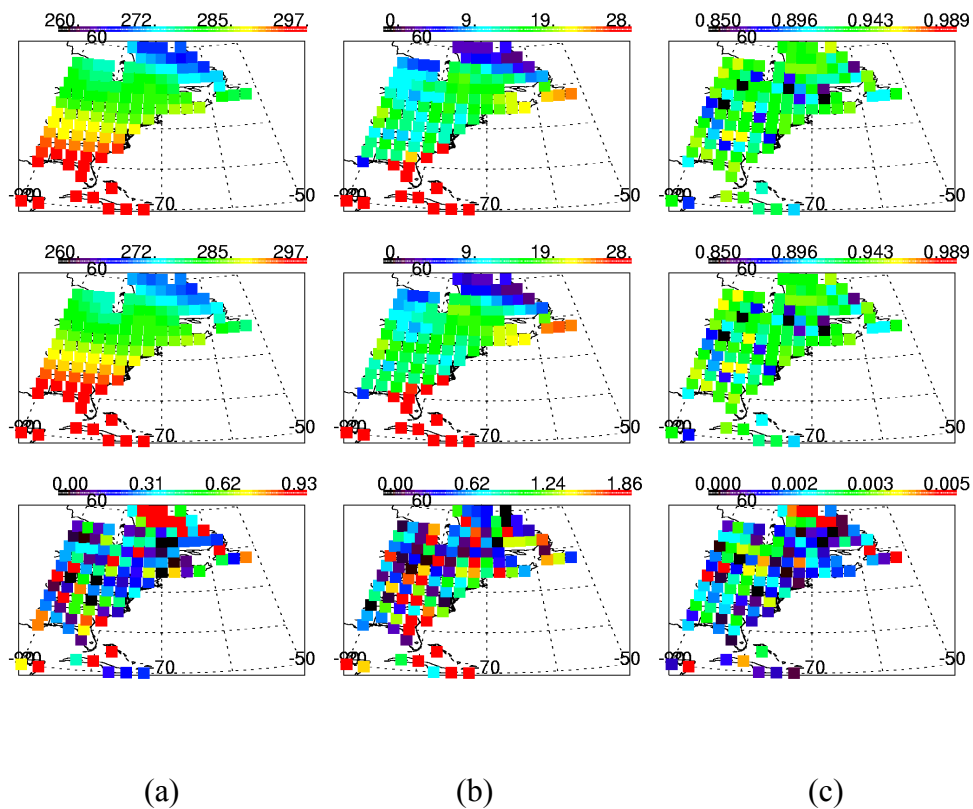


Figure 9-5: Same as Figure 9-4 but with time-averaged background and covariance.

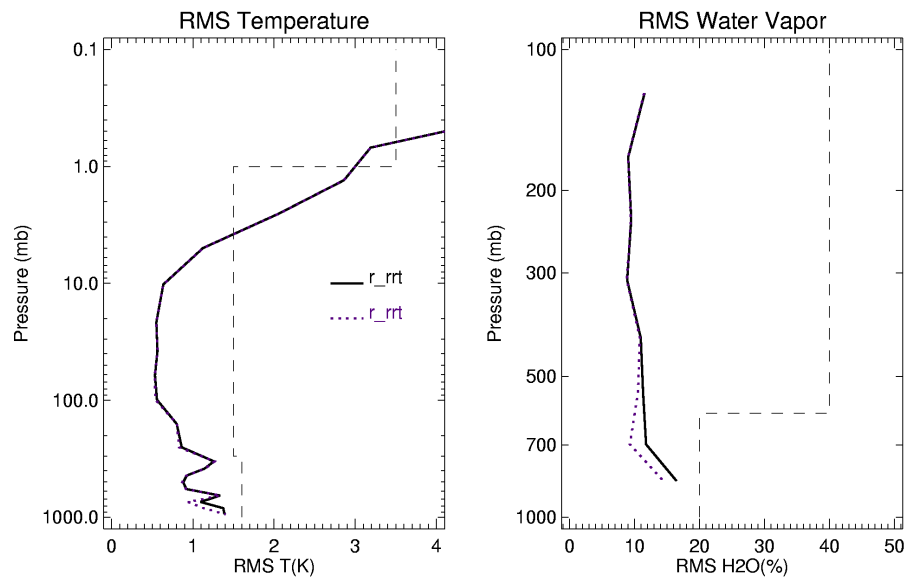


Figure 9-6: The *rms* error of temperature and mixing ratio profiles for the 176 NWP grid points. Solid line, climatology background and covariance. Dashed line, time-averaged background and covariance.

### 9.3. Summary

We have performed a set of core module retrievals of various atmospheric and surface parameters on simulated radiances based upon NWP fields. For these retrievals the initial guess and covariance were based upon climatology. The retrieved values of surface emissivity were averaged over an eight-day, two-observations-per-day-period. For day nine we used both climatology background and covariance and time-averaged background and covariance. There was a significant improvement in the retrieval of the surface parameters and the lower atmosphere temperature and mixing ratio.

The above retrievals were all performed retrieving both water vapor profiles and cloud liquid water. We repeated the retrievals without retrieving CLW, i.e., assuming clear sky conditions. Figure 9-7 and Figure 9-8 are the same as Figure 9-2 and Figure 9-3, except for the assumption of clear sky conditions. By comparing Figure 9-8 and Figure 9-3 it can be seen that the *rms* error for both 89V and 89H decreases from about 0.1 to 0.004. Figure 9-7 shows that for the individual case shown in Figure 9-2, the 89V and 89H emissivity retrievals oscillate around zero in the assumed clear sky retrievals as opposed to oscillating around some bias in the assumed cloudy sky retrievals. The lower frequency channels behave the same for either retrieval assumptions.

The retrievals for time-step 17 were also repeated but with assumed clear sky conditions. This was done for both climatology and time-averaged background and covariance. For the climatology case the *rms* for skin temperature and TPW are 1.4 K and 1.96 kg/m<sup>2</sup> respectively. For the time-averaged case the *rms* values are 0.8 K and 1.54 kg/m<sup>2</sup> respectively. Figure 9-9 and Figure 9-10 are the same as Figure 9-4 and Figure 9-5.

# APPENDIX 4: IMPACT OF DYNAMIC EMISSIVITY ON CORE MODULE RETRIEVALS

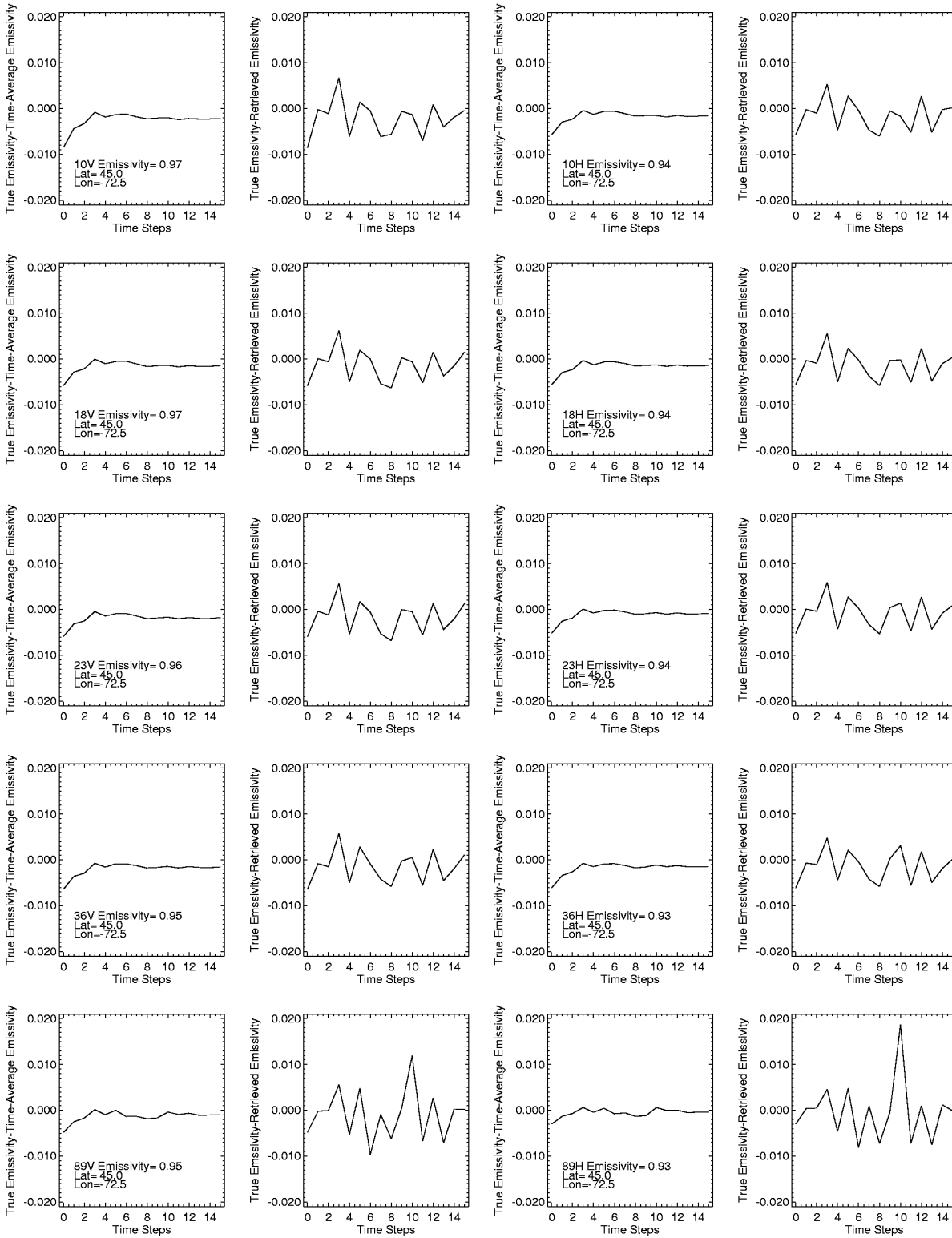


Figure 9-7: Same as Figure 9-2 except assumed clear sky conditions.



## APPENDIX 4: IMPACT OF DYNAMIC EMISSIVITY ON CORE MODULE RETRIEVALS

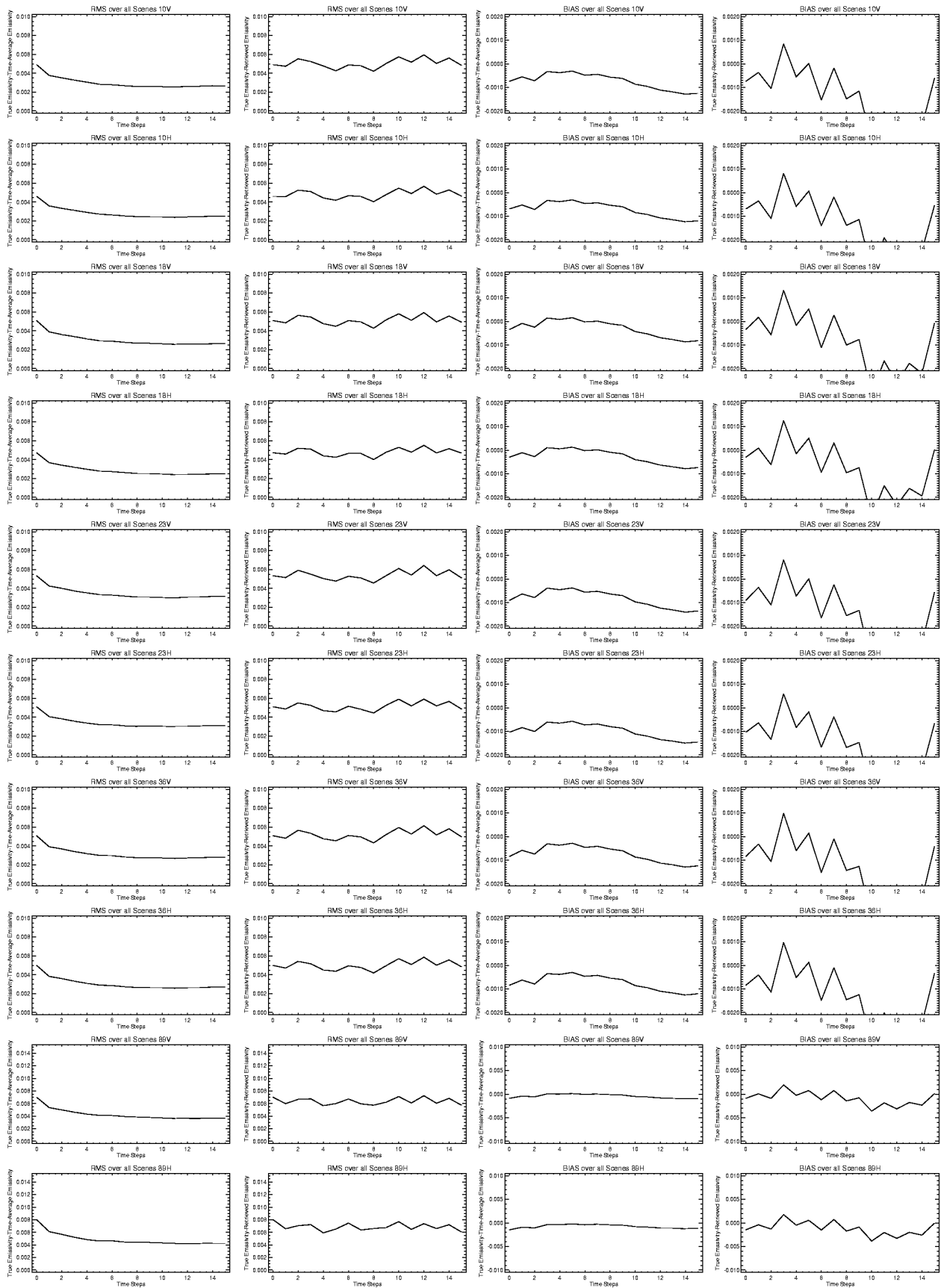


Figure 9-8: Same as Figure 9-3 except assumed clear sky conditions.

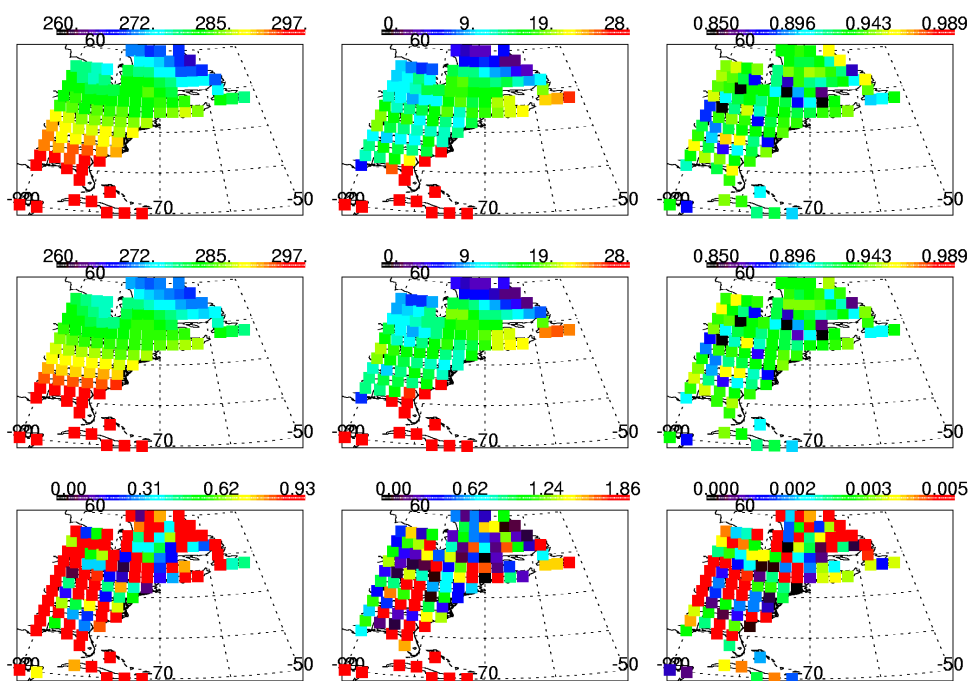


Figure 9-9: Same as Figure 9-4 except assumed clear sky conditions.

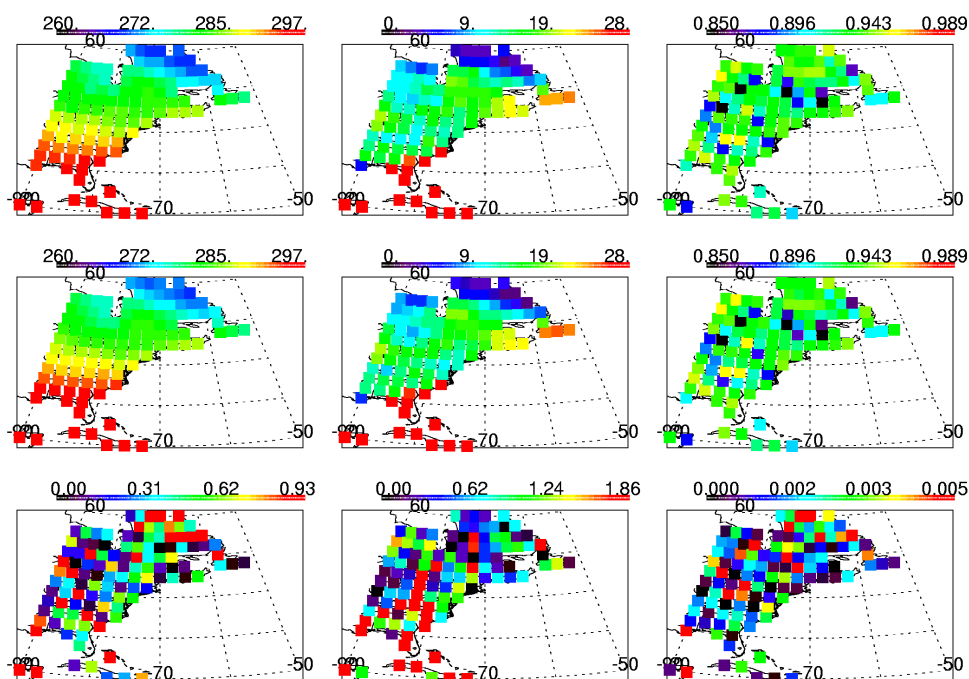


Figure 9-10: Same as Figure 9-5 except assumed clear sky conditions.

## 10. APPENDIX 5: IMPACT OF AN AIR MASS CLASSIFICATION ON CORE MODULE RETRIEVALS.

### 10.1. Overview

The purpose of this study is to show the impact of an air-mass pre-classification on the core physical inversion retrievals.

The study begins by showing how the TIGR-2 (Thermodynamic Initial Guess Retrieval) dataset (and therefore any dataset) can be classified from simulated CMIS brightness temperatures. Refer to Achard [Achard, 1991] and Aires [Aires, 1994] for all the details on this dataset and its air-mass classification. Probabilistic Neural Networks (PNN) can be used for this purpose. This classification method is based on the measure of the distance (transformed into probabilities) between the inputs and the actual weights of the network. It contains a competitive layer that selects the class according to the highest probability criterion. The weights have the dimension of the number of elements of the training set.

Then we classified the NOAA-88 dataset in the same manner and performed retrievals to make performance comparisons using a global covariance matrix, and pre-classified covariance matrices.

### 10.2. Air Mass Classification of the TIGR-2 Dataset using a PNN

#### 10.2.1. Network Architecture

##### *Inputs*

The inputs of the classifier are CMIS brightness temperatures. Using the whole CMIS channel set is not optimal. The channels affected by the surface and the clouds prevent the classification from being robust. Several instrumental configurations have been tested and only 3 channels in the oxygen absorption band have been chosen. The inputs of the PNN classifier are the 3 CMIS brightness temperatures at 54.905, 55.490, and 56.660 GHz.

##### *Outputs*

The outputs of the network are 5 air mass classes (polar1, polar2, midlat1, midlat2 and tropical air classes from the TIGR-2 air mass classification scheme, as described in Achard, 1991).

### 10.2.2. Training and Validation

The TIGR-2 dataset (containing 1761 situations represented by their temperature and water vapor profiles and separated into 5 classes) is used to create a training and a validation dataset for the PNN classifier.

The training dataset consists of these 1761 classified situations for which we have simulated the 3 CMIS brightness temperatures mentioned above using clear sky and a constant class emissivity over land (class#7).

The validation dataset consists of these same 1761 situations for which we have simulated the same 3 CMIS channels, but this time for cloudy cases (randomly generated clouds) and randomly selected land classes between 1 and 16.

### 10.2.3. Results

Figure 10-1 shows the training classification (top figures) and the validation results (bottom figures). The thick blue horizontal lines show the true classification (previously done at LMD from the temperature and moisture profiles, as explained in Achard [Achard, 1991]), and the thin red horizontal lines show our results for the dataset classification from the selected 3 CMIS channels. This PNN is a robust method for air mass classification. The 5 classes can be well discriminated with this PNN using only 3 of the 50 GHz channels. These channels are not sensitive neither to the surface, nor to the clouds, which makes the robustness of the method (the results are independent from the fact that the training may have been done on cloudy or on clear cases).

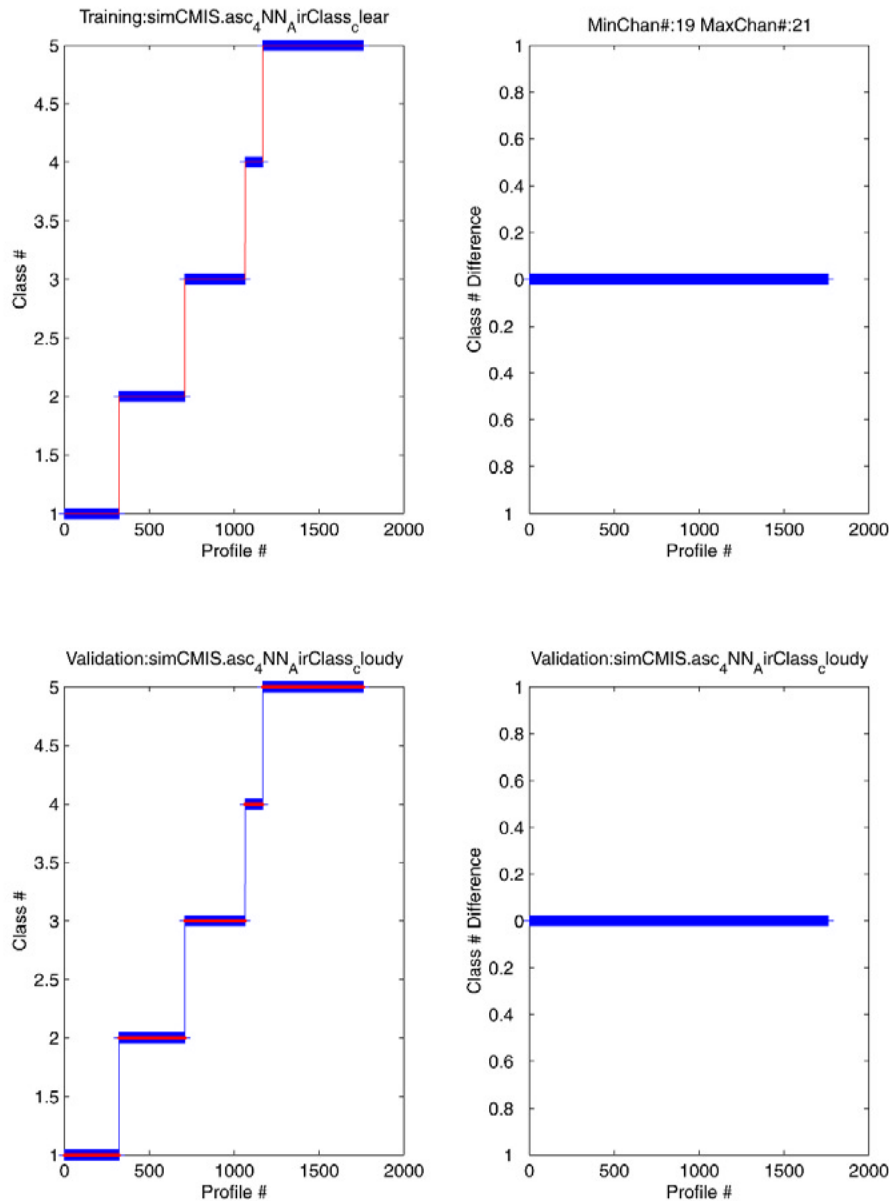


Figure 10-1: TIGR-2 Classification Results.

### 10.3. Impact of Air-Mass Pre-Classification on Core Module Retrievals

The atmosphere and skin temperature data were divided into five subsets (classes) in order to compose five backgrounds and associated covariance matrices. The classification was performed by a probabilistic neural network classifier. The network was trained on a set of profiles from the TIGR dataset that had been separated at LMD (Laboratoire de Météorologie Dynamique) into five classes (polar1, polar2, midlat1, midlat2 and tropical). We matched each profile with a set of emissivities randomly selected from the land cases of the inter/extrapolated

July and October Prigent profiles (see dataset description in Appendix 3). Clouds were also applied to the profiles in a random manner. The training brightness temperatures were derived from the profiles by computing CMIS brightness temperatures and adding noise corresponding to a 50-km spatial resolution. We found that a set of three of the 50-GHz-band channels was sufficient to correctly classify all the TIGR profiles, when an independent set of noise realizations were used as test cases. When the neural network was tested on NOAA-88 data, we found that four channels (centered at 54.380, 54.905, 55.490, and 56.660 GHz) were required to ensure that every classified NOAA-88 profile was fully consistent with the population in the respective TIGR class. This four-channel set includes channels that are primarily sensitive to the lower stratosphere and upper troposphere and excludes surface-sensitive channels. The set can therefore be used with the neural network to classify CMIS SDR data by air mass type without regard to the geographic location (water, land, coast, etc.).

Retrieval experiments were performed to assess the impact on Core Module results of pre-classifying cases according to air mass. Retrievals made with a global background were compared with retrievals made with the classified background. The global/classified distinction refers to the water vapor profile, the temperature profile, and the surface temperature. The surface emissivities in these experiments were assumed to be correctly classified as ocean, unfrozen land, or ice/snow. The retrievals were made with noise corresponding to a 50-km horizontal spatial resolution. Each profile was classified by executing the neural to the noisy brightness temperatures. Retrieval performance comparisons are shown in Figure 10-2, Figure 10-3 and Figure 10-4 separately for ocean, unfrozen land, and frozen land environments, for cloudy conditions. In these plots, the profile errors are for point-value (not vertically averaged) results.

The primary benefit of the classification was, as expected, to reduce the temperature profile retrieval errors near the tropopause. Even though the classification used only temperature-sounding channels sensitive near the tropopause, the classification benefited profile retrieval performance near the surface. The classification was also beneficial or neutral for retrieving surface temperature, cloud liquid, and precipitable water (Table 10-1).

Table 10-1: Comparison of performance for retrieval variables for global and classified airmass.

	Tsfc (K)		CLW kg/m <sup>2</sup>		PW <sub>v</sub> kg/m <sup>2</sup>	
	Global	Class.	Global	Class.	Global	Class.
Ocean	0.91	0.89	0.010	0.008	0.17	0.16
Land	1.71	1.72	0.15	0.14	3.01	2.69
Ice	2.25	2.19	0.04	0.04	0.68	0.64

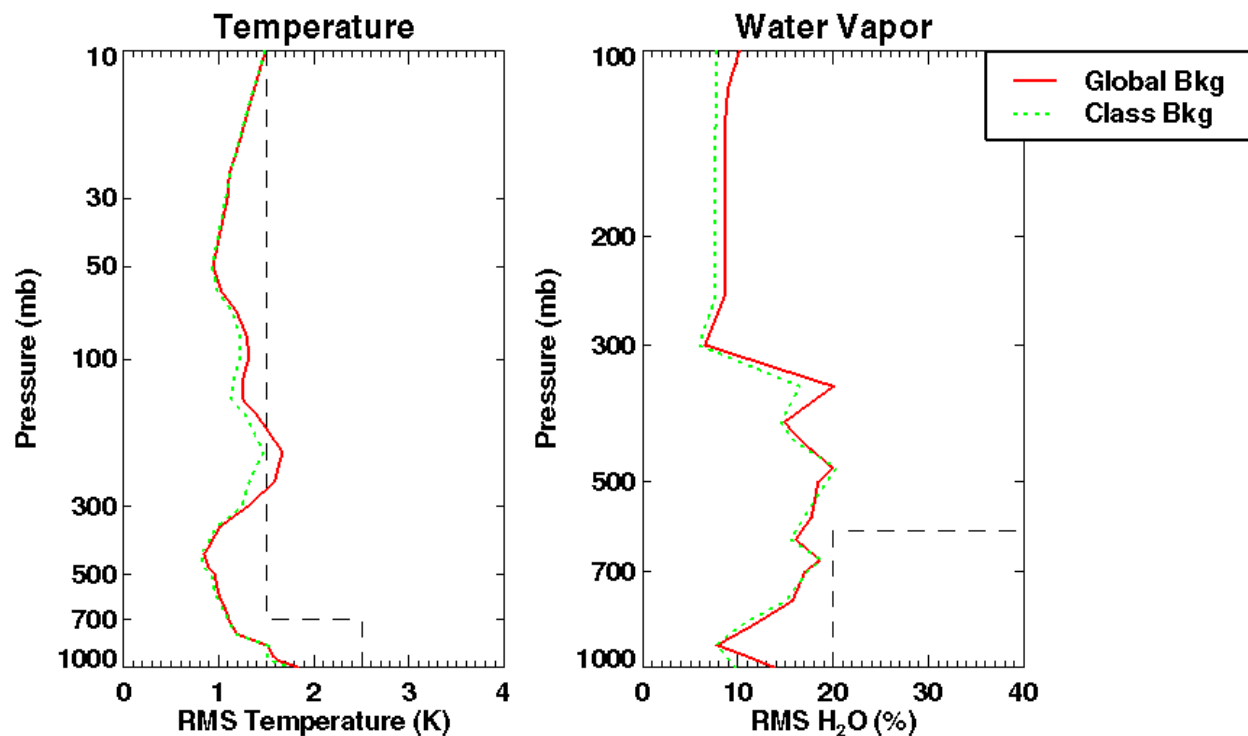


Figure 10-2: Ocean - Comparison of performance for retrieval variables for global and classified air mass.

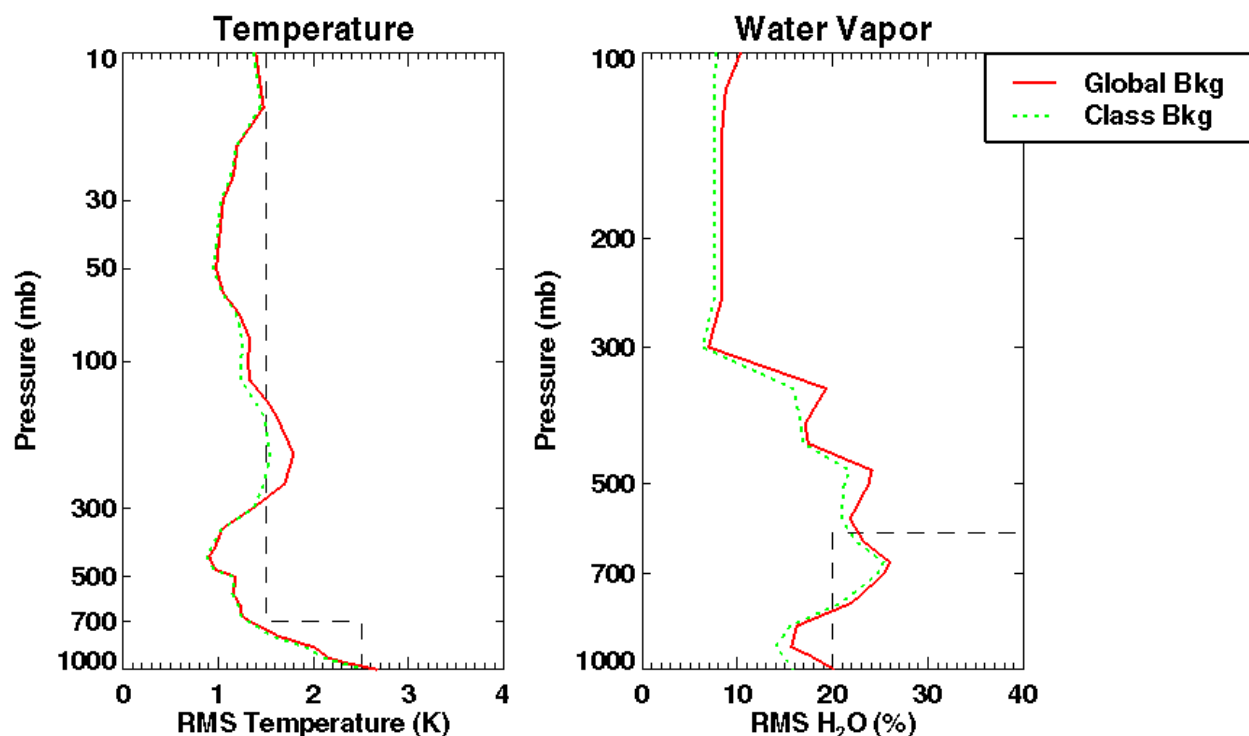


Figure 10-3: Land - Comparison of performance for retrieval variables for global and classified air mass.

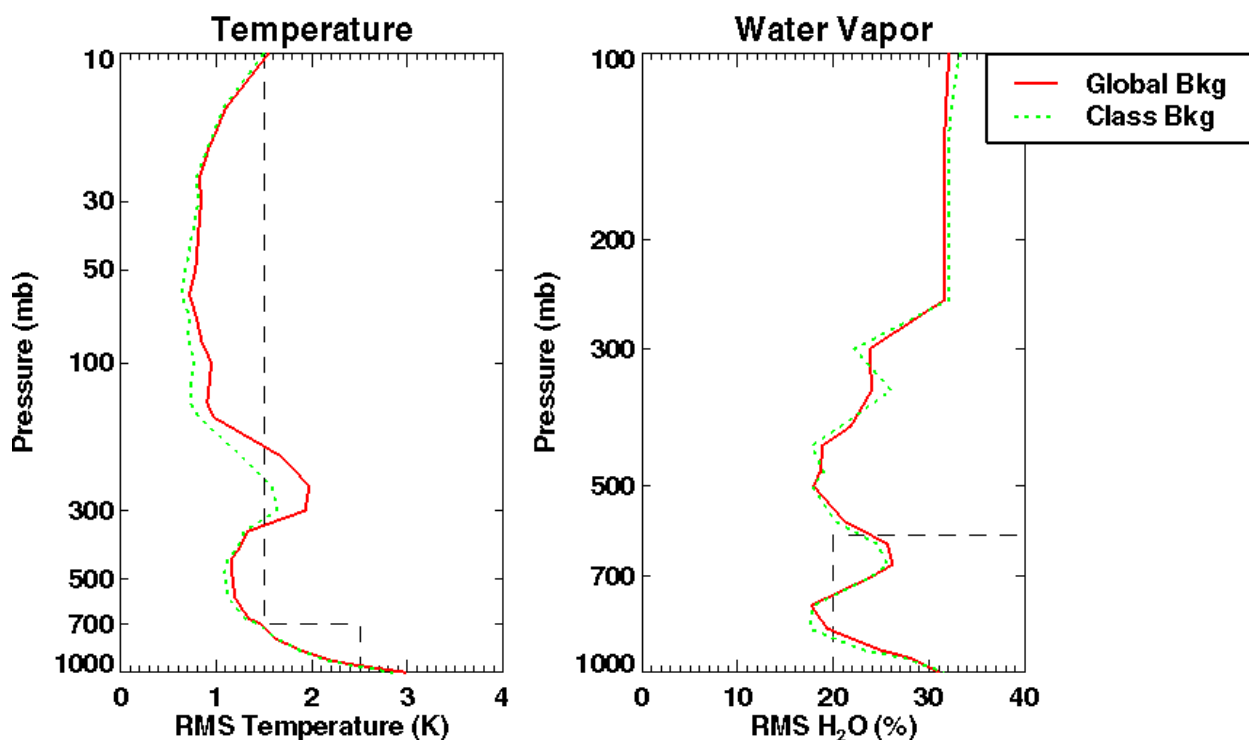


Figure 10-4: Ice - Comparison of performance for retrieval variables for global and classified air mass.



## 11. APPENDIX 6: IMPACT OF SURFACE EMISSIVITY CLASSIFICATION ON CORE MODULE RETRIEVALS

### 11.1. Overview

A variety of surface classification methods have been developed, some of which are discussed in the Vegetation/Surface Type ATBD (Vol. 11). There is considerable radiometric ambiguity among some of the types. For pre-classification for the Core Module, it is not necessary to identify a specific surface type, but to identify the emissivity characteristics most important to core module function.

The retrieval performance for several core module output parameters is highly dependent on the surface emissivity, as is shown in the main section of this volume and in the ATBD volumes for Water Vapor (Vol. 3), Cloud Liquid Water (Vol. 7, Part 2), and Atmospheric Vertical Temperature Profile (Vol. 4). The key aspect of the emissivity is its value at 18/23-GHz in horizontal polarization, as well as the degree to which that emissivity is known prior to retrieval and is available to constrain the retrieval. Retrieval performance is most challenged for cases with high 18/23-GHz-H emissivity (surfaces with moderate or dense vegetation) and it is those cases where performance is most sensitive to prior knowledge of the emissivity.

The Core Module surface pre-classifier focuses on identifying conditions with high 18/23-GHz-H emissivity. One reason for that focus is that it targets the classification to the cases where it can provide the greatest performance benefit. Another reason is system robustness. Any land scene not identified as having high 18/23-GHz-H emissivity has the “global” emissivity background constraint applied. The global background includes a broad variety of land surfaces, including wet land and high emissivity cases. By including high-emissivity cases in the global background, any high-emissivity retrieval scenes that the high-emissivity tests do not detect will still use an acceptable background and will have acceptable retrieval performance. No attempt is made to pre-classify other surface types, such as scattering surfaces (desert, snow). There would be a substantial risk that a precipitating scene would be misclassified as a scattering surface, causing the Core Module to converge to an erroneous solution rather than throwing a quality control flag that indicates possible precipitation contamination.

### 11.2. Classification algorithm

The first step is a test for low emissivity in the 18/23 GHz region, such as would occur with open water:

$$T_{23H} - T_{18H} > A,$$

where  $T_X$  is the brightness temperature in channel  $X$  and  $A$  is a threshold value determined from

$$A = \begin{cases} A_1 & \text{if } T_{18V} < T_{C1} \\ A_2 & \text{if } T_{18V} > T_{C2} \\ A_1 + (T_{18V} - T_{C1}) \frac{(A_2 - A_1)}{(T_{C2} - T_{C1})} & \text{otherwise} \end{cases}$$

and  $A_1=0$ ,  $A_2=2$ ,  $T_{C1}=250$ , and  $T_{C2}=270$ . This test was derived from the standing water test Neale et al. (1990) applied to SSM/I. The first change was to use horizontal polarization rather than vertical, with horizontal being available on CMIS (unlike SSM/I) and being far more sensitive to water. The second change was to set a staged threshold that depends on the 18-GHz-V channel. That dependence is used to account for cold, dry atmospheres where  $T_{23H} - T_{18H}$  tends to be smaller than for moister scenes, for a given surface emissivity.

The second test checks for a scattering signature (Ferraro, et al., 1996)

$$\max[(T_{23V} - T_{89V}), (T_{18V} - T_{37V})] > 6,$$

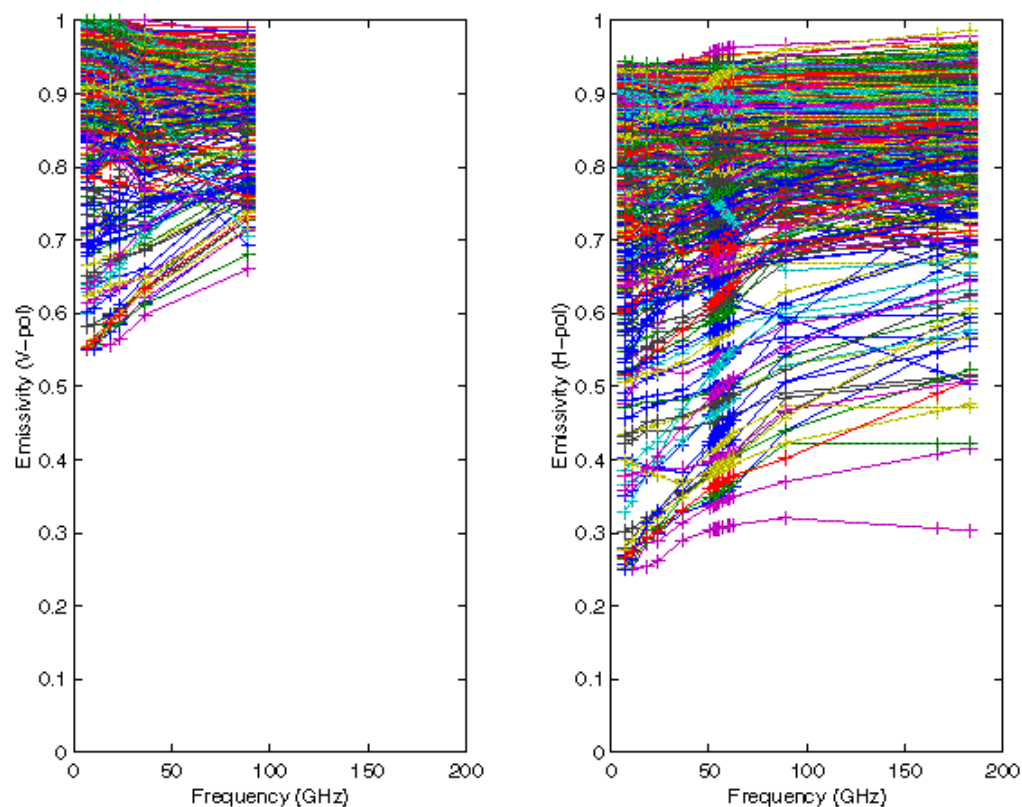
tuned for CMIS.

If neither test is passed, the scene is classified as high-emissivity.

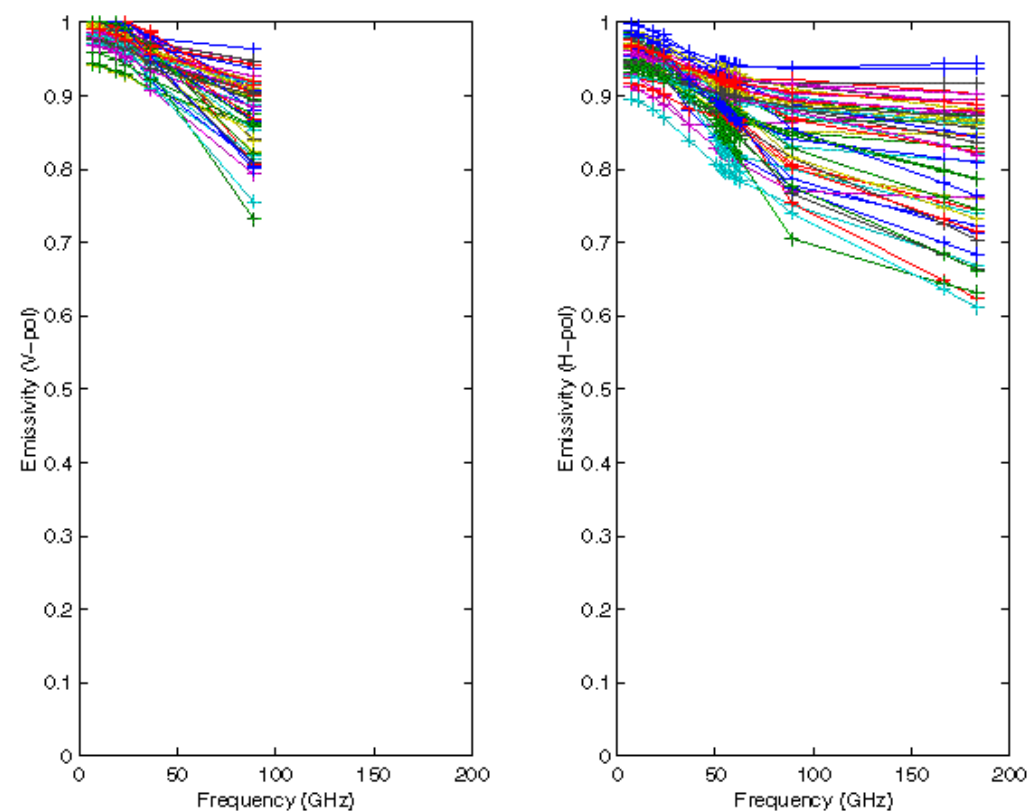
### 11.3. Background statistics generation

The background emissivity statistics for the high-emissivity surface class were generated by applying the classification algorithm to a set of scenes. The scenes were generated by randomly selecting 1200 emissivity spectra from our Prigent-derived emissivity database. Each spectrum was matched with 40 atmospheric profiles, for a total of 4800 scenes. Brightness temperatures were computed for each scene, with sensor noise simulated. For each of the 1200 spectra, the classifier was run on each of the 40 scenes, and if 20 or more of them tripped the low emissivity test, the spectrum was set aside as a low-emissivity case. If 20 or more of the 40 scenes tripped the scattering test, the spectrum was set aside as a scattering case. Otherwise, it was included in the set of high-emissivity cases from which the background statistics were derived. The 1200 spectra classified this way are plotted in Figure 11-1. From the plots it is clear that the test was successful at passing only high-emissivity cases into the set used to generate those background statistics. While a substantial number of high-emissivity cases were screened with the low-emissivity scenes, it is better to err on the side of failing to misclassify a high-emissivity scene as a “global” case than to misclassify a low-emissivity scene as having a high emissivity.

## a. Low H-polarization cases



## b. Scattering cases



## c. High H-polarization cases

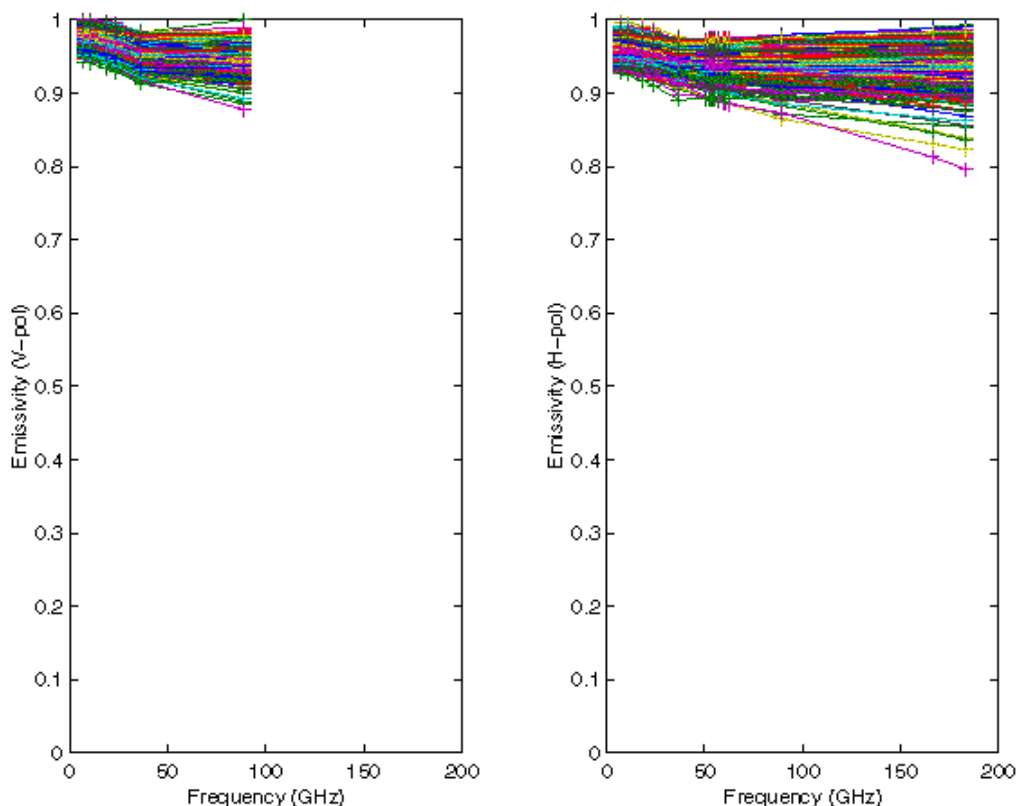


Figure 11-1: Emissivity spectra for the cases classified for developing the high-emissivity background statistics. The spectra cover the CMIS channel set, and were plotted before the baseline sounding channel set was converted from H to V polarization.

#### 11.4. Impact of pre-classification on retrieval performance

The impact of the emissivity pre-classification can be seen most clearly when it is applied to a set of cases for which many have high 18/23-GHz-H emissivity. The impact was tested with a set of scenes corresponding to mixed forest, which fits that description. In those cases, the algorithm classified about half of them as high-emissivity. All the cases, regardless of classification, were included in the performance impact analysis. The tests demonstrated a large beneficial impact for water vapor profile retrieval of the classification (Figure 11-2). Likewise retrieval errors were reduced by factors of 33%, 25%, and 37%, respectively, for precipitable water, cloud liquid water, and land surface temperature.

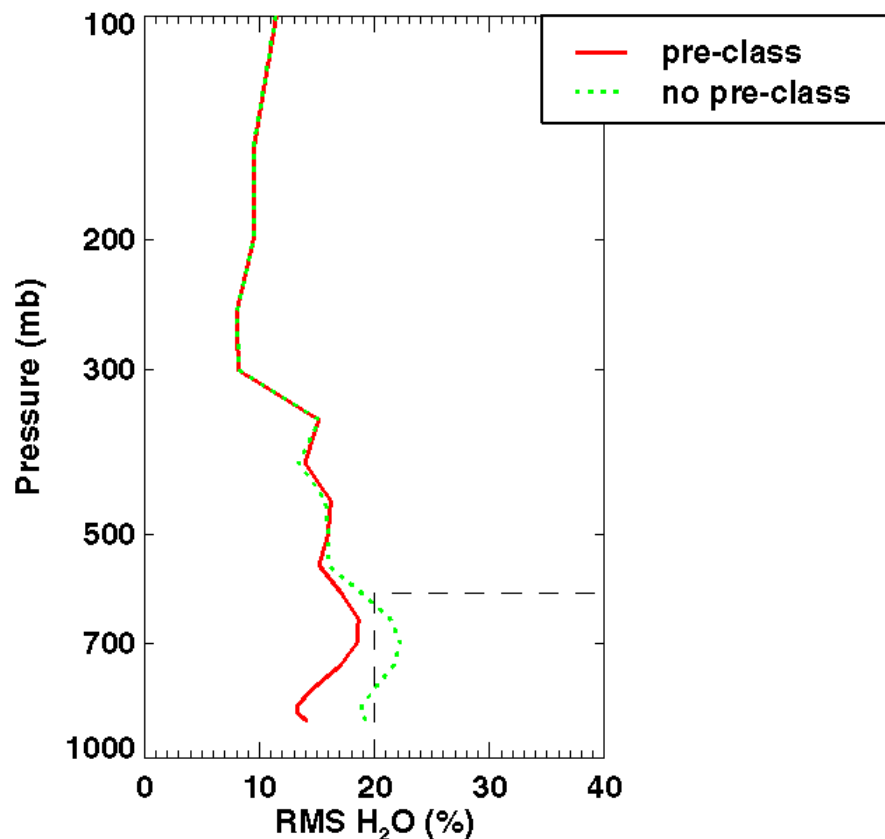


Figure 11-2: Water vapor profile retrieval error for mixed forest surface type with and without surface emissivity pre-classification. The retrievals were performed with noise representative of a composite field of view size of 50 km, and the errors were then inflated 5% to account for error increase in the cascade from 50 to 15 km. The scenes were cloudy, with liquid water randomly (uniform distribution) ranging from 0 to 0.25 kg/m<sup>2</sup>.

## REFERENCES

Abramowitz, M., and Stegun, I., Handbook of Mathematical Functions, National Bureau of Standards, Applied Mathematics, series 55. Abramowitz and Stegun Editions, **18(55)**, pp 878-901, 1968.

Achard, V., 3 problèmes clé de l'analyse 3D de la structure thermodynamique de l'atmosphère: mesure du contenu en ozone; classification des masses d'air; modélisation "hyper" rapide du transfert radiative, *Pd-D Thesis, Paris VII University, France*, (Available from LMD, Ecole Polytechnique, 91 128 Palaiseau Cedex, France).  
1991.

Aerojet, Software user's manual for the SSMIS, **Volume 1, Report 9467**, 1994.

Aires, F., Classification en masse d'air par réseaux neuronaux, *Technical Report, LMD, France*, (Available from LMD, Ecole Polytechnique, 91 128 Palaiseau Cedex, France), 1994.

Backus, G.E., and Gilbert, J.F., Uniqueness in the inversion of inaccurate gross Earth data, *Philos. Trans. R. Soc. London A*, **266**, pp 123-192, 1970.

Benediktsson, J.A., Neural network approaches versus statistical methods in classification of multisource remote sensing data, *IEEE Transactions on Geoscience and Remote Sensing*, **28(4)**, pp 541-552, July 1990.

Cabrera-Mercader, C., and Staelin, D., Passive microwave relative humidity retrievals using feedforward neural networks, *IEEE Trans. Geoscience. and Remote Sensing*, **33(6)**, pp 1324-1328, 1995.

Chahine, M. T. and Susskind J., Fundamentals of the GLA physical retrieval method, *Report on the Joint ECMWF/EUMETSAT Workshop on the Use of Satellite Data in Operational Weather Prediction: 1989-1993*, **Vol. 1**, pp 271-300, T. Hollingsworth Editor, 1989.

Chedin, A., Scott N.A., Wahiche C., and Moulinier P., The Improved Initialisation Inversion (3I) method: A high resolution physical method for temperature retrievals from the TIROS-N series, *J. Clim. Appl. Meteor.*, **24**, pp 128-143, 1985.

Clough, S.A., Kneizys, F.X., and Davies, R.W., Line shape and the water vapor continuum, *Atmos. Res.*, **23**, pp 229-241, 1989.

Clough, S.A., Iacono, M.J., and Moncet, J.-L., Line-by-line calculation of atmospheric fluxes and cooling rates: Application to water vapor, *J. Geophys. Res.*, **97**, pp 15761-15785, 1992.

ECMWF Scientific Advisory Committee, Verification statistics and evaluations of ECMWF products, ECMWF/SAC/29/(00)3a, Reading, England, 1 September 2000.

English, S. J., Estimation of temperature and humidity profile information from microwave radiances over different surface types, *J. of Applied Meteorology*, **38**, pp 1526-1541, 1999.

## REFERENCES

- Escobar, J., Base de données pour la restitution de paramètres atmosphériques à l'échelle globale; Etude sur l'inversion par réseaux de neurones des données des sondeurs verticaux atmosphériques satellitaires présents et à venir, *PhD University of Paris VII*, France, February 1993 (Available from LMD, Ecole Polytechnique, 91 128 Palaiseau Cedex, France).
- Eyre, J.R., Inversion of cloudy satellite sounding radiances by nonlinear optimal estimation: Theory and simulations for TOVS and application to TOVS data, *Quart. J. Roy. Meteor. Soc.*, **115**, pp 1001–1037, 1989a.
- Eyre, J. R., Inversion of cloudy satellite sounding radiances by nonlinear optimal estimation. II: Application to TOVS data. *Q. J. R. Meteorol. Soc.*, **115**, pp 1027-1037, 1989b.
- Eyre, J. R., The information content of data from satellite sounding systems: A simulation study, *Q. J. R. Meteorol. Soc.*, **116**, pp 401-434, 1990.
- Ferraro, R. R., F. Weng, N. C. Grody, and A. Basist, An eight-year (1987-1994) time series of rainfall, clouds, water vapor, snow cover, and sea ice derived from SSM/I measurements, *Bull. Amer. Meteor. Soc.*, **77**, pp 891-905. 1996.
- Fleming, H.E. and McMillin, L.M, Atmospheric transmittance of an absorbing gas 2. *Applied Optics*, **16**:1366, 1977.
- Fleming, H.E., Goldberg, M.D., and Crosby, D.S., Minimum variance simultaneous retrieval of temperature and water vapor from radiance measurements, *Proc. Second Conference on Satellite Meteorology, Williamsburg, Amer. Met. Soc.*, pp 20-23, 1986.
- Gill, E.G., Murray, W., and Wright, M.H., Practical Optimization, *Academic, San Diego, California*, 1981.
- Halem, M., Ghil, M., Atlas, R., Susskind, J., Quirk, W , The GISS sounding temperature impact test, *NASA Tech. Memo. 78063*: 2.9-2.82, 1978.
- Houghton, J.T., Taylor, F.W., and Rodgers, C.D., Remote Sounding of Atmospheres, *Cambridge Planetary Science Series, Cambridge University Press*, 1984.
- Isaacs, R.G., Unified Retrieval Methodology for the DMSP Meteorological Sensors, *RSRM' 87 Advances in Remote Sensing Retrieval Methods*, pp 203-214, Deepak, Fleming and Theon Editors, 1987.
- Isaacs, R. G., Hoffman, R. N., and Kaplan, L. D., Satellite remote sensing of meteorological parameters for global numerical weather prediction, *Rev. of Geophys.*, **24(4)**, pp 701-743, 1986.
- Klein and Swift, 1977
- Kohn and T. Wilheit, 1995.
- Lee J., Weger, R.C., Sengupta, S.K., Welch, R.M., A neural network approach to cloud classification, *IEEE Transactions on Geoscience and Remote Sensing*, **28(5)**, pp 847-855, July 1990.

## REFERENCES

- Levenberg, K., A method for the solution of certain problems in least squares, *Q. Appl. Math.*, **2**, pp 164-168, 1944.
- Liebe, H.J., Hufford, G.A., and Manabe, T., A model for the complex permittivity of water at frequencies below 1 THz. *Intern. J. Infrared Millimeter Waves*, **12**, pp 659–675, 1991.
- McMillin, L. M., Fleming, H.E., Atmospheric transmittance of an absorbing gas: a computationally fast and accurate transmittance model for absorbing gases with constant mixing ratios in inhomogeneous atmospheres, *Applied Optics*, **15 (2)**, pp 358-363, 1976.
- McMillin, L. M., Fleming, H.E., Atmospheric transmittance of an absorbing gas. 2: a computationally fast and accurate transmittance model for slant paths at different zenith angles, *Applied Optics*, **16 (5)**, pp 1366-1370, 1977.
- McMillin, L. M., Fleming, H.E. and Hill, M.L., Atmospheric transmittance of an absorbing gas. 3: a computationally fast and accurate transmittance model for absorbing gases with variable mixing ratios, *Applied Optics*, **18 (10)**, pp 1600-1606, 1979.
- McMillin, L. M., Cone, L.J., Goldberg, M.D., and Kleespies, T.J., Atmospheric transmittance of an absorbing gas. 4, *Applied Optics*, **34:6274**, 1995.
- McMillin, L. M., Cone, L.J., and Kleespies, T.J., Atmospheric transmittance of an absorbing gas. 5, *Applied Optics*, **34:8396**, 1995.
- Marks, C.J. and Rodgers, C.D., A retrieval method of atmospheric composition from limb emission measurements, *J. Geophys. Res.*, **98**, pp 14939-14953, 1993.
- Marquardt, D., An algorithm for least squares estimation of nonlinear parameters, *SIAM J. Appl. Math.*, **11**, pp 431-441, 1963.
- Moncet, J.L. and Isaacs, R.G., Advanced Technical Applications for Satellite Microwave Water Vapor Retrievals, *PL-TR-92-2311, Final Report. Phillips Laboratory, Directorate of Geophysics, AFMC, Hanscom AFB, MA 01731-5000*, 1992.
- Moncet, J.-L., Isaacs, R.G., Hegarty, J.D., Unified Retrieval of Atmospheric temperature, Water Substance, and Surface Properties from the Combined DMSP Sensor Suite, *PL-TR-96-2067, Final Report. Phillips Laboratory, Directorate of Geophysics, AFMC, Hanscom AFB, MA 01731-5000*, 1996.
- Moulinier, P., Analyse statistique d'un vaste ensemble de situations atmospheriques sur l'ensemble du globe., LMD Internal Communication Number 123, 1983 (Available from LMD, Ecole Polytechnique, 91 128 Palaiseau Cedex, France).
- Neale, C. M. U., M. J. McFarland, and K. Chang, Land-surface-type classification using microwave brightness temperatures from the Special Sensor Microwave/Imager, , *IEEE Trans. Geoscience Remote Sensing*, **28**, pp 829-845, July 1990.
- Press, W.H., Teukolsky, S.A., Vetterling, W.T., Flannery, B.P., Numerical Recipes in C : The Art of Scientific Computing, *Cambridge University Press, Cambridge*, pp 681-689, 1992.



## REFERENCES

- Prigent, C., Rossow, W.B., and Matthews, E., Microwave land emissivities estimated from SSM/I observations, *J. Geophys. Res.*, **102**, pp 21867-21890, 1997.
- Prigent, C., Rossow, W.B., and Matthews, E., Global maps of microwave land surface emissivities: Potential for land surface characterization, *Radio Science*, **33**, pp 745-751, 1998.
- Prigent, C. and Rossow, W.B., Retrieval of surface and atmospheric parameters over land from SSM/I: Potential and limitations, *Q. J. R. Meteorol. Soc.*, **xxx**, pp xxx-xxx, 1999.
- Reuter, D., Susskind J., and Pursch A., First guess dependence of a physically based set of temperature-humidity retrievals from HIRS2/MSU data, *J. Atmos. Ocean. Tech.*, **5**, pp 70-83, 1988.
- Rieu, H., Escobar, J., Scott, N.A., Chedin, A., SSM/T Forward Modelling Using Neural Networks, *J. Quant. Spectrosc. Radiat. Transfer*, **56(6)**, pp 821-833, 1996.
- Rodgers, C.D., Retrieval of atmospheric temperature and composition from remote measurements of thermal radiation, *Rev. Geophys.*, **14**, pp 609–624, 1976.
- Rodgers, C.D., Characterization and error analysis of profiles retrieved from remote sounding measurements, *J. Geophys. Res.*, **95**, pp 5587-5595, 1990.
- Rosenkranz, P.W., Inversion of data from diffraction-limited multiwavelength remote sensors. 2. Nonlinear dependence of observables on the geophysical parameters, *Radio Science*, **17:1**, pp 245-456, 1982.
- Rosenkranz, P.W., A Rapid Atmospheric Transmittance Algorithm for Microwave Sounding Channels, *IEEE Trans. on Geo. and Remote Sensing*, **33(5)**, pp 1135-1140, 1995.
- Rosenkranz, P.W., Hutchinson, K.D., Hardy, K.R., and Davis M.S., An assessment of the impact of satellite microwave sounder incidence angle and scan geometry on the accuracy of atmospheric temperature profile retrievals, *J. Atmos. Ocean. Tech.*, **14**, pp 488–494, 1997.
- Rumelhart, D.E., Hinton, G., Williams R., Learning internal representation by error propagation. Parallel distributed processing exploring the micro-structure of cognition, *D.E. Rumelhart, J. McClelland Editors, MIT Press*, 1986.
- Scott, N. A., and Chedin A., A fast line by line method for atmospheric absorption computations: the Automated Atmospheric Absorption Atlas, 4A, *J. Appl. Meteor.*, **20**, pp 801-812, 1981.
- Smith, W. L., An improved method for calculating tropospheric temperature and moisture from satellite radiometer measurements. *Mon. Wea. Rev.*, **96**, pp 387-396, 1968.
- Smith, W. L., and Woolf, H. M., 1976: The Use of Eigenvectors of Statistical Covariances Matrices for Interpreting Satellite Sounding Radiometer Observations. *J. Atmos. Sci.*, **33**, pp 1127-1140, 1976.
- Smith, W. L., and Platt, C.R.M, Comparison of satellite-deduced cloud heights with indications from radiosonde and ground-based laser measurements. *J. Appl. Met.*, **17**, pp 1796-1802, 1978.

## REFERENCES

- Smith, W.L., Woolf, H.M., Hayden, C.M., Wark, D.Q., and McMillin, L.M., The TIROS-N Operational Vertical Sounder, *Bull. Amer. Meteor.Soc.* **60**, pp 1177,1979.
- Staelin, D., F.W. Chen, and F.J. Solman, AMSU/NEXRAD/NAOST-M Precipitation Results Relevant to ATMS, presentation at "Sounder OAT Meeting", 3 February 2000.
- Susskind, J., Rosenfield, J., Reuter, D., Chahine, M.T., Remote sensing of weather and climate parameters from HIRS2/MSU on TIROS-N, *J. Geophys. Res.*, **89**, pp 4677-4697, 1984.
- Susskind, J. and Reuter D., Retrieval of sea-surface temperatures from HIRS2/MSU, *J. Geophys. Res.*, **90C**, pp 11602-11608, 1985a.
- Susskind, J., Reuter, D., Intercomparison of physical and statistical retrievals from simulated HIRS2 and AMTS data. In: Deepak A., Fleming H. E., Chahine, M. T. (eds) *Advances in remote sensing retrieval methods*. A Deepak, Hampton VA, pp 641-661, 1985b.
- Susskind, J., Water vapor and temperature. *Atlas of Satellite Observations Related to Global Change*. Edited by R. J. Gurney, J. L. Foster, and C. L. Parkinson. Cambridge University Press, Cambridge, England, pp 89-128, 1993.
- Susskind, J., Barnett, C., Goldberg, M., Final Report to the Integrated Program Office on the Interferometer Thermal Sounder Study : Part II Comparative Performance of Interferometers/AIRS, 1998.
- Twomey, S., Introduction to the Mathematics of Inversion in Remote Sensing and Indirect Measurements, *Develop. in Geomath.*, **3**, Elsevier Sci., New York, 1977.
- Wilheit, T.T., The effect of winds on the microwave emission from the ocean's surface at 37 GHz, *J. Geophys. Res.*, **84**, pp 4921-4926, 1979.
- Wiscombe, J.W., Exponential Sum Fitting of Radiative Transmission Functions, *Journal of Computational Physics*, **24**, pp 416-444, 1977.

## LIST OF ACRONYMS

ADD	Algorithm Description Document
AER	Atmospheric and Environment Research
AGL	Above Ground Level
ALFA	AER Local Area Forecast Model
AMS	American Meteorological Society
AMSR	Advanced Microwave Scanning Radiometer
AMSU	Advanced Microwave Sounding Unit
APOLLO	AVHRR Processing Scheme Over Cloud Land and Ocean
APS	Algorithm Performance Simulation
ARA	Atmospheric Radiation Analysis
ARD	Algorithm Requirements Document
ARM	Atmospheric Radiation Measurement
ASRR	Algorithm System Requirements Review
ASTER	Advanced Spaceborne Thermal Emission and Reflection Radiometer
ATBD	Algorithm Theoretical Basis Document
ATOVs	Advanced TOVS
AVHRR	Advanced Very High Resolution Radiometer
BT	Brightness Temperature
CC	Cloud Clearing
CEPEX	Central Equatorial Pacific Experiment
CF	Central frequency
CHARTS	Code for High resolution Accelerated Radiative Transfer with Scattering
CKD	Clough, Kneizys and Davies
CLW	Cloud Liquid Water
CMIS	Conical Microwave Imaging Sounder
COD	Cloud Optical Depth
CTH	Cloud Top Height
CTP	Cloud Top Pressure
DEM	Digital Elevation Model
DMSP	Defense Meteorological Satellite Program
DoD	Department of Defense
DOE	Department of Energy
ECMWF	European Centre for Medium-Range Weather Forecasting
EDR	Environmental Data Record
EIA	Earth Incidence Angle
EOF	Empirical Orthogonal Function
EOS	Earth Observing System
ESFT	Exponential Sum Fitting Technique
FFT	Fast Fourier Transform
FIRE	First ISCCP Regional Experiment
FOR	Field Of Regard
FOV	Field Of View
GPS	Global Positioning System
GSFC	Goddard Space Flight Center
HH	Hole Hunting
HIRS	High-resolution Infrared Sounder
HSR	Horizontal Spatial Resolution
IFOR	Instantaneous Field Of Regard

## REFERENCES

IFOV	Instantaneous Field Of View
ILS	Instrument Line Shape
IPO	Integrated Program Office
IPT	Integrated Product Team
ISCCP	International Satellite Cloud Climatology Project
IST	Ice Surface Temperature
IWVC	Integrated Water Vapor Content
JHU	Johns Hopkins University
JPL	Jet Propulsion Laboratory
LA	Lower Atmosphere
LAT	Latitude
LBL	Line By Line
LBLRTM	Line By Line Radiative Transfer Model
LMD	Laboratoire de Météorologie Dynamique
LON	Longitude
LOS	Line Of Sight
LST	Land Surface Temperature
L-V	Levenberg-Marquardt
LVM	Levenberg-Marquardt
MHS	Microwave Humidity Sounder
ML	Maximum Likelihood
MODIS	Moderate-Resolution Imaging Spectrometer
MODTRAN	Moderate Resolution Transmittance Code
MSU	Microwave Sounding Unit
MW	Microwave
NASA	National Aeronautics and Space Administration
NCAR	National Center for Atmospheric Research
NCEP	National Center for Environmental Prediction
NDSI	Normalized Difference Snow Index
NDVI	Normalized Difference Vegetation Index
NEDN	Noise Equivalent Difference
NESDIS	National Environmental Satellite, Data, and Information Service
NN	Neural Network
NOAA	National Oceanic and Atmospheric Administration
NPM	Numerical Prediction Model
NPOESS	National Polar-orbiting Operational Environmental satellite System
NRL	Naval Research Laboratory
NWP	Numerical Weather Prediction
OD	Optical Depth
OI	Optimal Interpolation
OLS	Operational Linescan System
OMIS	Operational Multi-Spectral Imaging Suite
OMPS	Ozone Mapping and Profiler Suite
OSS	Optimal Spectral Sampling
PCA	Principal Component Analysis
PDR	Preliminary Design Review
PSD	Power Spectral Density
POES	Polar Orbiting Environmental Satellite
Psfc	Surface Pressure

## REFERENCES

PSURF	Surface Pressure
QC	Quality Control
RDR	Raw Data Records
RH	Relative Humidity
RMS/ <i>rms</i>	Root Mean Square
RMSE	Root Mean Square Error
RRTM	Rapid Radiative Transfer Model
RT	Radiative Transfer
RTA	Radiative Transfer Algorithm
RTE	Radiative Transfer Equation
RTM	Radiative Transfer Model
S/N	Signal/Noise
SAR	Synthetic Aperture Radar
SCPR	Simultaneous Cloud Parameter Retrieval
SDR	Sensor Data Record
SEIT	System Engineering Integrated Product Team
SFR	System Functional Review
SGI	Silicon Graphics, Inc.
SPS	System Performance Simulation
SRD	Sensor Requirement Document
SRR	System Requirements Review
SSM/I	Special Sensor Microwave/Imager
SSM/T	Special Sensor Microwave/Temperature
SSMIS	Special Sensor Microwave Imager Sounder
SST	Sea Surface Temperature
SVD	Single Value Decomposition
SW	Shortwave
T	Temperature
TBD	To Be Determined (by contractor)
TBR	To Be Resolved (by contractor/government)
TBS	To Be Supplied (by government)
TIGR	TOVS Initial Guess Retrieval
TIM	Technical Interchange Meeting
TOA	Top Of Atmosphere
TOD	Time of Day
TOVS	TIROS-N Operational Vertical Sounder
TRD	Technical Requirements Document
TSKIN	Skin Temperature
UA	Upper Atmosphere
UR	Unified Retrieval
USGS	United States Geological Survey
VIIRS	Visible/Infrared Imager/Radiometer Suite
Vis	Visible
WPTB	Weather Product Test Bed
WV	Water Vapor
WVF	Water Vapor Fraction

## REFERENCES

This page intentionally left blank.